creative commons
COMMONS DEED

저작자표시-비영리-변경금지 2.0 대한민국

이용자는 아래의 조건을 따르는 경우에 한하여 자유롭게

- 이 저작물을 복제, 배포, 전송, 전시, 공연 및 방송할 수 있습니다.

다음과 같은 조건을 따라야 합니다:

**저작자표시**. 귀하는 원저작자를 표시하여야 합니다.

**비영리**. 귀하는 이 저작물을 영리 목적으로 이용할 수 없습니다.

**변경금지**. 귀하는 이 저작물을 개작, 변형 또는 가공할 수 없습니다.

- 귀하는, 이 저작물의 재이용이나 배포의 경우, 이 저작물에 적용된 이용허락조건을 명확하게 나타내어야 합니다.
- 저작권자로부터 별도의 허가를 받으면 이러한 조건들은 적용되지 않습니다.

**저작권법에 따른 이용자의 권리는 위의 내용에 의하여 영향을 받지 않습니다.**

이것은 이용허락규약(Legal Code)을 이해하기 쉽게 요약한 것입니다.

Disclaimer

dCollection

**Ph.D. Dissertation of Engineering**

# Biological and Mechanical Properties of MAX Phases and MXene/PLA Nanocomposites

**February 2018**

**Graduate School of Engineering**

**Seoul National University**

**Materials Science and Engineering Major**

**Chen Ke**

# Biological and Mechanical Properties of MAX Phases and MXene/PLA Nanocomposites

**Supervisor: Prof. Hyoun-Ee Kim**

**Submitting a Ph.D. Dissertation of Engineering**

**January 2018**


**Graduate School of Engineering**

**Seoul National University**

**Materials Science and Engineering Major**

**Chen Ke**


**Confirming the Ph.D. Dissertation written by Chen Ke**

**February 2018**

**Chair : Cheol-Hee Ahn (Seal)**

**Vice Chair: Hyoun-Ee Kim (Seal)**

**Examiner : Young-Hag Koh (Seal)**

**Examiner : Jeong-Yun Sun (Seal)**

**Examiner : Byung-Ho Yoon (Seal)**

# Abstract

# Biological and Mechanical Properties of MAX Phases and MXene/PLA Nanocomposites

Chen Ke

Department of Materials Science and Engineering

Seoul National University

Dental implant surgery has been popularly trusted by the worldwide patients for oral rehabilitation. However, the poor resistance to physical abrasion and fatigue fracture, and the detrimentally released ions of the traditional Ti-based materials (such as pure Ti and Ti-6Al-4V alloy) are crucial factors from the aspect of materials influencing on the survival rates. MAX phase is a terminology for a family of layered ternary compounds, which possess high flexural strength, fracture toughness, and damage tolerance, good tribological properties, excellent machinability, and

good oxidation and corrosion resistance because of their unique structure, in which alternate near-close-packed layers of covalent $M_6X$ octahedrons are interleafed with metal-like A atom layers. Therefore, MAX phases have the potential to be used in the biomedical application, in particularly dental and orthopedic fields. Nevertheless, the results of previous works which merely focus on the $Ti_3SiC_2$ are inconsistent. The reason for this phenomenon is still blurry. Since the biological responses to host tissue cells must be considered in the development of synthetic biomaterials, it is essential to systematically evaluate the biocompatibility of MAX phase and establish the general mechanism for such a numerous family (more than 70 members).

This thesis first explored the biocompatibility of the selected MAX phases ($Ti_3AlC_2$, $Ti_3SiC_2$, and $Ti_2AlN$) on basis of different A-site and X-site atoms. The results of cell tests showed that these phases were innocuous to preosteoblasts and fibroblasts. Compared with the strong viable fibroblasts, the different cellular responses of these materials were clearly distinguishable for the preosteoblasts. Under an osteoblastic environment, $Ti_2AlN$ exhibited better cell proliferation and osteogenic differentiation performance than $Ti_3AlC_2$ and $Ti_3SiC_2$. Moreover, the performance was superior to that of a commercial Ti-6Al-4V alloy and comparable

to that of pure Ti. A general mechanism was suggested based on the different surficial oxidation products, which were determined from the binding energy of the adsorbed $Ca^{2+}$ ions using first-principles calculations. Compared with the partially oxidized $TiC_xO_y$ layer on $Ti_3AlC_2$ and $Ti_3SiC_2$, the partially oxidized $TiN_xO_y$ layer on the $Ti_2AlN$ had a stronger affinity to the $Ca^{2+}$ ions, which indicated the good biocompatibility of $Ti_2AlN$. In addition, the (001) surfaces were proved to possess the strongest binding energy with the $Ca^{2+}$ ions in a certain MAX phase. This phenomenon disclosed the good biocompatibility of the 2-dimensional transition metal carbides or nitrides (MXenes), which mainly were composed of these (001) surfaces.

Guided bone regeneration (GBR) technique is a reliable and validated therapy to augment the bone for the surgery of dental implantation. Although the resorbable GBR membrane is fascinating, which protects the bone healing from the interference of non-osteogenic tissue, and exempts the secondary surgery for the removal of remaining membrane, the poor mechanical properties and cellular responses are critical issues, which usually result in insufficient amount of regenerated bone. In the second work of this thesis, $Ti_3C_2T_z$ nanosheets (delaminated $Ti_3C_2T_z$, d-$Ti_3C_2T_z$), the representative of MXenes, were used to

enhance the mechanical properties and biocompatibility of Poly (lactic acid) (PLA) membrane. As a prerequisite, the intrinsic biocompatibility of d-$Ti_3C_2T_z$ was first authenticated using that of widely-discussed graphene oxide (GO) for reference. The strong and biocompatible d-$Ti_3C_2T_z$ enhanced PLA nanocomposite membranes were fabricated using the interfacial mediation with n-octyltriethoxysilane (OTES). To the best of our knowledge, this was the first effort to introduce MXene into polymer matrix for biomedical applications. The optimized ultimate tensile strength (UTS) of OTES-d-$Ti_3C_2T_z$/PLA nanocomposite membrane was 72 MPa (obtained at 0.5 wt.%), which increased by 33%. This enhancement was almost the highest compared with the graphene-enhanced works, where the solvent casting was adopted. The reason could be ascribed to the strong interaction between OTES-$Ti_3C_2T_z$ and PLA, which ensured the efficient load transferring between these two components. The d-$Ti_3C_2T_z$ was also certified to significantly promote the adhesion, proliferation, and osteogenic differentiation of preosteoblasts on the nanocomposite membranes, which exhibited ascending trend along with the increasing filler content (0 to 1 wt.%).

**Keywords:** $Ti_3AlC_2$, $Ti_2AlN$, $Ti_3C_2T_z$, Poly (lactic acid), *In vitro* test,

First-principles calculation, Biocompatibility, Mechanical properties.

**Student number**: 2015-30843

# Contents

# List of Tables

# List of Figures

interfacial layer formation at UV-photofunctionalized titanium surfaces. The image is reprinted from *Biomaterials*.

**Fig. 1.8.** Schematic diagram of mechanism for different effects of bare and TiN-coated NiTi alloys on endothelial cell function. The image is reprinted from *Biomaterials*.

**Fig. 1.9.** Snapshots from a FPMD simulation at 300 K showing the adsorption of a $Ca^{2+}$ ion on the hydrated partially oxidized TiN surface. (A) Initial configuration, after relaxation of the system for ~300 fs keeping fixed the $Ca^{2+}$ ion; **(B)** After ~180 fs of simulated time; **(C)** After ~650 fs of simulated time. The image is reprinted from *Acta Materialia*.

**Fig. 2.1.** XRD spectra of the self-prepared $Ti_3AlC_2$ (black line), $Ti_3SiC_2$ (red line), and $Ti_2AlN$ (blue line) bulks.

**Fig. 2.2.** SEM surface morphology of the self-prepared **(A)** $Ti_3AlC_2$, **(B)** $Ti_3SiC_2$, and **(C)** $Ti_2AlN$ bulks.

**Fig. 2.3.** XPS spectra of $Ti_3AlC_2$ bulks: **(A)** Ti 2p region, **(B)** Al 2p region, **(C)** C 1s region and **(D)** O 1s region.

**Fig. 2.4.** XPS spectra of $Ti_3SiC_2$ bulks: **(A)** Ti 2p region, **(B)** Si 2p region, **(C)** C 1s region and **(D)** O 1s region.

**Fig. 2.5.** XPS spectra of $Ti_2AlN$ bulks: **(A)** Ti 2p region, **(B)** Al 2p region, **(C)** N 1s region and **(D)** O 1s region.

**Fig. 2.6.** Hydrophilicity of the self-prepared $Ti_3AlC_2$, $Ti_3SiC_2$, and $Ti_2AlN$ bulks determined by the contact angle with deionized water compared with pure Ti and

Ti-6Al-4V alloy.

**Fig. 2.7.** Typical CLSM images used to determine the morphology of MC3T3-E1 cells attached on the surfaces of **(A)** $Ti_3AlC_2$, **(B)** $Ti_3SiC_2$, **(C)** $Ti_2AlN$, **(D)** Ti–6Al–4V alloy, and **(E)** pure Ti specimens after incubation for 3 h. Phalloidin and DAPI were used to stain the filamentous actin (red) and nucleus (blue), respectively. The seeding cell density was $1\times10^4$ cells/mL.

**Fig. 2.8.** Spreading areas of the preosteoblasts attached on the $Ti_3AlC_2$, $Ti_3SiC_2$, $Ti_2AlN$, Ti–6Al–4V alloy, and pure Ti specimens, which was obtained from the calculation of *ImageTool 3.0* using fifty CLSM images (**Fig. 2.9**) for each material at ×20 magnification. (**$p < 0.01$)

**Fig. 2.9.** Typical CLSM images used for calculating the spreading area of the preosteoblasts on the surfaces of **(A)** $Ti_3AlC_2$, **(B)** $Ti_3SiC_2$, **(C)** $Ti_2AlN$, **(D)** Ti–6Al–4V alloy, and **(E)** pure Ti specimens after incubation for 3 h. Phalloidin and DAPI were used to stain the filamentous actin (red) and nucleus (blue), respectively. The seeding cell density was $1\times10^4$ cells/mL.

**Fig. 2.10.** MTS assay for determining the cell viability of MC3T3-E1 cells on the $Ti_3AlC_2$, $Ti_3SiC_2$, $Ti_2AlN$, Ti–6Al–4V alloy, and pure Ti specimens after 5-day and 7-day incubation. The seeding cell density was $1\times10^4$ cells/mL. (*$p < 0.05$, ***$p < 0.001$)

**Fig. 2.11.** Typical CLSM image used to determine the corresponding distribution of MC3T3-E1 cells grown after 7 days. Phalloidin and DAPI were used to stain the filamentous actin (red) and nucleus (blue), respectively. The seeding cell density was $1\times10^4$ cells/mL.

**Fig. 2.12.** ALP activity used to determine the differentiation of MC3T3-E1 cells after 12-day incubation on the $Ti_3AlC_2$, $Ti_3SiC_2$, $Ti_2AlN$, Ti–6Al–4V alloy, and pure Ti specimens. The seeding cell density was $1\times10^4$ cells/mL. (*$p < 0.05$)

**Fig. 2.13.** Biological behaviors of L929 cells on the $Ti_3AlC_2$, $Ti_3SiC_2$, $Ti_2AlN$, Ti–6Al–4V alloy, and pure Ti specimens: **(A)** Morphology and distribution of L929 cells after incubation for 3 h; **(B-C)** Cell proliferation determined from CLSM image (7 days) and MTS assay after 3-day and 5-day incubation. Phalloidin and DAPI were used to stain the filamentous actin (red) and nucleus (blue), respectively. The seeding cell density was $1\times10^4$ cells/mL. (*$p < 0.05$, **$p < 0.01$)

**Fig. 2.14.** Different configurations of the (100) and (001) surfaces for the $Ti_3AlC_2$, $Ti_3SiC_2$, and $Ti_2AlN$.

**Fig. 2.15.** Optimized configurations for partially oxidized surfaces of the $Ti_3AlC_2$, $Ti_3SiC_2$, and $Ti_2AlN$.

**Fig. 2.16.** Schematic diagram of the possible positions that the $Ca^{2+}$ ions (green spheres) bound on the $Ti_3AlC_2$ and $Ti_3SiC_2$. (TAC and TSC represent $Ti_3AlC_2$ and $Ti_3SiC_2$, respectively)

**Fig. 2.17.** Schematic diagram of the possible positions that the $Ca^{2+}$ ions (green spheres) bound on the $Ti_2AlN$. (TAN represents $Ti_2AlN$)

**Fig. 2.18.** Optimized configurations for the $Ca^{2+}$ ion bound on the (001), (100)-1, (100)-2, and (100)-3 surfaces of the $Ti_3AlC_2$, $Ti_3SiC_2$, and $Ti_2AlN$ and the (110) surface of $rTiO_2$.

density was $5\times10^4$ cells/mL; **(B)** The hydrophilicity determined by the contact angle with the deionized water; **(C)** The cell proliferation after 5-day and 7-day incubation determined by DNA assay. Seeding cell density was $1\times10^4$ cells/mL. (**P<0.01); **(D)** The cell differentiation after 12-day incubation determined by ALP activity. Seeding cell density was $1\times10^4$ cells/mL. (***P<0.001)

**Fig. 3.11.** Schematic diagram of surface modification of OTES on the d-$Ti_3C_2T_z$.

**Fig. 3.12.** **(A)** FT-IR spectra of d-$Ti_3C_2T_z$ (black) and OTES grafted d-$Ti_3C_2T_z$ (red). **(B)** The dispersity and stability of d-$Ti_3C_2T_z$ (black) and OTES grafted d-$Ti_3C_2T_z$ (red) in the DCM determined by the relative absorbance of UV-visible spetrophotometer at 800 nm. Inset: digital images.

**Fig. 3.13.** Optical images of PLA and OTES-d-$Ti_3C_2T_z$/PLA composite membranes prepared using simple solvent casting.

**Fig. 3.14.** Typical SEM cross section morphology of pure PLA and OTES-d-$Ti_3C_2T_z$/PLA nanocomposite membranes with different loading content: **(A)** Pure PLA, **(B)** 0.2 wt. %, **(C)** 0.5 wt. %, **(D)** 1 wt. %, **(E)** 2 wt. %.

**Fig. 3.15.** the typical stress-strain curves **(A)** and ultimate tensile strength and Young's modulus **(B)** of pure PLA and OTES-d-$Ti_3C_2T_z$/PLA nanocomposite membranes.

**Fig. 3.16.** Comparison of UTS and its enhancement of OTES-d-$Ti_3C_2T_z$/PLA nanocomposite membrane in this work with those of the membranes which were enhanced by graphene (or reduced GO), GO, and functional group modified GO from the references.

**Fig. 3.17.** Typical CLSM images of adherent MC3T3-E1 cells on pure PLA and OTES-d-$Ti_3C_2T_z$/PLA nanocomposite membranes: **(A)** Pure PLA, **(B)** 0.2 wt. %, **(C)** 0.5 wt. %, **(D)** 1 wt. %.

**Fig. 3.18**. Typical SEM images of adherent MC3T3-E1 cells on pure PLA and OTES-d-$Ti_3C_2T_z$/PLA nanocomposite membranes: **(A)** Pure PLA, **(B)** 0.2 wt. %, **(C)** 0.5 wt. %, **(D)** 1 wt. %.

**Fig. 3.19.** DNA assay for determining the cell viability of preosteoblasts on the pure PLA and OTES-d-$Ti_3C_2T_z$ enhanced PLA composite membranes after 5-day and 7-day incubation. Seeding cell density was $1\times10^4$ cells/mL.

**Fig. 3.20.** The amount of protein obtained from the preosteoblasts after incubating on the pure PLA and OTES-d-$Ti_3C_2T_z$ enhanced PLA composite membranes for 12 days. Seeding cell density was $0.5\times10^4$ cells/mL.

**Fig. 3.21.** ALP assay for determining the cell differentiation of preosteoblasts on the pure PLA and OTES-d-$Ti_3C_2T_z$ enhanced PLA composite membranes after 12-day incubation. Seeding cell density was $0.5\times10^4$ cells/mL.

# Chapter 1.

# Introduction

## 1.1 Generalities of Ti-based Materials for Dental Application

According to the statistics of *American Association of Oral and Maxillofacial Surgeons* (AAOMS), 69% of adults whose age are from 35 to 44, have lost at least one permanent tooth because of an accident, gum disease, a failed root canal or natural tooth decay. [1] Dental implantation is a popular therapy for effective restoration, which has progressed rather rapidly over the past two decades. The number of patients receiving the dental implant surgery has increased steadily all over the world, reaching about one million dental implantations per year. [2] The demand is still booming particularly in China. The annual rate is expected to 30% due to the low implant penetration in contrast with that in Italy and South Korea (*China Industry Research*) (**Fig. 1.1**). Although the dental implantation is a kind of mature technique, the failures happen from time to time (survival rates range is from 90% to 96.5%) [3, 4] because of the inflammation, implant fractures, physical abrasion, fatigue crack, implant loosening and exposure of implant. [5, 6] Besides the infection during or after surgery, and undesirable personal conditions of the patients (such as insufficient alveolar bone, and periodontitis), the incomplete mechanical properties and biocompatibility of the materials are also the critical problems.

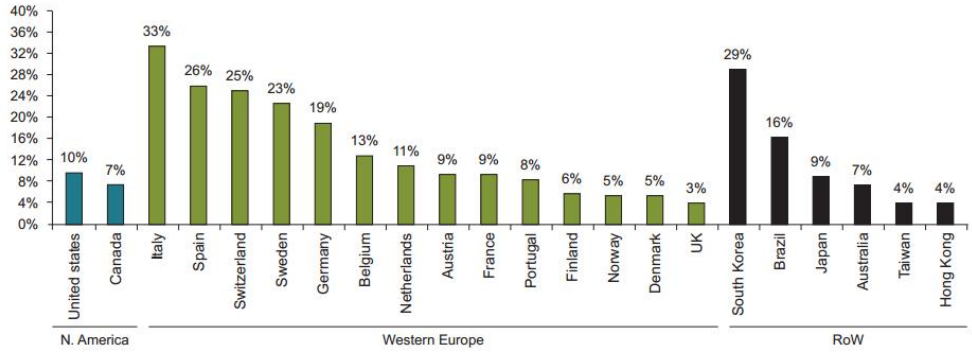


**Fig. 1.1.** The ratio of implant penetration to tooth restoration. The image is reprinted from *DENTSPLY IMPLANTS magazine*. [1]

Ti-based materials have good biocompatibility because the partially released Ti ion is very active and rapidly reacts with hydroxyl radicals or anions in body fluid to form the oxides or salts, so that the Ti ion will not combine with the biomolecules, which might interfere the normal physiology. Likewise, the passive layer consisting of compact $TiO_2$ can prevent the further corrosion. [7, 8] Traditional Ti-based materials such as pure Ti (ASTM grade 4) and Ti-6Al-4V (ASTM grade 5) have been proverbially used as the bone substitutes, dental implant, screw fixation and many other orthopedic applications because of their good biocompatibility and high mechanical properties. [9-13] However, the physical abrasion resistance and fatigue fracture of pure Ti and Ti-6Al-4V alloy need to be enhanced regarding as the dental

materials. [13-15] The native formed $TiO_2$ film is easily fractured because of the poor mechanical properties under the conditions of fretting and sliding wear. [16] Hence, more V ions will be released from the Ti-6Al-4V alloy before the regeneration of $TiO_2$ film. These detrimental ions probably result in gastrointestinal discomfort, and even have a toxic effect on the liver and kidney, [17, 18] which is supposed to be avoided in the biomedical applications. [19, 20]

Nowadays, titanium carbide (TiC), titanium nitride (TiN), titanium oxy nitride (TiON) and titanium aluminum nitride (TiAlN) have been widely used as the coating film to strengthen the surficial hardness and wear resistance of the pure Ti and Ti-6Al-4V alloy, which is also helpful to reduce the releasing of V ions. [14, 21, 22] However, the interface between the coating and substrate is always a weak defect. The preparation process of corresponding bulks mainly consisting of these brittle refractory titanium carbide or nitride needs quite high sintering temperature (more than 2000 K). [23] Therefore, the development of new Ti-based materials with better mechanical properties and biological responses is always the intriguing trend for dental materials. [5]

## 1.2 Generalities of Guided Bone Regeneration (GBR) Membrane

Guided bone regeneration (GBR) is a reliable and validated therapy which has been widely used in oral rehabilitation with the placement of dental implants and periodontal regeneration. [24-26] The basic concept of GBR strategy is based on the hypothesis that protecting the bone healing of the defect from the interference of non-osteogenic tissue (such as epithelial tissue) using a GBR membrane [25-27] (**Fig. 1.2**). This membrane should maintain the space of the osseous defect, exclude the soft tissue cells, as well as possess good biological affinity, tissue integration, and ease of use. [27, 28]

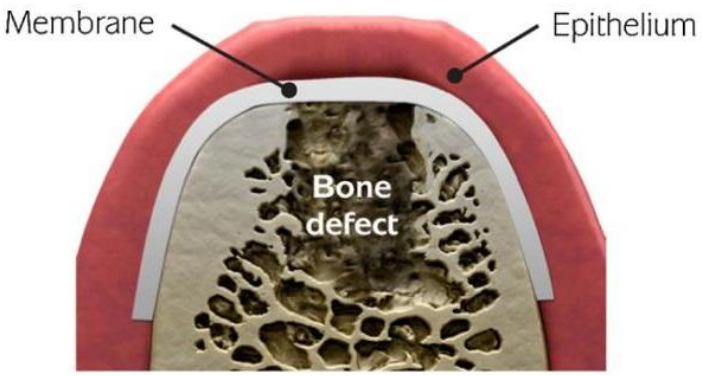


**Fig. 1.2.** Schematic illustration of GBR membrane used in augmenting the bone for dental implant. (The figure is reprinted from *Dental Materials*) [26]

The GBR membrane can be roughly classified to two generations. Compared with non-resorbable Ti and expanded polytetrafluoroethylene (ePTFE) membranes, the resorbable membranes, such as poly (lactic acid) (PLA), poly (glycolic acid) (PGA), poly (ε-caprolactone) (PCL) and their copolymers or tissue-derived collagens, chitosan, gelatin, and silk fibroin, are more fascinating because of the exemption from the secondary surgery to extract the remaining membrane. [26, 29] Nowadays, the commercial GBR membranes are mainly fabricated using the above materials. For instance, the representatives of non-resorbable membranes: Gore-Tex® (e-PTFE), High-density Gore-Tex® (high-density PTFE), and Gore-Tex-Ti® (Ti reinforced PTFE); the representatives of resorbable membranes: Guidor®, Epi-Guide®, and Vivosorb® are mainly made of PLA; Resolut Adapt® and Biomesh-S ® are mainly made of PLGA; And Bio-Gide®, Ossix®, Biomend®, Dentium®, Lyoplant®, Cytoplast®, and Heal-All® are mainly made of collagen. [28] Notwithstanding the good biocompatibility of naturally derived polymers, the synthetic polymers are more handily to control the biodegradability, rigidity, manageability, processability, and drug-encapsulating ability. Likewise, they have more convenient and stable source of the raw materials, which can avoid the possible disease transmission from the animals. [30-33] However, the poor mechanical

properties [29] and cell affinity [26, 29] are crucial issues for these resorbable membranes, which result in insufficient amount of regenerated bone. For instance, David Schneider and his cooperators compared the clinical performances between titanium-reinforced expanded polytetrafluorethylene membrane and modified polylactide-co-polyglycolide acid membrane. The results showed that in the cases of resorbable membrane, the horizontal thickness of regenerated bone was much thinner than in the cases of the PTFE membrane. Meanwhile, the membrane exposure happened more frequently in the cases of the resorbable membranes. [29]

The incorporation of secondary phase is one of the effective methods to enhance the polymer matrix. Currently, graphene and its derivates have been corroborated to strengthen the mechanical properties of polymeric matrices (classified in **Fig. 1.3**) Herein, the PLA is selected as the matrix for summary owing to its wide application in commercial GBR membrane. [34, 35, 43] The graphene (G) or reduced graphene oxide (rGO) which has relatively hydrophobic surface is more efficacious than the hydrophilic bare GO. Whereas, the GO can be also used to reinforce the mechanical properties of hydrophobic PLA effectively after the modification of interface. In addition, these nanosheets are also discovered to promote interfacial bio-interactions including: **(1)** Adsorbing and concentrating

nutrition factors; **(2)** Mediating their cellular signaling and biological performance with co-cultured cells; **(3)** Accelerating cell adhesion and growth, and affecting cell proliferation and differentiation. [53-55]

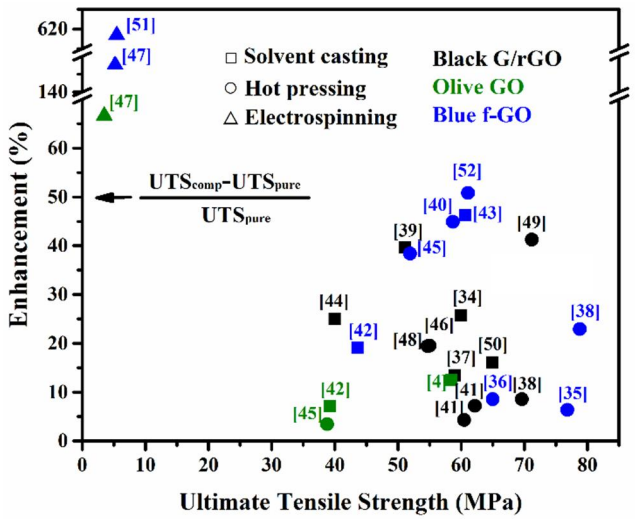


**Fig. 1.3.** Classification of the ultimate tensile strength (UTS) and its enhancement of PLA nanocomposite which was enhanced by graphene (G) or reduced graphene graphene (rGO), GO, and functional group modified GO (f-GO) from the previous references. [34-52]

## 1.3 Generalities of MAX Phases

The layered ternary machinable ceramics, $M_{n+1}AX_n$ phases, are composed of an early transition metal (**M**), an A-group element (**A**), and a C and/or N (**X**); and n equals to 1-6 (**Fig. 1.4**). [56, 57] MAX phases exhibit good tribological properties, damage tolerance, and oxidation and corrosion resistance because of their unique structure, in which alternate near-close-packed layers of covalent $M_6X$ octahedrons are interleafed with metal-like A atom layers. [56, 58-63] For instance, the commonly discussed Ti-based MAX phases, $Ti_3AlC_2$, $Ti_3SiC_2$, and $Ti_2AlN$, have much greater flexural strength and fracture toughness (such as $Ti_3AlC_2$, 340–450 MPa [64] and 4.6–9.1 $MPa \cdot m^{1/2}$ [63]; $Ti_3SiC_2$, 720 MPa [65] and 4.5–16 $MPa \cdot m^{1/2}$ [63]; $Ti_2AlN$, 350–371 MPa [66] and 8.2 $MPa \cdot m^{1/2}$ [67]) than those of common bioceramics (such as hydroxyapatite, 65–85 MPa [68] and 0.65–0.70 $MPa \cdot m^{1/2}$ [69]). Therefore, these machinable ceramics have been used as the concrete dry drills, gas burner nozzles, heat exchangers and screw. [56, 63]

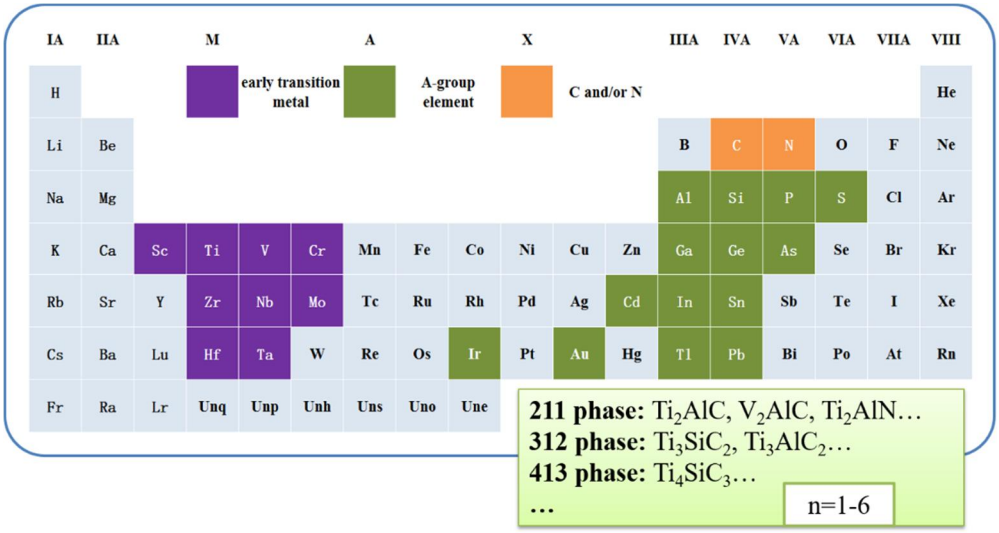


**Fig. 1.4.** The elements composition of $M_{n+1}AX_n$ phases.

In the previous researches, the MAX phase ($Ti_3SiC_2$) has been discussed as the structural materials in biomedical application because of their attractive mechanical properties. [70-72] Gao and Miyamoto et al [71] deemed that the $Ti_3SiC_2$ (3 vol. % TiC) was bio-inert. After 24-week implantation in tibia periosteum of rabbit, there was no adverse foreign body reaction being observed. In addition, the $Ti_3SiC_2$ exhibited a good performance to resist the corrosion of 0.9 wt. % NaCl solution. However, Ngai et al [72] found that when the SiC-reinforced $Ti_3SiC_2$ composite was implanted into the femur of New Zealand rabbit, a few of foreign-body granulomas and eosinophilic leukocytes could be observed after 10-week implantation; However, the surface of composite maintained intact as before. Owing to the lack of control

group such as pure $Ti_3SiC_2$ or SiC in their experiment, it was difficult to exactly evaluate the biocompatibility of these $Ti_3SiC_2$-based composites. For the specific applications, Shi et and cooperators [73, 74] utilized the $Ti_3SiC_2$ powders as the secondary phase to strengthen and toughen the hydroxyapatite. The bending strength and fracture toughness of the composite were confirmed to increase from 75 to 250 MPa, and from 0.8 to 3.9 $MPa \cdot m^{1/2}$, along with the decreasing of Vickers hardness. This composite even performed excellent machinability when the loaded content of $Ti_3SiC_2$ was more than 20 vol. %.

Nevertheless, all the above current researches concentrate on the $Ti_3SiC_2$. The reasons for inconsistent biological behaviors remains unclear, and verification of the biocompatibility of MAX phases, especially for the other phases in this large family (more than 70 members), remains insufficient. It is important and necessary to establish the general mechanism on the biocompatibility of MAX phases for doping out the potential application of the overall phases in biomedical fields.

## 1.4 Generalities of 2D Metal Carbides or Nitrides (MXenes)

Recently, the burgeoning two-dimensional (2D) materials such as graphene, transition metal dichalcogenides (TMDs), boron nitrides, and MXenes possessing distinctive properties from their three-dimensional (3D) counterparts have attracted tremendous attention. [75-79] MXenes is an emerging family of 2D early transition metal carbides or nitrides, derived by the selective exfoliation of "A" layers with chemical etching from MAX phases (such as hydrofluoric acid, ammonium hydrogen difluoride or lithium fluoride-hydrochloric acid mixture solution), and following physical delamination with sonication (**Fig. 1.5**). [56, 62, 79-81] Therefore, there are two kinds of typical morphologies of MXene. The accordion-like stacked MXene (exfoliated MXene, e-MXene) is obtained after the chemical exfoliation. The MXene nanosheet (delaminated MXene, d-MXene) is obtained after the delamination of e-MXene using the sonication with the intercalated molecules such as dimethyl sulfoxide (DMSO), $H_2O$ and $Li^+$ ion. To date, quite a vast number of MXenes have been synthesized with the general formula of $M_{n+1}X_nT_z$ (where M is an early transition metal, X is a C and/or N, n is 1, 2, 3, and $T_z$ stands for the terminated groups, such as -OH, -O and -F). [79, 80, 82, 83] (**Table 1.1**) Owing to the abundance of MAX phases, the composition and structure of MXene are far more

easily to be tunable than that of graphene. For instance, the porous MXene (porous $Ti_3C_2T_z$, $V_2CT_z$, and $Nb_2CT_z$) can be fabricated using the oxidation and following acid etching of the specific metal ions. [84] In addition, the sandwich-like ordered double transition metal MXene, $Mo_2TiC_2T_z$, $Mo_2Ti_2C_3T_z$, and $Cr_2TiC_2T_z$, can be obtained using the adjustment of M-site atom. [85] Moreover, MXene can be composed of nitrides, such as the $Ti_4C_3T_z$, which is obtained from the etching of molten fluoride salt (LiF, NaF, and KF at 550 °C) from the $Ti_4AlN_3$. [86] As special cases, the $Zr_3C_5T_z$, $Hf_3C_2T_z$, $SCT_z$, and $Mo_2CT_z$ nanosheets can be synthesized using the etching of $Al_3C_3$ from $Zr_3Al_3C_5$, the etching of Ti from $Ti_2SC$, and the etching of Ga from $Mo_2Ga_2C$, separately. [87-90]

These nanosheets possess large specific surface area, excellent electrical conductivity, and good hydrophilicity, which grant them desirable candidates for versatile applications such as in energy storage (such as the electrode for supercapacitor, lithium-ion battery, and lithium–sulfur battery), [91-93] surface absorbent (such as Pb(II), Cr(VI), and U(VI)), [94-96] and sensor device (such as temperature, $CO_2$, nitrite, and $H_2O_2$). [97-100]

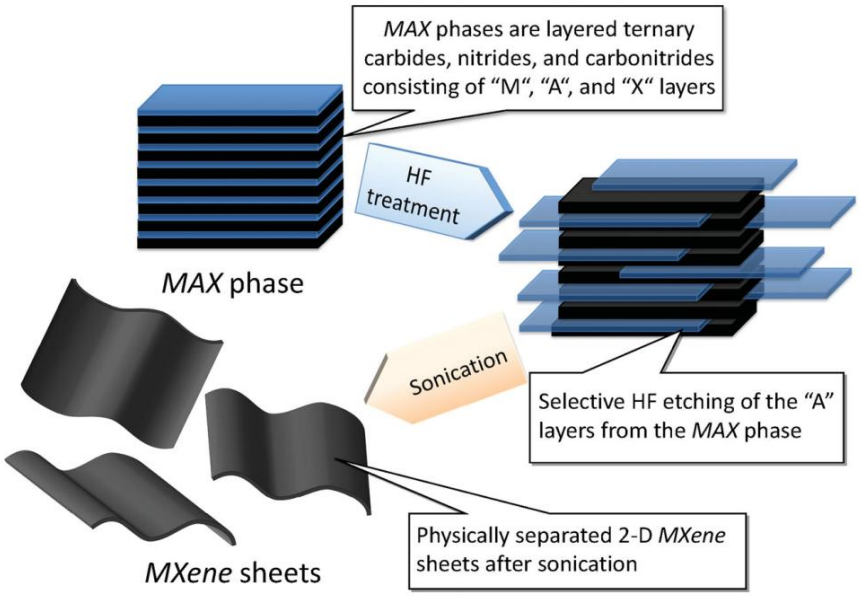


**Fig. 1.5.** Schematic diagram describing the synthesis process of MXenes from MAX phases. The image is reprinted from *ACS Nano*. [80]

**Table 1.1.** The current synthesized MXene from MAX phase.

| MAX phase structure | MAX phase | MXene |
|---|---|---|
| 211 | $Ti_2AlC$ | $Ti_2CT_z$ [80] |
| | $V_2AlC$ | $V_2T_z$ [83] |
| | $Nb_2AlC$ | $Nb_2T_z$ [83] |
| | $(Ti_{0.5}Nb_{0.5})_2AlC$ | $(Ti_{0.5}Nb_{0.5})_2CT_z$ [80] |
| 312 | $Ti_3AlC_2$ | $Ti_3C_2T_z$ [79] |
| | $Ti_3AlCN$ | $Ti_3CNT_z$ [80] |
| | $(V_{0.5}Cr_{0.5})_3AlC_2$ | $(V_{0.5}Cr_{0.5})_3C_2T_z$ [80] |
| 413 | $Ta_4AlC_3$ | $Ta_4C_3T_z$ [80] |
| | $Nb_4AlC_3$ | $Nb_4C_3T_z$ [82] |
| | $Ti_4AlN_3$ | $Ti_4N_3T_z$ [86] |
| Special | $Zr_3Al_3C_5$ | $Zr_3C_2T_z$ [87] |
| | $Hf_3[Al(Si)]_4C_6$ | $Hf_3C_2T_z$ [88] |
| | $Ti_2SC$ | $SCT_z$ [89] |
| | $Mo_2Ga_2C$ | $Mo_2CT_z$ [90] |

Very recently, MXenes have aroused great interests in the biomedical applications fields. The $TiO_2$ nanoparticle modified accordion-like $Ti_3C_2T_z$ (e-$Ti_3C_2T_z$) is confirmed to be used as supporting materials for hemoglobin to detect the concentration of $H_2O_2$ (**Fig. 1.6(A)**). This biosensor has high sensitivity (447.3 $\mu A\ mM^{-1}\ cm^{-2}$), wide detection range (0.1–380 μM), and low detection limit (14

nM). [98] $Ti_3C_2T_z$ nanosheets (d-$Ti_3C_2T_z$) also exhibits a high antibacterial efficiency with growth inhibition of 99% for Escherichia coli (E. coli) and Bacillus subtilis (B. subtilis), which reveals that MXenes can serve as novel antimicrobial nanomaterials in environmental and biomedical applications (**Fig. 1.6(B)**). [101, 102] In addition, $Ti_3C_2T_z$ nanosheets (d-$Ti_3C_2T_z$) is discovered to have high efficiency for photothermal conversion and *in vitro*/*in vivo* photothermal ablation of tumor, which indicates the great potential for cancer therapy (**Fig. 1.6(C)**). [103] In particularly, the *in situ*-grown MnOx/d-$Ti_3C_2$ composite can be developed as multifunctional theragnostic agents for efficient magnetic resonance (MR) and photoacoustic (PA) dual-modality imaging-guided photothermal therapy (PTT) to oppose the cancer. This charming therapy has efficient tumor detection, high photothermal-conversion performance, and good biocompatibility. [104] Similarly, $Ti_3C_2T_z$ nanosheets (d-$Ti_3C_2T_z$) can be also trimmed to quantum dots like the graphene quantum dots using hydrothermal method. These MXene quantum dots are photoluminescent (quantum yields up to ≈10%), which can be used as cellular imaging for macrophage (RAW264.7) (**Fig. 1.6(D)**). [105] Finally, the $Ti_3C_2T_z$ nanosheets (d-$Ti_3C_2T_z$) can be used to assemble the ultrathin MXene-based field-effect

transistors, which enabled the real-time, label-free monitoring of neuronal spiking activities [106].

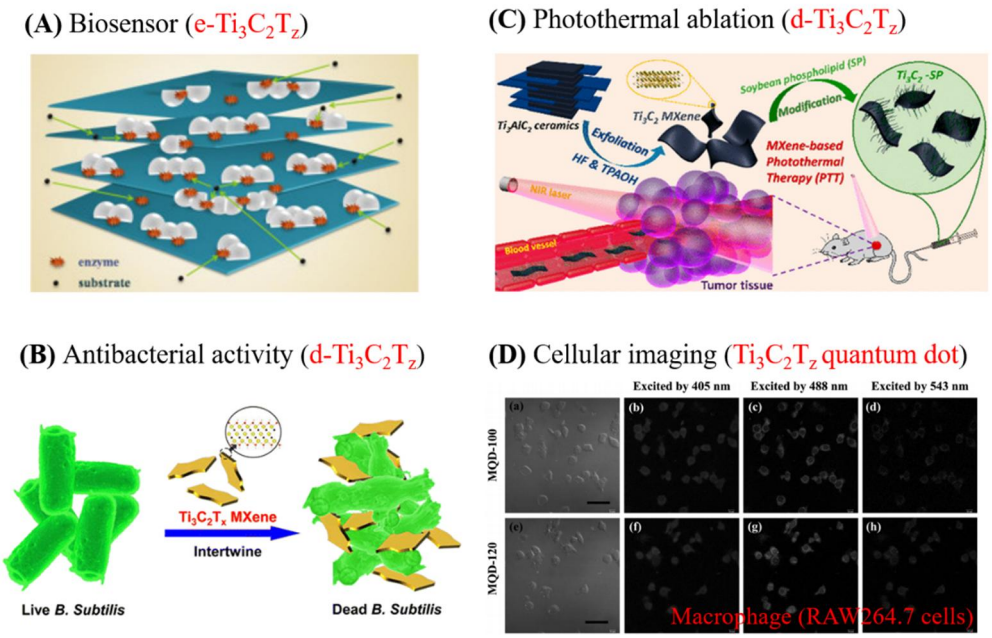


**Fig. 1.6.** Representative applications of MXene ($Ti_3C_2T_z$) in biomedical fields: **(A)** Biosensor, reprinted from *Biosensors and Bioelectronics*; [98] **(B)** Antibacterial activity, reprinted from *ACS Nano*; [101] **(C)** Photothermal ablation, reprinted from *Nano Letter*; [103] **(D)** Cellular imaging, reprinted from *Advanced Materials*. [105]

## 1.5 Generalities of Biocompatibility

Biocompatibility has been defined as ‘‘the ability of a material to perform with an appropriate host response in a specific application’’. [8] This means that the biomaterials or any leachable products from them do not cause serious cell death, chronic inflammation or other impairment of cellular or tissue functions. [8] In addition, the desirables for the biocompatibility should contain non-inflammatory, non-toxic, noncarcinogenic, nonpyrogenic, blood compatible, and non-allergic performances as well. [107] To investigate the biocompatibility of biomedical implants, the mechanisms how cells recognize and interact with the extracellular matrix (ECM) influenced by the biomaterials should be first explored. [108] There are abundant analytical methods to assess the cellular responses using quantitative or qualitative analyses including cell adhesion, proliferation, migration, differentiation and cell survival. [108]

The cell affinity of the biomaterials is known to be affected by the surface hydrophilicity, net charge, topography, chemical composition, and other biochemical-physical properties. [108, 109] For instance, the hydrophilic materials

induce a high level of the adhesion and spreading of the MC3T3-E1 cells. [110] Meanwhile, the negatively charged surface of the pure Ti can be converted to electropositive charge. [111] Ogawa and coworkers found after the treatment of UV-photofunctionalization, the titanium surface was full of cell-attracting terminals consisting of the RGD sequence of proteins or positively charged $TiO_2$ surface, which served as direct chemoattractants to cells without divalent cations such as $Ca^{2+}$ ions (**Fig. 1.7**). [111] There is also a consensus that roughening the implant surface at microscale and even at nanoscale can lead to a stronger bony response. [112] In addition, these above factors usually interact each other. The hydrophilicity of biomaterials is easily to be tailored by the surface topography and net charge. Furthermore, the investigation of biomolecular mechanism is essential and important for the biological effects between the implant and cells. For instance, the TiN coating on the NiTi alloy not only effectively prevented the release of Ni ions, but also promoted the formation of actin cytoskeleton and focal adhesion, increased energy metabolism, enhanced regulation of inflammation, and promoted amino acid metabolism, thus improved the cell functions (**Fig. 1.8**). [113]

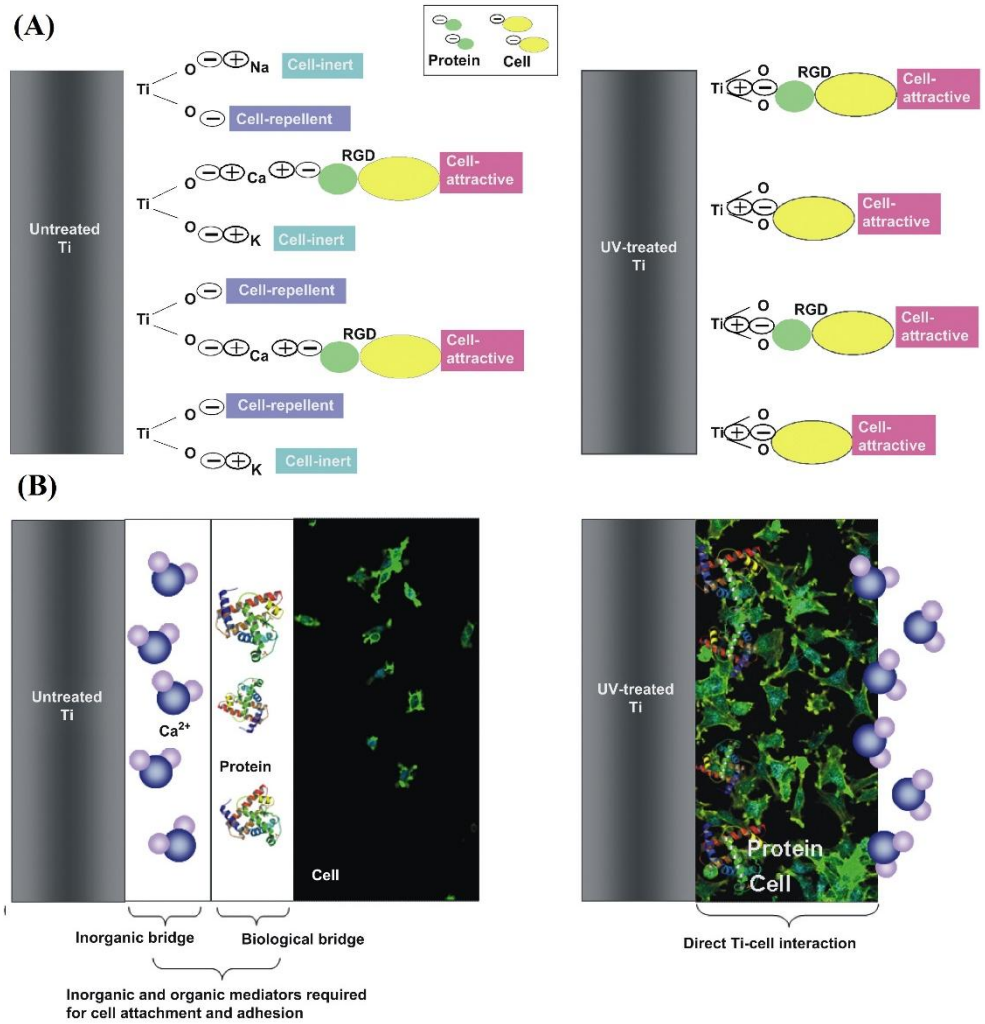


**Fig. 1.7.** Schematic description of the mechanism of electrostatic interactions underlying the UV-photofunctionalization of titanium dioxide surfaces: UV-mediated conversion of titanium surfaces from bioinert to bioactive. **(A)** Electrostatic interaction of $TiO_2$ surfaces with ions, proteins and cells. **(B)** A distinct interfacial layer formation at UV-photofunctionalized titanium surfaces. The image is reprinted from *Biomaterials*. [111]

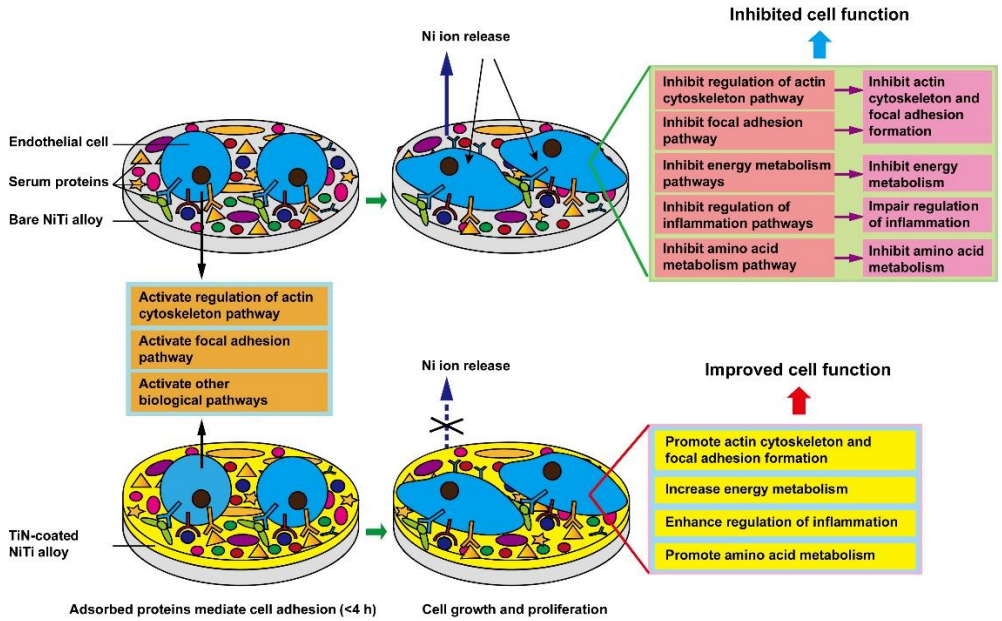


**Fig. 1.8.** Schematic diagram of mechanism for different effects of bare and TiN-coated NiTi alloys on endothelial cell function. The image is reprinted from *Biomaterials*. [113]

In theoretical simulations, the adsorption process of $Ca^{2+}$ ions on the surface of the biomaterial is widely used as the representative marker especially for bony tissue, [114, 115] since the $Ca^{2+}$ ion plays a prominent role bridging a net negatively charged substrate and anionic protein (integrin) for cell attachment. [111] Likewise, the deposition of calcium is the first step for the nucleation of the calcium phosphate, which is critical for the implants in contact with the bony tissue. [114, 115] Stefano and coworkers demonstrated that the $TiN_xO_y$ surface could initiate the

spontaneous nucleation of calcium phosphate because of the presence of a high electronegatively charged surface, which was about –0.80 (**Fig. 1.9**). [114] This phenomenon was also discovered on the surface of $TiO_2$, where the lowest electronegative charge of (011) surface was –0.45. [115]

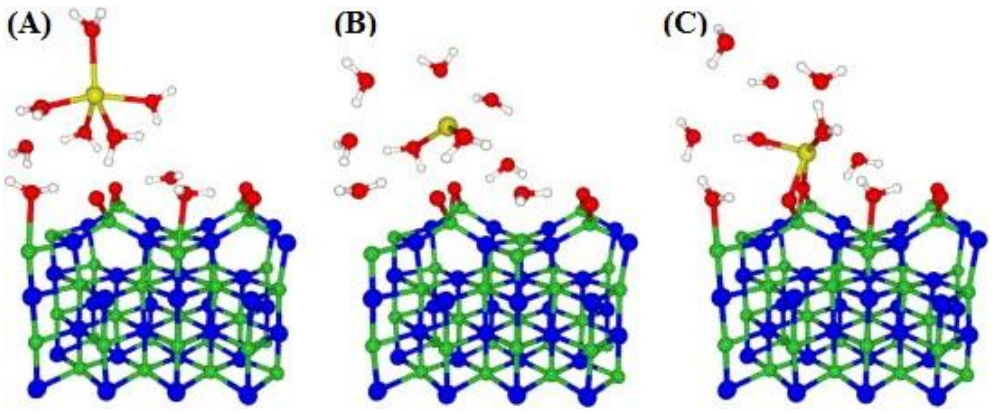


**Fig. 1.9.** Snapshots from a FPMD simulation at 300 K showing the adsorption of a $Ca^{2+}$ ion on the hydrated partially oxidized TiN surface. (A) Initial configuration, after relaxation of the system for ~300 fs keeping fixed the $Ca^{2+}$ ion; **(B)** After ~180 fs of simulated time; **(C)** After ~650 fs of simulated time. The image is reprinted from *Acta Materialia*. [114]

## 1.6 Purpose and Meaning of the Project

The biological responses to host tissue cells must be considered in the development of synthetic biomaterials. [108] In this thesis, the biocompatibility of selected MAX phases ($Ti_3AlC_2$, $Ti_3SiC_2$, and $Ti_2AlN$) will be systematically investigated using cell adhesion, proliferation, and differentiation with preosteoblasts and fibroblasts. Moreover, first-principles calculations will be employed to further reveal the general mechanism. The aim of the first part of this thesis is to explore the factors that affect the biocompatibility of MAX phases from the direction of different chemical compositions and to establish a reasonable mechanism to speculate the biocompatibility of other MAX phases. Then, the second part focuses on a practical dental application of $Ti_3C_2T_z$ nanosheets. The $Ti_3C_2T_z$ nanosheets will be embedded into PLA for exploring the potential application as a GBR membrane. To the best of our knowledge, this is the first effort to introduce MXene to polymer matrix for biomedical application. The uniaxial tensile test and *in vitro* tests will be employed to confirm whether $Ti_3C_2T_z$ nanosheets can enhance the mechanical properties and biocompatibility of PLA membrane.

# Chapter 2.

# Biocompatibility of Selected MAX Phases ($Ti_3AlC_2$, $Ti_3SiC_2$, and $Ti_2AlN$): *In Vitro* Tests and First-Principles Calculations

## 2.1 Introduction

In the previous references, the MAX phase has been introduced to the biomedical fields as a structural material or secondary phase to strengthen and toughen hydroxyapatite. [70-74] However, the previous works merely concentrate on the $Ti_3SiC_2$, and the reason for the inconsistent results remains indistinct. Since the biological responses to host tissue cells must be considered in the development of synthetic biomaterials, [108] it is essential to systematically evaluate the biocompatibility of MAX phase and establish the general mechanism for such a numerous family (more than 70 members).

In this chapter, the biocompatibility of selected MAX phases ($Ti_3AlC_2$, $Ti_3SiC_2$, and $Ti_2AlN$) will be systematically investigated using cell adhesion, proliferation, and differentiation with preosteoblasts and fibroblasts. Moreover, the first-principles calculations will be employed to further reveal the mechanism. The aim of this chapter is to explore the factors that affect the biocompatibility of MAX phases from the direction of different chemical compositions and to establish a reasonable mechanism to speculate the biocompatibility of other MAX phases.

## 2.2 Preparation and Characterization of $Ti_3AlC_2$, $Ti_3SiC_2$, and $Ti_2AlN$ Bulks

### 2.2.1 Preparation of $Ti_3AlC_2$, $Ti_3SiC_2$, and $Ti_2AlN$ Bulks

The $Ti_3AlC_2$ and $Ti_3SiC_2$ bulks were prepared from the commercial powders (98%, 300 mesh, Beijing Jinhezhi Materials Co., Ltd., China) using hot pressing sintering (ZT-60-24Y, Chenhua Co., Ltd., China) in an Ar atmosphere with a maximum pressure of 20 MPa. The heating rate was 10 °C/min, and the temperature was held for 2 h at 1350 °C for $Ti_3AlC_2$, and at 1400 °C for $Ti_3SiC_2$. The $Ti_2AlN$ bulks were synthesized *in-situ* using a pulse-electric-current-aided sintering device (HP D 25/3; FCT Group, Germany) with a Ti–1.1Al–TiN ground powder mixture (Ti and Al, 99.5%, 300 mesh; TiN, 300 mesh, 99.9%; Targets Research Center of General Research Institute for Nonferrous Metals, China) in an Ar atmosphere. The green pellet was then calcined in a graphite mold at 1350°C for 1 h with a maximum pressure of 30 MPa. [116]

All the specimens were processed into 10 mm × 10 mm slices (for cell adhesion and proliferation) and 20 mm × 20 mm slices (for cell differentiation)

using wire cut electric discharge machining. Before the *in vitro* tests, the slices were sequentially polished using 400, 800, and 1500 grit SiC paper. Then, the as-rinsed slices were disinfected in ethanol for 30 min and ultraviolet rays for at least 3 days in a clean bench.

### 2.2.2 Characterization of $Ti_3AlC_2$, $Ti_3SiC_2$, and $Ti_2AlN$ Bulks

#### 2.2.2.1 Characterization Methods

The chemical phase-analysis of the synthesized MAX phases were evaluated using X-ray Diffraction (XRD, Bruker AXS D8 Advance, Germany) with Cu $K_\alpha$ radiation and their spectra were collected at a step scan of 0.02° 2θ and a step time of 0.2 s. The microstructure was observed using field emission scanning electron microscope (SEM, Merlin Compact, ZEISS, Germany) equipped with energy dispersive spectroscopy (EDS, Thermo Scientific, USA). The surficial composition was detected using X-ray photoelectron spectroscopy (XPS, AXIS-His, Kratos, Japan). The hydrophilicity was evaluated based on the contact angle with approximately 10 μL of deionized water using a goniometer (Phoenix 300, Korea) at ambient atmosphere.

### 2.2.2.2 Discussion

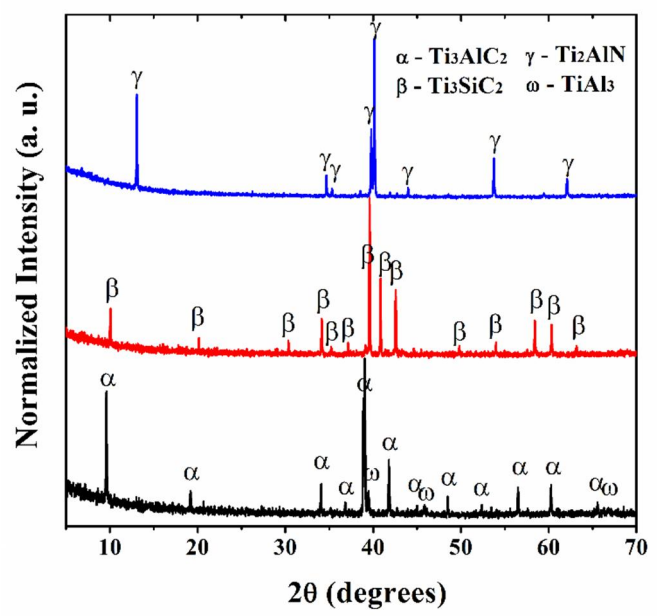


**Fig. 2.1.** XRD spectra of the self-prepared $Ti_3AlC_2$ (black line), $Ti_3SiC_2$ (red line), and $Ti_2AlN$ (blue line) bulks.

The phase composition of each self-made MAX phase bulk was determined using XRD. The spectra in **Fig. 2.1** indicated that all the MAX phase bulks possessed a high purity. In particular, for $Ti_3SiC_2$ and $Ti_2AlN$ bulks, no apparent impurity peaks were observed. For the $Ti_3AlC_2$ bulk, the amount of remaining intermetallic $TiAl_3$ was approximately 2 wt. % according to the supplier. However,

this intermetallic phase commonly exists in Ti–6Al–4V alloy, [117, 118] which is proverbially used as a commercial biomaterial. To the best of our knowledge, the related works did not note that $TiAl_3$ is harmful to the human body. Hence, we believe that these self-prepared bulks could be used as platforms to evaluate the biocompatibility of the corresponding MAX phases.

The SEM images showed that these platforms used for *in vitro* tests had dense body and similar morphology after being polished by the same 1500 grit SiC paper (**Fig. 2.2A-C**), which meant that during the following analysis of the biocompatibility of MAX phases, the influence from the morphology could be ignored. Moreover, the XPS spectra exhibited that besides the Ti-C bond or Ti-N bond belonged to the MAX phases (i.e. M-X bond), the Ti-O bond and Al-O bond existed on the surfaces of the $Ti_3AlC_2$ and $Ti_2AlN$, and the Ti-O bond and Si-O bond existed on that of $Ti_3SiC_2$, respectively (**Fig. 2.3-2.5**). The presence of oxygen on the surfaces of MAX phases was also detected by the analysis of EDS (**Table 2.1**). These results were consistent with the previous works, [119, 120] which attested that the MAX phases were covered by the partially oxidized layer. This partially oxidized layer was also discovered and demonstrated on the surfaces of TiC and TiN by the experiments and simulations. [114, 121]

The contact angle test with deionized water showed that the surface of $Ti_2AlN$ bulk (37.0°) was more hydrophilic than those of $Ti_3AlC_2$ bulk (44.4°) and $Ti_3SiC_2$ bulk (45.5°). Meanwhile, the contact angle of $Ti_2AlN$ bulk (37.0°) was also significantly lower than those of the commercial Ti–6Al–4V alloy (52.9°) and pure Ti (51.6°) as shown in **Fig. 2.6**.

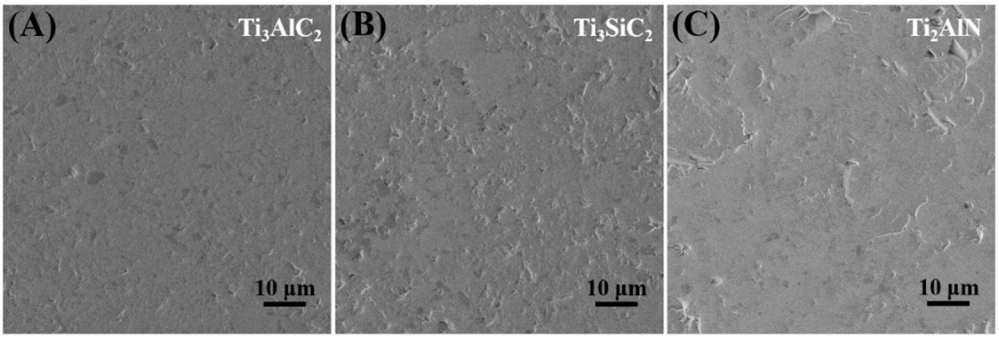


**Fig. 2.2.** SEM surface morphology of the self-prepared **(A)** $Ti_3AlC_2$, **(B)** $Ti_3SiC_2$, and **(C)** $Ti_2AlN$ bulks.

**Table 2.1.** EDS analysis of the self-prepared MAX phases used for *in vitro* tests.

| at. % | Ti | Al | Si | C | N | O |
|---|---|---|---|---|---|---|
| **$Ti_3AlC_2$** | 56.1±1.0 | 24.9±1.9 | - | 16.7±0.1 | - | 2.2±1.5 |
| **$Ti_3SiC_2$** | 57.6±0.3 | - | 20.0±0.6 | 17.8±0.3 | - | 4.6±1.0 |
| **$Ti_2AlN$** | 46.3±1.2 | 22.3±0.3 | - | - | 21.3±0.5 | 10.2±1.9 |

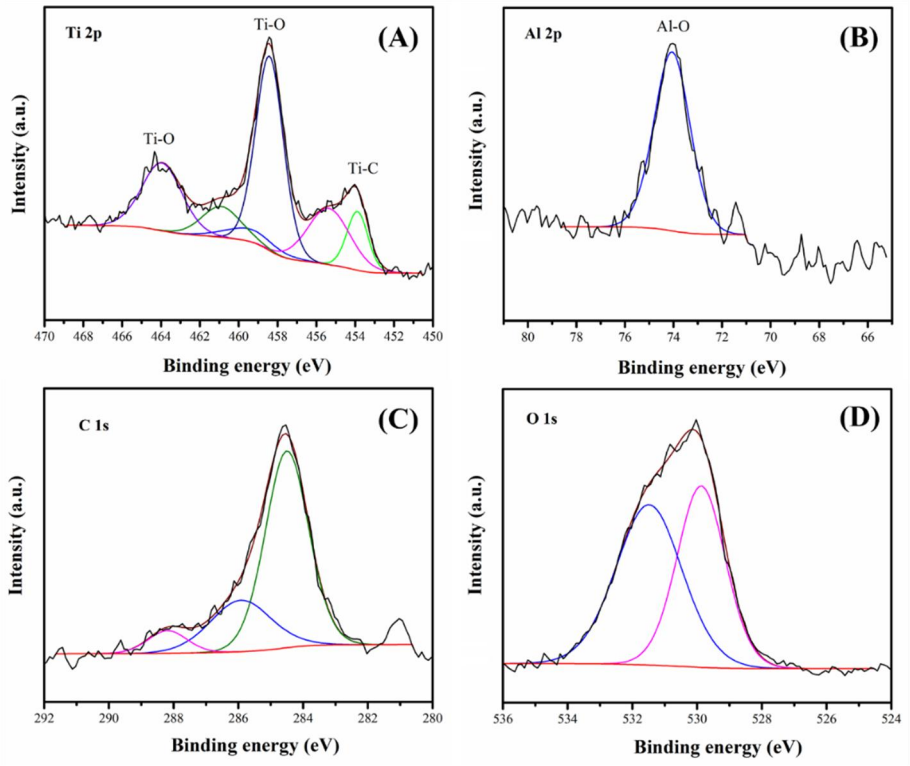


**Fig. 2.3.** XPS spectra of $Ti_3AlC_2$ bulks: **(A)** Ti 2p region, **(B)** Al 2p region, **(C)** C 1s region and **(D)** O 1s region.

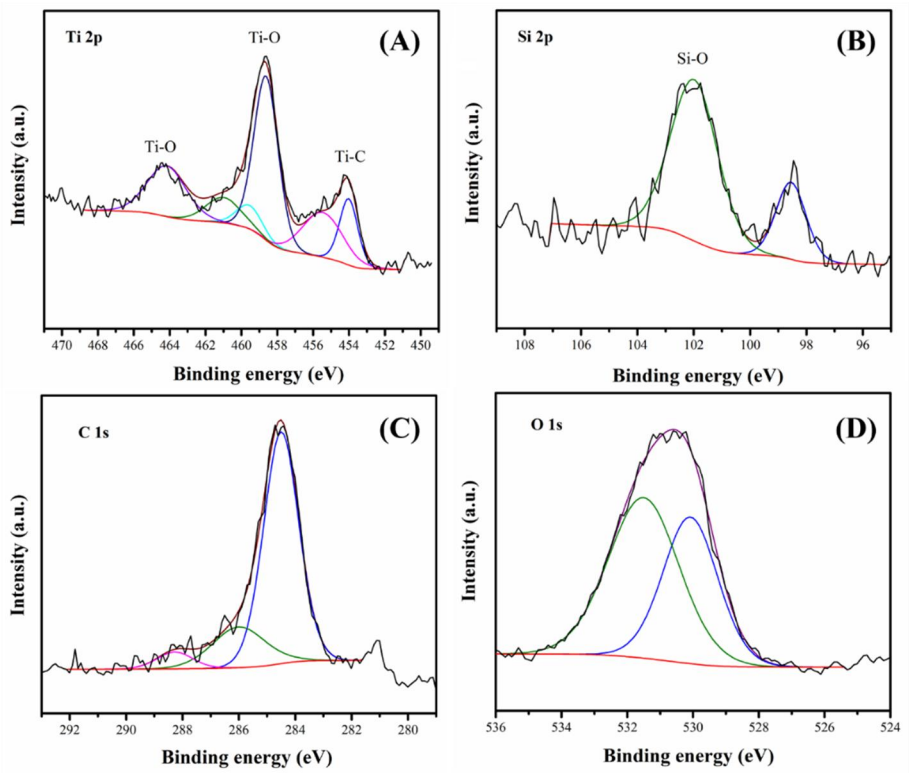


**Fig. 2.4.** XPS spectra of $Ti_3SiC_2$ bulks: **(A)** Ti 2p region, **(B)** Si 2p region, **(C)** C 1s region and **(D)** O 1s region.

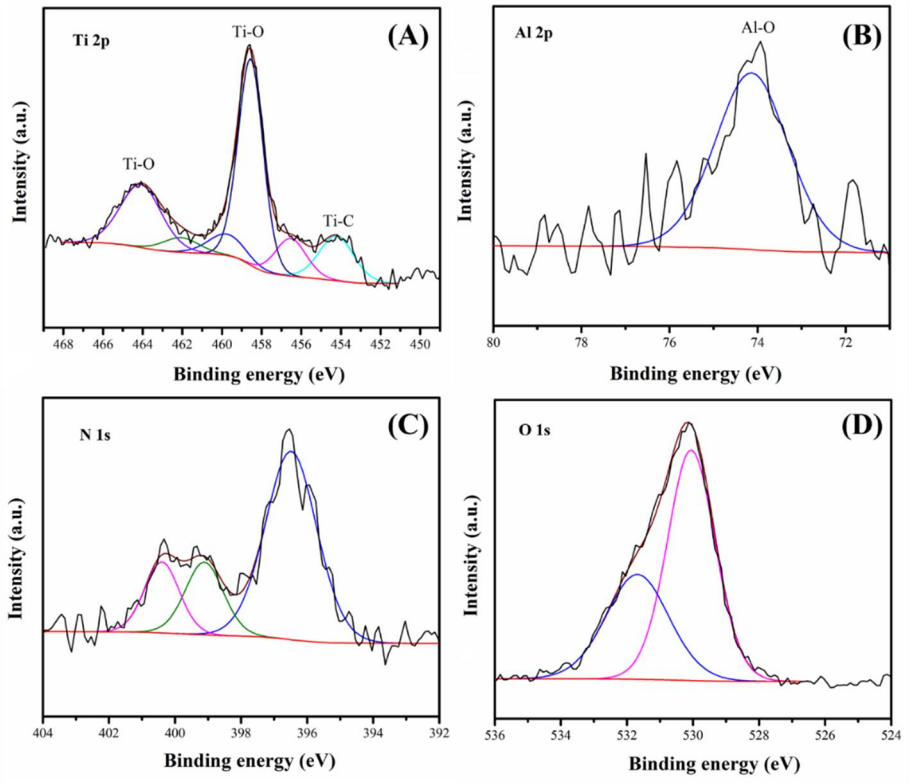


**Fig. 2.5.** XPS spectra of $Ti_2AlN$ bulks: **(A)** Ti 2p region, **(B)** Al 2p region, **(C)** N 1s region and **(D)** O 1s region.

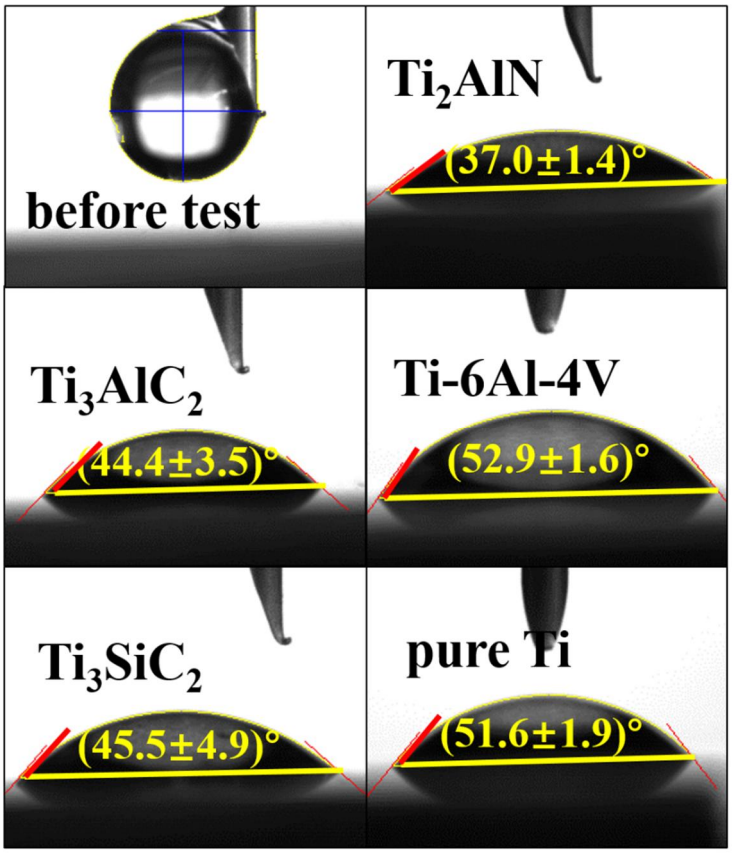


**Fig. 2.6.** Hydrophilicity of the self-prepared $Ti_3AlC_2$, $Ti_3SiC_2$, and $Ti_2AlN$ bulks determined by the contact angle with deionized water compared with pure Ti and Ti-6Al-4V alloy.

## 2.3 Biocompatibility of MAX Phases: *In Vitro* Tests

### 2.3.1 Biological Behaviors of Preosteoblasts on the MAX Phases

#### 2.3.1.1 *In Vitro* Tests Methods

Since the bony tissue is the main service condition during the dental implantation surgery, a mouse preosteoblast cell line (MC3T3-E1; ATCC, CRL-2593, USA) was first employed in the *in vitro* tests. All the cells were cultivated in alpha-minimum essential medium (α-MEM, Welgene Co., Ltd., Korea) with fetal bovine serum (FBS; Cellgro, USA) (10% FBS for preosteoblasts) and 1% penicillin streptomycin (Pen Strep; Life Technologies Co., Ltd., USA) in a humidified incubator (Sanyo Co., Ltd., Japan) with 5% $CO_2$ at 37 °C. A dye-exclusion assay (Trypan blue) was used to count the cells.

The cell adhesion was determined based on the preosteoblasts (1 mL, $1\times10^4$ cells/mL) after being cultured on the surface of the $Ti_3AlC_2$, $Ti_3SiC_2$, $Ti_2AlN$, Ti–6Al–4V alloy and pure Ti bulks for 3 h. The cells were then stained using phalloidin (Life Technology Co., Ltd., USA) and 4', 6-diamidino-2-phenylindole (DAPI, Life Technology Co., Ltd., USA). The morphology and distribution were recorded using the confocal laser scanning microscopy (CLSM; FluoView FV1000, Olympus Co.,

Ltd., Japan). The spreading area of the preosteoblasts was calculated using *ImageTool 3.0* from 50 CLSM images for each material at ×20 magnification.

The MTS (3-(4,5-dimethylthiazol-2-yl)-5-(3-carboxymethoxyphenyl)-2-(4-sulfophenyl)-2H-tetrazolium) assay was used to evaluate the cell proliferation. After being cultured for 3, 5 or 7 days, the optical density (OD) of the formazan product was detected using a microplate reader (EZ Read 400, Biochrom Ltd. UK) at 490 nm. The CLSM was also used to examine the amount and distributions of the preosteoblasts after incubation for 7 days for verification.

The alkaline phosphatase (ALP) assay was applied to determine the osteogenic differentiation. After incubation for 12 days, the total protein of the cells was determined using the Bio-Rad protein assay kit (Bio-Rad Co., Ltd., USA) based on a series of bovine serum albumin (BSA; Sigma) standards. Then, the ALP activity was predicted based on the color change from p-nitrophenyl phosphate (pNPP, Sigma) to p-nitrophenol (pNP). The amount of ALP was calculated based on the absorbance value at 405 nm (OD value) per milligram of total cellular protein.

All the experiments were conducted with at least three parallel samples. The results are expressed as the mean ± standard deviation. A value of $p < 0.05$ was

considered statistically significant according to the Student's t-test method using *Statistical Product and Service Solutions* software.

### 2.3.1.2 Discussion

To evaluate the adhesive behavior of the preosteoblast on the surface of $Ti_3AlC_2$, $Ti_3SiC_2$, $Ti_2AlN$, Ti–6Al–4V alloy, and pure Ti bulks, CLSM was employed. As observed in **Fig. 2.7**, the cells attached on all these materials very well. Compared with the Ti alloy and pure Ti, the spreading of preosteoblast on the MAX phase, particularly on the $Ti_2AlN$ was promoted in the initial adhesion stage. Based on the 50 CLSM images (shown in **Fig. 2.8** and **Fig. 2.9**), the cell spreading area on the $Ti_2AlN$ calculated using the *ImageTool 3.0* was 2901 $\mu m^2$/cell, which was larger than that on the Ti alloy (2372 $\mu m^2$/cell) or pure Ti (2450 $\mu m^2$/cell) (**Fig. 2.8**). Because the hydrophilic materials induced a higher level of the adhesion and spreading of the MC3T3-E1 cells, [110] the contact angle results with deionized water corroborated these findings. The more hydrophilic $Ti_2AlN$ (37.0°) exhibited better initial cell attachment compared with the commercial Ti–6Al–4V alloy and pure Ti (52.9° and 51.6° respectively, as shown in **Fig. 2.6**).

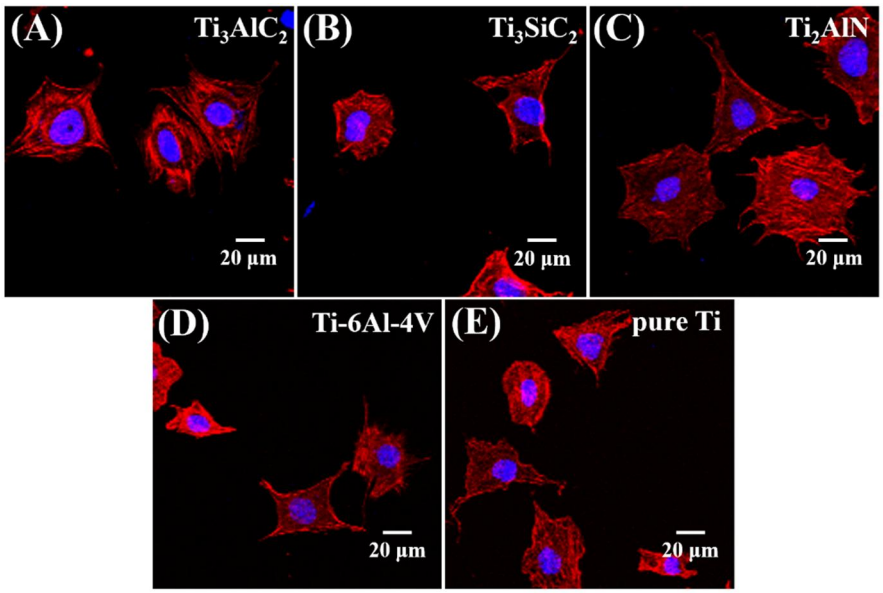


**Fig. 2.7.** Typical CLSM images used to determine the morphology of MC3T3-E1 cells attached on the surfaces of **(A)** $Ti_3AlC_2$, **(B)** $Ti_3SiC_2$, **(C)** $Ti_2AlN$, **(D)** Ti–6Al–4V alloy, and **(E)** pure Ti specimens after incubation for 3 h. Phalloidin and DAPI were used to stain the filamentous actin (red) and nucleus (blue), respectively. The seeding cell density was $1\times10^4$ cells/mL.

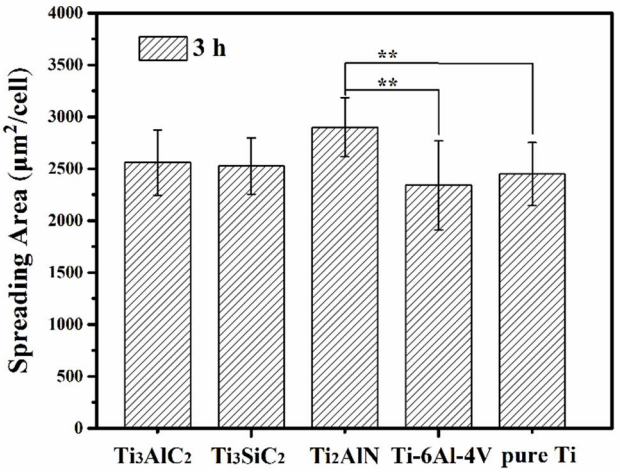


**Fig. 2.8.** Spreading areas of the preosteoblasts attached on the $Ti_3AlC_2$, $Ti_3SiC_2$, $Ti_2AlN$, Ti–6Al–4V alloy, and pure Ti specimens, which was obtained from the calculation of *ImageTool 3.0* using fifty CLSM images (**Fig. 2.9**) for each material at ×20 magnification. (**$p < 0.01$)

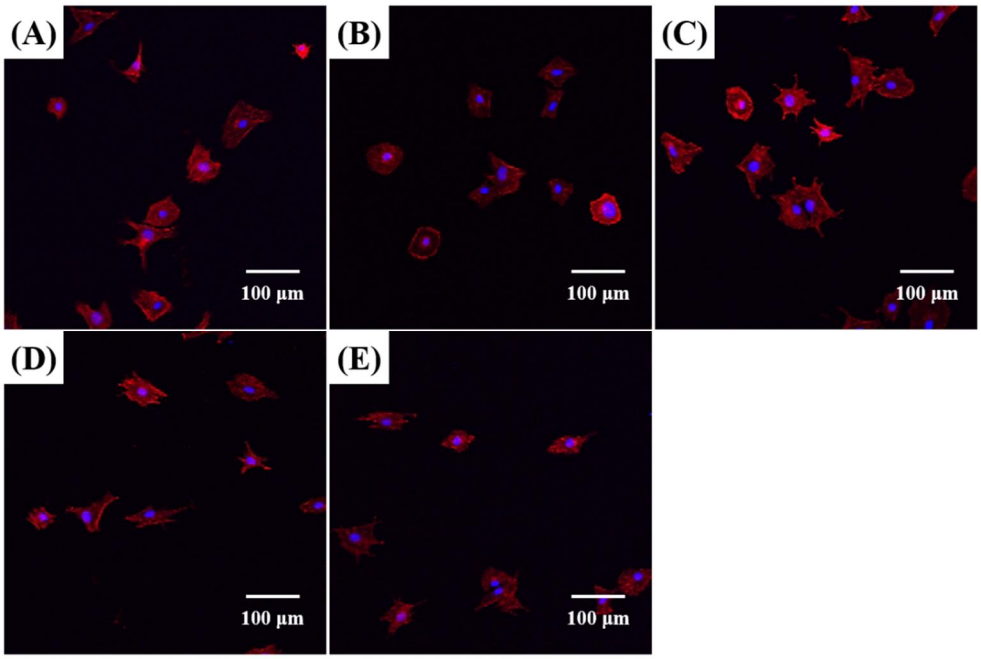


**Fig. 2.9.** Typical CLSM images used for calculating the spreading area of the preosteoblasts on the surfaces of **(A)** $Ti_3AlC_2$, **(B)** $Ti_3SiC_2$, **(C)** $Ti_2AlN$, **(D)** Ti–6Al–4V alloy, and **(E)** pure Ti specimens after incubation for 3 h. Phalloidin and DAPI were used to stain the filamentous actin (red) and nucleus (blue), respectively. The seeding cell density was $1\times10^4$ cells/mL.

The viability of the preosteoblasts was then characterized by MTS assay and direct CLSM observation. Based on **Fig. 2.10**, the MAX phase exhibited non-toxicity on the preosteoblast, and the cells actively proliferated on all the materials. Among the selected MAX phases, $Ti_2AlN$ exhibited the best performance

based on the optical density value. Moreover, the cell viability in the $Ti_2AlN$ group was even higher than that in the commercial Ti–6Al–4V alloy and was comparable to that in the pure Ti after 7 days of incubation. This phenomenon was also supported by the distribution of the preosteoblasts directly observed using CLSM images (**Fig. 2.11**). In contrast to $Ti_3AlC_2$, $Ti_3SiC_2$, and Ti–6Al–4V alloy, a larger number of preosteoblasts was universally distributed on the $Ti_2AlN$.

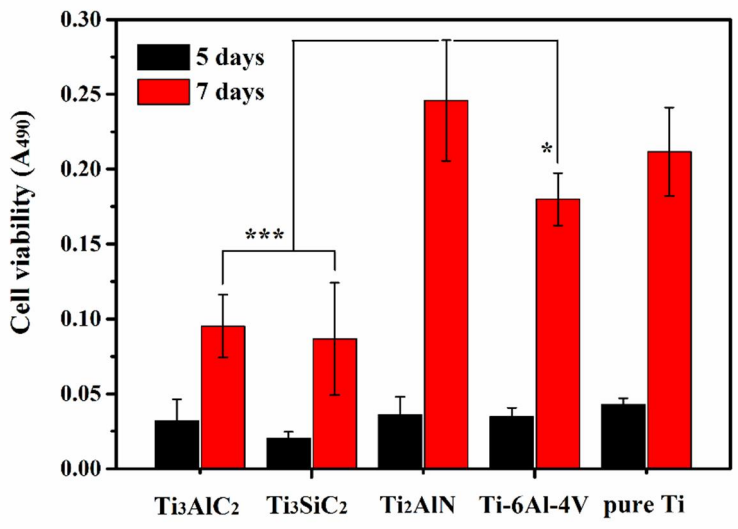


**Fig. 2.10.** MTS assay for determining the cell viability of MC3T3-E1 cells on the $Ti_3AlC_2$, $Ti_3SiC_2$, $Ti_2AlN$, Ti–6Al–4V alloy, and pure Ti specimens after 5-day and 7-day incubation. The seeding cell density was $1\times10^4$ cells/mL. (*$p < 0.05$, ***$p < 0.001$)

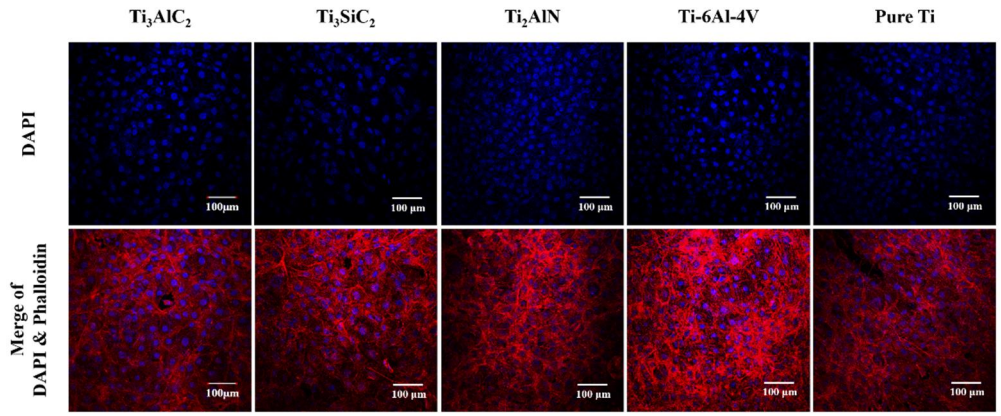


**Fig. 2.11.** Typical CLSM image used to determine the corresponding distribution of MC3T3-E1 cells grown after 7 days. Phalloidin and DAPI were used to stain the filamentous actin (red) and nucleus (blue), respectively. The seeding cell density was $1\times10^4$ cells/mL.

During the osteoblastic differentiation, ALP was formed to promote the hydrolysis of phosphate esters, which was used as an early marker to determine the differentiation degree of preosteoblasts. [122, 123] In this study, the ALP activity of the MC3T3-E1 cells cultured on the surfaces of $Ti_3AlC_2$, $Ti_3SiC_2$, $Ti_2AlN$, Ti–6Al–4V alloy, and pure Ti for 12 days was recorded using microplate reader (**Fig. 2.12**). Among the selected MAX phases, the ALP activity in the $Ti_2AlN$ group was significantly higher than that in the other two phases. The ALP activity in the $Ti_2AlN$ group was almost twofold and fourfold of that in the $Ti_3AlC_2$ and $Ti_3SiC_2$

group, respectively. Although a noticeable difference of the ALP activity between $Ti_2AlN$ group and pure Ti group was difficultly detected, the osteogenic differentiation of preosteoblasts in the $Ti_2AlN$ group was superior to that in the commercial Ti–6Al–4V alloy group.

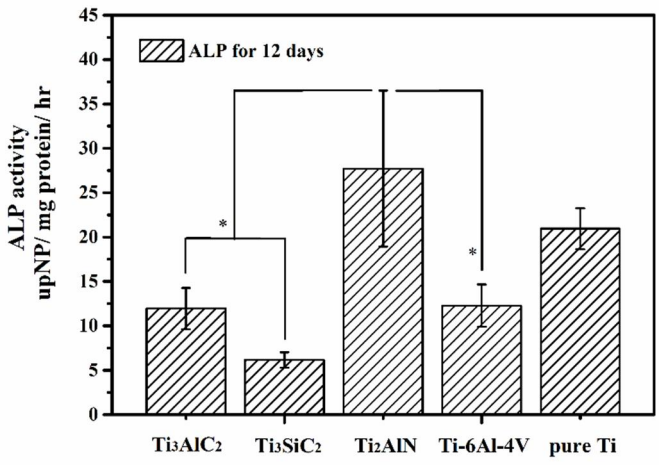


**Fig. 2.12.** ALP activity used to determine the differentiation of MC3T3-E1 cells after 12-day incubation on the $Ti_3AlC_2$, $Ti_3SiC_2$, $Ti_2AlN$, Ti–6Al–4V alloy, and pure Ti specimens. The seeding cell density was $1\times10^4$ cells/mL. (*$p < 0.05$)

### 2.3.2 Biological Behaviors of Fibroblasts on the MAX Phases

Soft tissue is another important service condition during the dental implantation surgery. Herein, the mouse fibroblast cell line (L929; derivative of strain L) was employed to evaluate the biocompatibility of MAX phases under the soft tissue condition. The fibroblasts were cultured using the same method as that for the preosteoblasts except the culture medium added with 5% FBS. The procedures for cell adhesion and proliferation were also the same as those shown in **2.2.1.1**.

The typical CLSM images in the **Fig. 2.13A** showed that the similar cell adhesive behaviors emerged on the $Ti_3AlC_2$, $Ti_3SiC_2$, $Ti_2AlN$, Ti–6Al–4V alloy, and pure Ti specimens after seeding for 3 h. The cell proliferation determined from the MTS assay and CLSM images also revealed a little difference (**Fig. 2.13B-C**). The mean values of each group obtained from the MTS assay at 5 days were at similar levels and the error bars overlapped. However, during the initial incubation stage (approximately 3 days), the fibroblasts proliferated faster on the $Ti_2AlN$ than on the other phases. These phenomena could be ascribed to the strong viability of the fibroblasts, whose proliferation rate was almost three times than that of the osteoblasts. [124] It was very difficult to distinguish the slight differences between

these materials. In other words, the biocompatibility of these MAX phases was as good as the references, Ti–6Al–4V alloy and pure Ti, under fibroblastic condition.

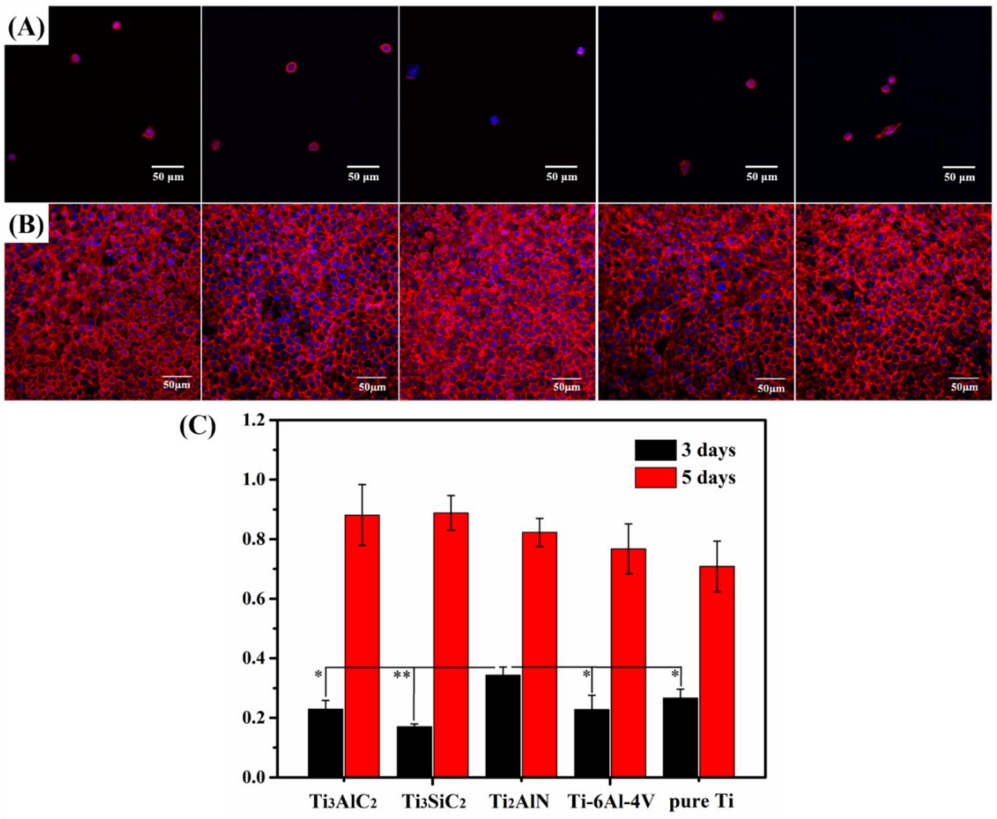


**Fig. 2.13.** Biological behaviors of L929 cells on the $Ti_3AlC_2$, $Ti_3SiC_2$, $Ti_2AlN$, Ti–6Al–4V alloy, and pure Ti specimens: **(A)** Morphology and distribution of L929 cells after incubation for 3 h; **(B-C)** Cell proliferation determined from CLSM image (7 days) and MTS assay after 3-day and 5-day incubation. Phalloidin and DAPI were used to stain the filamentous actin (red) and nucleus (blue), respectively.

The seeding cell density was $1\times10^4$ cells/mL. (*$p < 0.05$, **$p < 0.01$)

## 2.4 Theoretical Calculation of $Ca^{2+}$ Ions Absorbed on the MAX Phases

The $Ca^{2+}$ ion plays a prominent role bridging a net negative substrate and anionic protein (integrin) for cell attachment. [111] The deposition of calcium is the first step for the nucleation of the calcium phosphate, which is critical for the implants in contact with the bony tissue. [114, 115] Hence, the simulation of the process of the $Ca^{2+}$ adsorbed on the substrate can be used to evaluate the biocompatibility of the biomaterials. This typical process not only simplifies the diverse and complex biological interactions, but also reduces the workload for the calculation. For instance, the negative charge is calculated to confirm this process in the works of $TiO_2$ and TiN. [114, 115] Herein, a new quantitative indicator (the binding energy of the absorbed $Ca^{2+}$ ions with the substrate) is used to directly evaluate this absorption process since the surfaces of MAX phases ($Ti_3AlC_2$, $Ti_3SiC_2$, $Ti_2AlN$) have been proven to have the negative charge in the normal pH range of body fluids according to the analysis of zeta potential. [125-128]

In this section, the first-principles calculations were preformed to investigate the phenomenon of the $Ca^{2+}$ ion bound on these selected MAX phases with the CASTEP package. [129] The general strategy was as follows: **(1)** Simplify the

surficial structures of MAX phases by selecting the stable representative surfaces; **(2)** Establish the partially oxidized the surficial structure; **(3)** Optimize the process of the $Ca^{2+}$ ion absorbed on the above partially oxidized surfaces. In details, the ultrasoft pseudopotentials [130] and the plane-wave basis were adopted for the spin-polarized density functional theory computation. A kinetic-energy cutoff for plane-wave expansion was set to 420 eV in our calculations. The generalized gradient approximation (GGA) was expressed by the Perdew–Burke–Ernzerhof (PBE) functional for the exchange-correlation potential. [131, 132] The effect of van der Waals (vdW) interactions based on the PBE functional was included explicitly using the empirical correction scheme of Grimme. [133] The vacuum distance was set to 16 Å along the z direction to avoid the artificial interlayer interaction caused by periodic boundary condition. All the atoms in the unit cell were fully relaxed until the convergence criterion on each atom was less than $10^{-5}$ eV in energy and 0.03 eV $Å^{-1}$ in force. The Brillouin zones were sampled with a 9×9×1 k-point grid using Monkhorst–Pack scheme. [134]

### 2.4.1 Establishment of Surface Structure of the Partially Oxidized MAX Phases

In the light of the layered hexagonal microstructure of MAX phases, the (100) and (001) surfaces were selected as representative surfaces based on the experimental XRD data (**Fig. 2.14**). To assess the stability of the naked surface slab, we first computed the cohesive energy ($E_c$) of the (100) and (001) surface slabs, which was defined as:

$$E_c = \left(E_{slab} - n_{Ti}E_{Ti} - n_{Al/Si}E_{Al/Si} - n_{N/C}E_{N/C}\right)/n_{tot},$$

where $E_{slab}, E_{Ti}, E_{Al/Si}$, and $E_{N/C}$ were the total energies of a surface slab, single Ti atom, single Al or Si atom and single N or C atom, respectively, and $n_{tot}, n_{Ti}, n_{Al/Si}$, and $n_{N/C}$ were the total number of atoms and the respective number of Ti, Al (or Si) and N (or C) atoms in the supercell. To further evaluate the stability of the formation of the naked surface slabs relative to the simple stable substances, we defined the formation energy as:

$$E_f = \left(E_{slab} - n_{Ti}\mu_{Ti} - n_{Al/Si}\mu_{Al/Si} - n_{N/C}\mu_{N/C}\right)/n_{tot},$$

where the chemical potentials $\mu_{Ti}, \mu_{Al/Si}$, and $\mu_{N/C}$ were defined as the energies per atom in bulk Ti, bulk Al or Si, and a nitrogen molecule or graphite, respectively.

$E_c$ and $E_f$ of these surface slabs are listed in **Table 2.2**.

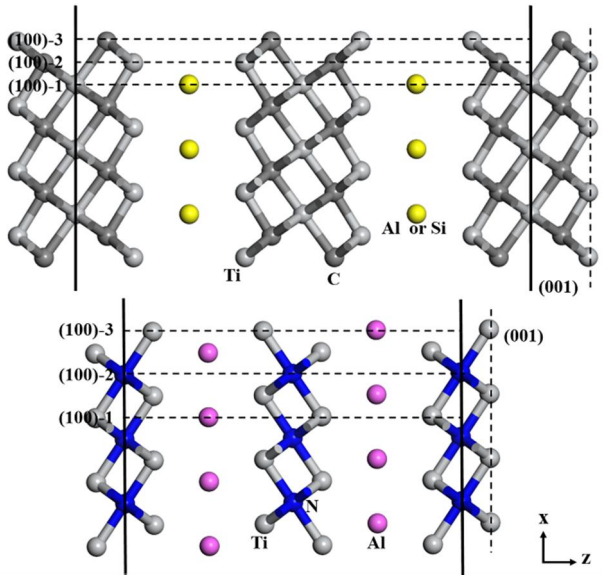


**Fig. 2.14.** Different configurations of the (100) and (001) surfaces for the $Ti_3AlC_2$, $Ti_3SiC_2$, and $Ti_2AlN$.

All the bare (001) surfaces were the most stable and the easiest to be observed experimentally because they had the lowest $E_c$ and $E_f$ (**Fig. 2.1** and **Table 2.2**). However, for the bare (100) surface, there were three possible configurations for the MAX phases. As shown in **Fig. 2.14** and **Table 2.2**, the (100)-3 configuration could be transformed into the (100)-1 configuration for $Ti_2AlN$, because the single-coordinated Ti atom was unstable and readily reacted with water or oxygen. However, the single-coordinated Ti atom also tended to be removed from the

surface of the (100)-2 configuration to form a planar TiC surface, which was similar to the structure of the (100)-1 configuration for the $Ti_3AlC_2$ and $Ti_3SiC_2$ after exposure to oxygen or water. Thus, the (100)-1 and (100)-2 configurations of $Ti_2AlN$ and the (100)-1 and (100)-3 configurations of both $Ti_3AlC_2$ and $Ti_3SiC_2$ were selected to investigate the following adsorption of the $Ca^{2+}$ ion on the (100) surface.

**Table 2.2.** Cohesive energy ($E_c$) and formation energy ($E_f$) of the naked surface slabs of MAX phases for each configuration shown in **Fig. 2.14**.

| surface | $E_c$ eV/atom | $E_f$ eV/atom | surface | $E_c$ eV/atom | $E_f$ eV/atom |
|---|---|---|---|---|---|
| TAC001 | –7.31 | –0.71 | TSC100-3 | –6.78 | –0.15 |
| TAC100-1 | –6.58 | –0.26 | TAN001 | –6.45 | –1.17 |
| TAC100-2 | –6.55 | –0.20 | TAN100-1 | –5.95 | –0.79 |
| TAC100-3 | –6.63 | –0.15 | TAN100-2 | –5.99 | –0.88 |
| TSC001 | –7.47 | –0.75 | TAN100-3 | –5.85 | –0.63 |
| TSC100-1 | –6.66 | –0.19 | r$TiO_2$110 | - | - |
| TSC100-2 | –6.62 | –0.026 | | | |

TAC, TSC and TAN represent $Ti_3AlC_2$, $Ti_3SiC_2$ and $Ti_2AlN$, respectively, in this table.

The MAX phase should be passivated by an oxidation reaction on the surface in ambient atmosphere. [135] From our experimental tests, the presence of the oxygen on the surface of MAX phases were also confirmed by the analyses of XPS and EDS (**Table 2.1** and **Fig. 2.3-2.5**). This phenomenon was widespread in the other titanium-based ceramics. For instance, Piscanec et al. reported that a partially oxidized TiN surface can be used as a preferential site for the deposition of $Ca^{2+}$ ion. [114] Herein, we tested various possible partially oxidized configurations followed by atomic relaxations.

The optimized stable configurations of $Ti_3AlC_2$, $Ti_3SiC_2$, and $Ti_2AlN$ were presented in **Fig. 2.15**. The O atom was bound to three Ti atoms located above the N/C atom in the (001) configuration. Herein, the O atom was probably bound with the H atom to form a hydroxyl group (OH). However, this process was energetically unfavorable according to the formation energy, where

$$(\mathrm{F} = E_{slab+mO+nH} - E_{slab+mO} - n\mu_H) > 0$$

especially under alkaline conditions. For the (100)-1 configuration of $Ti_2AlN$, the

bridging OH group (F= –0.43 eV) was coordinated by two Ti atoms bound to two N atoms, whereas the threefold-coordinated O atom was coordinated by one Al atom and two Ti atoms bound to three N atoms. Rodriguez et al. have shown that the CTiTi hollow is the most stable site for the adsorption of O atoms on the TiC (001) surface. [136] In addition, for the (100)-1 configurations of $Ti_3AlC_2$ and $Ti_3SiC_2$, one O atom was coordinated by two Ti atoms bound to three C atoms and by one C atom bound to five Ti atoms on the planar TiC surface, which was consistent with reports of Rodriguez et al. The other free surficial Ti and Al atoms were bound to the threefold-coordinated O atoms. The oxidation behaviors of the (100)-2 configuration for $Ti_2AlN$ and the (100)-3 configuration for $Ti_3AlC_2$ and $Ti_3SiC_2$ were similar to that of the (100)-1 configuration, in which the O atom was also bound to two Ti atoms and an Al atom for $Ti_2AlN$ and the CTiTi hollow for $Ti_3AlC_2$ and $Ti_3SiC_2$, respectively (as observed in **Fig. 2.15**).

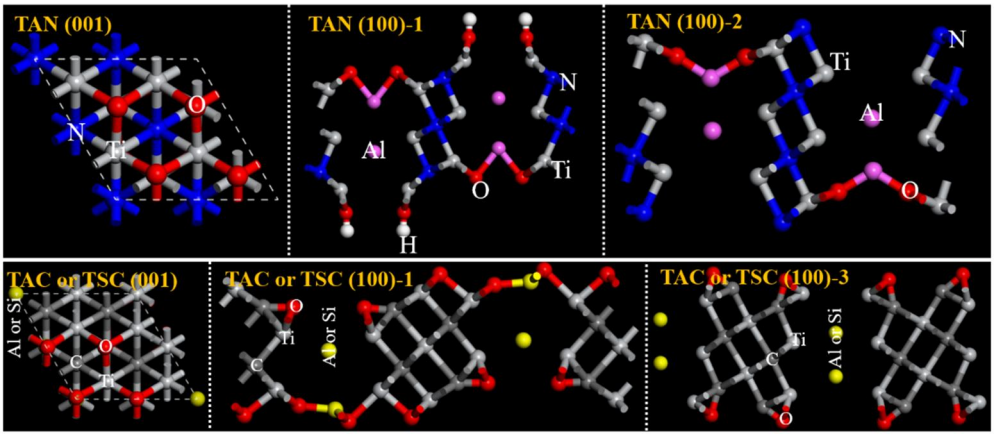


**Fig. 2.15.** Optimized configurations for partially oxidized surfaces of the $Ti_3AlC_2$, $Ti_3SiC_2$, and $Ti_2AlN$.

### 2.4.2 Optimization of Absorption of $Ca^{2+}$ Ions

**Table 2.3.** $\Delta E_{bind}$ of the $Ca^{2+}$ ions bound on the different positions for each configuration shown in **Fig. 2.16** and **Fig. 2.17**.

| Surface | Position 1 | Position 2 | Position 3 | Position 4 |
|---|---|---|---|---|
| TAC001 | **–19.14** | | | |
| TAC100-1 | –14.45 | **–16.28** | –16.03 | |
| TAC100-3 | **–15.90** | –15.05 | | |
| TSC001 | **–19.96** | | | |
| TSC100-1 | –13.98 | **–16.94** | –14.95 | |
| TSC100-3 | **–15.63** | –14.80 | | |
| TAN001 | **–24.71** | | | |
| TAN100-1 | –15.40 | **–18.53** | –16.39 | –16.02 |

| | | |
|---|---|---|
| TAN100-2 | **<u>–15.74</u>** | –14.43 |
| $rTiO_2$110 | **<u>–21.83</u>** | |

TAC, TSC and TAN represent $Ti_3AlC_2$, $Ti_3SiC_2$ and $Ti_2AlN$, respectively, in this table. The $\Delta E_{bind}$ for optimal position is marked with bold and underline. Unit: eV/atom

We also tested the possible adsorption sites of $Ca^{2+}$ ions on the surface of partially oxidized configurations of $Ti_3AlC_2$, $Ti_3SiC_2$, and $Ti_2AlN$ (shown in **Table 2.3** and **Fig. 2.16-2.17**). The preferred adsorption site of $Ca^{2+}$ ions on the surface and the corresponding binding energy were shown in **Fig. 2.18** and **Table 2.3** (**<u>the bold values</u>**)**.** The binding energy was defined as:

$$\Delta E_{bind} = \left(E_{poMAX+mCa^{2+}} - E_{poMAX} - mE_{Ca^{2+}}\right)/m$$

where $E_{Ca^{2+}}$, $E_{poMAX}$, and $E_{poMAX+mCa^{2+}}$ represented the total energies of a single $Ca^{2+}$ ion, the specific partially oxidized surface of the MAX phase, and the corresponding configuration after $Ca^{2+}$ ions absorbed on this surface, respectively. *m* was the number of absorbed $Ca^{2+}$ ions.

In the (001) configuration, the $Ca^{2+}$ ion was coordinated by three O atoms (**Fig. 2.18**). The binding energies of the $Ca^{2+}$ ion on the (001) configurations of $Ti_3AlC_2$, $Ti_3SiC_2$, and $Ti_2AlN$ were –19.14, –19.96, and –24.71 eV/atom, respectively. In

addition, the $Ca^{2+}$ ion was coordinated by four O atoms in the (100)-1 configuration (**Fig. 2.18**), and the binding energies were –16.28, –16.94, and –18.53 eV/atom for $Ti_3AlC_2$, $Ti_3SiC_2$, and $Ti_2AlN$, respectively. For the (100)-2 configuration of $Ti_2AlN$, the $Ca^{2+}$ ion tended to bind to two threefold-coordinated N atoms with a binding energy of –15.74 eV/atom, whereas the $Ca^{2+}$ ion preferred to bind to two C atoms and one O atom in the (100)-3 configuration with binding energies of –15.90 (–15.63) eV/atom for $Ti_3AlC_2$ ($Ti_3SiC_2$), respectively (**Fig. 2.18**). For comparison, we studied the adsorption of $Ca^{2+}$ ions on a rutile $TiO_2$ (110) surface, which was the most stable representative surface of $TiO_2$ [115]. The $Ca^{2+}$ ion was coordinated by two bridging O atoms and two terminal O atoms of the OH group, which was consistent with the result of Svetina's work [115]. The binding energy was –21.83 eV, which was considered the source of the good biocompatibility of the $TiO_2$.

In summary, the partially oxidized (001) surface of the $Ti_2AlN$ exhibited a stronger affinity to the $Ca^{2+}$ ion, in contrast with that of $TiO_2$. However, the binding strength of the $Ca^{2+}$ ion on the partially oxidized (100) surfaces of $Ti_2AlN$ and the (001) and (100) surfaces of both $Ti_3AlC_2$ and $Ti_3SiC_2$ were weaker than that on $TiO_2$. These results indicated that the partially oxidized $Ti_2AlN$ exhibited improved biocompatibility with respect to the partially oxidized $Ti_3AlC_2$ and $Ti_3SiC_2$, and

comparable biocompatibility to the pure Ti, which was in excellent agreement with the experimental observations.

It was worth the whistle that the binding energy of $Ca^{2+}$ ion on the (001) surface was much stronger than that on the (100) surface for each MAX phase (**Table 2.3**). This phenomenon indicated that the MXenes ($Ti_3C_2T_z$ and $Ti_2NT_z$), which mainly were composed of the (001) surfaces, had a good affinity to the $Ca^{2+}$ ion, and also the biocompatibility.

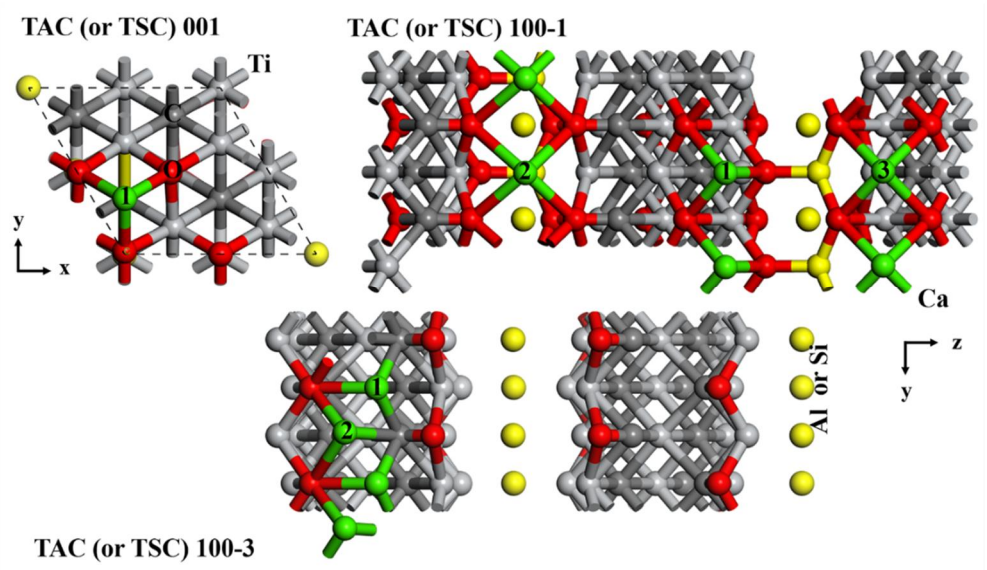


**Fig. 2.16.** Schematic diagram of the possible positions that the $Ca^{2+}$ ions (green spheres) bound on the $Ti_3AlC_2$ and $Ti_3SiC_2$. (TAC and TSC represent $Ti_3AlC_2$ and

$Ti_3SiC_2$, respectively)

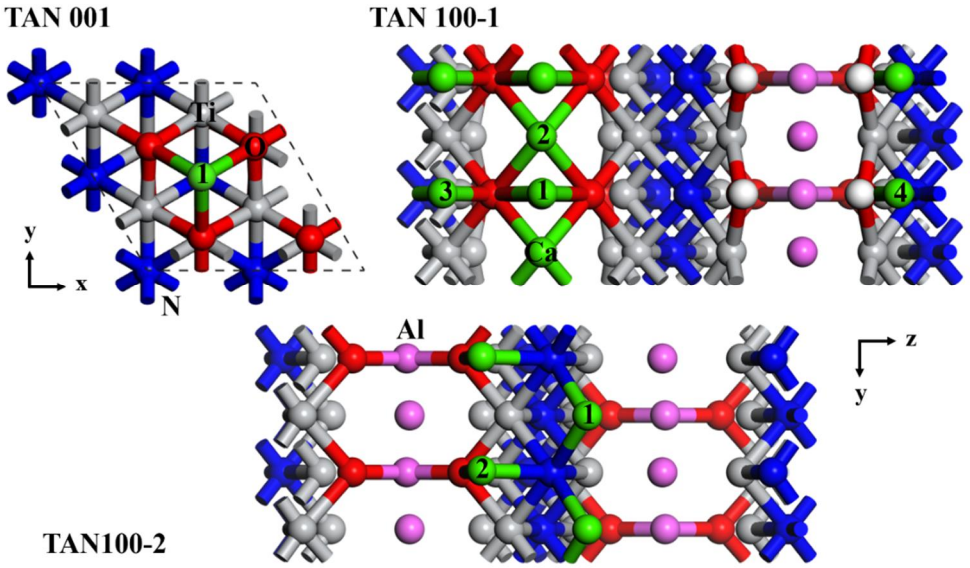


**Fig. 2.17.** Schematic diagram of the possible positions that the $Ca^{2+}$ ions (green spheres) bound on the $Ti_2AlN$. (TAN represents $Ti_2AlN$)

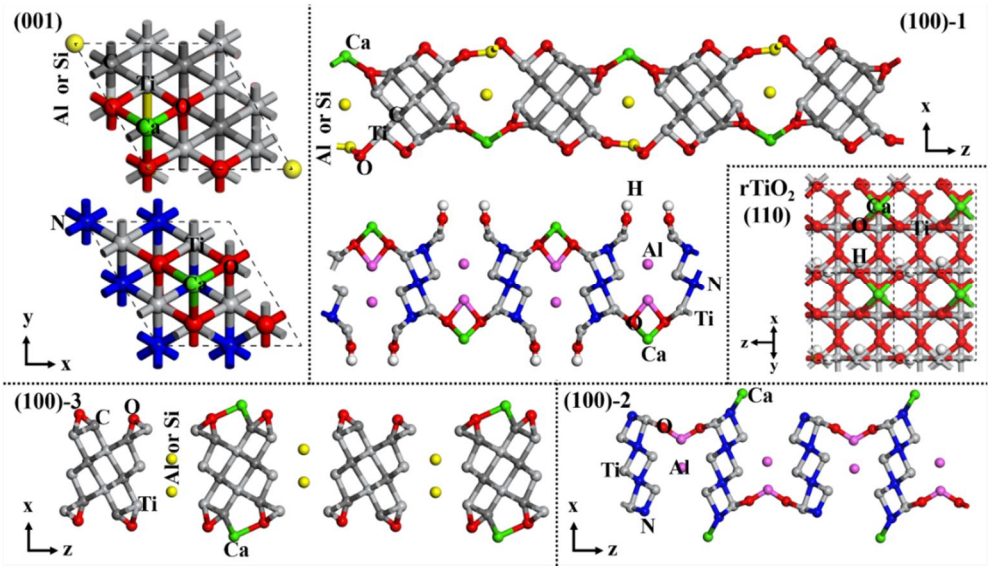


**Fig. 2.18.** Optimized configurations for the $Ca^{2+}$ ion bound on the (001), (100)-1, (100)-2, and (100)-3 surfaces of the $Ti_3AlC_2$, $Ti_3SiC_2$, and $Ti_2AlN$ and the (110) surface of $rTiO_2$.

## 2.5 Mechanism for Biocompatibility of the MAX Phases.

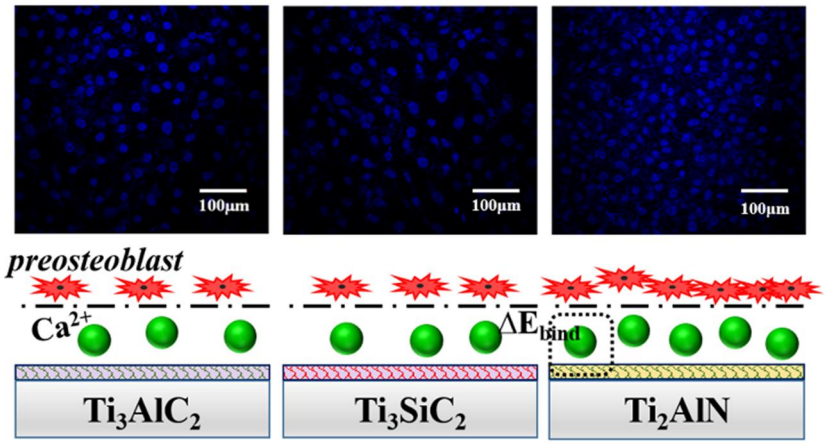


**Fig. 2.19.** Schematic diagram of mechanism on the biocompatibility of $Ti_3AlC_2$, $Ti_3SiC_2$, and $Ti_2AlN$ based on the absorbed $Ca^{2+}$ ions.

The cell affinity is known to be affected by the surface hydrophilicity, chemical composition, net charge, topography, and other biochemical-physical properties. [108, 109] Herein, we observed that not only the hydrophilicity but also the intrinsic features of the chemical elements played important roles in the biological behavior of these selected MAX phases (**Fig. 2.19**). Because the real compositions of $Ti_3AlC_2$, $Ti_3SiC_2$ and $Ti_2AlN$ surface are composed of $Al_2O_3$ and $TiC_xO_y$, $SiO_2$ and $TiC_xO_y$, and $Al_2O_3$ and $TiN_xO_y$, respectively [114, 119, 121] (**Fig. 2.3-2.5** and **Table 2.1**), and the surface of pure Ti and Ti–6Al–4V alloy are protected by $TiO_2$, and $TiO_2$ and $Al_2O_3$,

[137, 138] the different biocompatibility of these materials can be explained based on the different biological properties of these oxides, carbides and nitrides. It is unquestionable that the $TiO_2$ has the best biocompatibility among these oxides. [139-141] However, TiC layer and TiN layer were shown to enhance the biocompatibility of Ti–6Al–4V alloy [142], NiTi alloy [113, 143], and Co–Cr alloy [144]. In particular, the TiN layer even improved the biocompatibility of pure Ti [145] because the TiN layer not only physically prevented the release of toxic ions, such as vanadium and nickel ions, but also improved the cell functions, including promoting the adsorption of proteins, increasing the metabolism of energy and amino acids, and enhancing the regulation of inflammation. [113, 142, 143, 146]

To determine the source of the biocompatibility, the adsorption of $Ca^{2+}$ ions on the surface of the materials is commonly used in theoretical calculation. [114, 115] Stefano et al. demonstrated that the $TiN_xO_y$ surface could initiate spontaneous nucleation of calcium phosphate because of the presence of a higher surface negative charge ($TiO_2$, –0.45; the partially oxidized TiN, –0.80). [114] In our experiment, the binding energy between the absorbed $Ca^{2+}$ ion and the surface was first calculated using first-principles theory for direct evaluation. Compared with $Ti_3AlC_2$ and $Ti_3SiC_2$, $Ti_2AlN$ had a notable stronger binding energy for the partially

oxidized (001) and (100) surfaces. The above analyses were consistent with our *in vitro* tests, in which $Ti_2AlN$ exhibited preferable proliferation and osteogenic differentiation compared with $Ti_3AlC_2$ and $Ti_3SiC_2$; the performance was even superior to that of the commercial Ti–6Al–4V alloy and comparable to that of pure Ti.

This discovery is interesting, as previous studies on the MAX phase for biomedical applications have merely focused on $Ti_3SiC_2$, [71, 72] which is considered to have the best resistance to oxidation and corrosion among the traditional MAX phases. [147, 148] However, this study revealed that the inertness was not the dominant factor determining the biocompatibility of the MAX phase. The $Ti_2AlN$ exhibited outstanding biocompatibility because of the $TiN_xO_y$ surface. The above analyses illustrated that the chemical composition of the MX layer in MAX phase played a more critical role than the A site atom. This mechanism also provided a direction to select a MAX phase for biomedical applications, which is valuable for such a large family. Based on this work, we speculate that the $Ti_{n+1}AN_n$ group (such as $Ti_4AlN_3$) has excellent biocompatibility. It is also notable that the two-dimensional early transition metal carbides or nitrides (MXenes), mainly consisting of these (001) surfaces, [79, 81, 91] probably exhibit remarkable biocompatibility due to the strongest

binding energy of the $Ca^{2+}$ ions on the (001) surface compared with the other surfaces.

## 2.6 Conclusion

This study used self-made pure MAX phase slices as platforms to evaluate the biocompatibility of $Ti_3AlC_2$, $Ti_3SiC_2$, and $Ti_2AlN$ via *in vitro* tests. All the phases were determined to be biocompatible with respect to the commercial Ti–6Al–4V alloy and pure Ti with preosteoblasts and fibroblasts. The cell proliferation and differentiation examination under an osteoblastic environment revealed that $Ti_2AlN$ exhibited the optimal performance among these MAX phases; its performance was even superior to that of the commercial Ti–6Al–4V alloy and comparable to that of pure Ti. The mechanism for this behavior was interpreted for the different protective layers. First-principles calculations revealed that $Ca^{2+}$ ions had a strong affinity for adsorption on the $TiN_xO_y$ layer, which indicated the good biocompatibility of $Ti_2AlN$. Our discovery provides a new route for the selection of specific MAX phases and MXenes for biomedical applications.

# Chapter 3.

# Strong and Biocompatible Poly (lactic acid) Membrane Enhanced by $Ti_3C_2T_z$ (MXenes) Nanosheets for Guided Bone Regeneration

## 3.1 Introduction

Guided bone regeneration (GBR) is a reliable and validated therapy which is widely used in oral rehabilitation with the placement of dental implants and periodontal regeneration. [24-26] The basic principle of GBR technique is protecting the bone healing from the interference of non-osteogenic tissue using a GBR membrane [25-27]. Compared with non-resorbable titanium and polytetrafluoroethylene membranes, the resorbable membranes, such as poly (lactic acid) (PLA), poly (glycolic acid) (PGA), poly (ε-caprolactone) (PCL) and their copolymers or tissue-derived collagens, are fascinating because of the exemption from the secondary surgery for membrane removal. [26, 29] However, the amount of regenerated bone is insufficient in the case of resorbable membrane, which results from the poor mechanical properties [29] and cellular responses. [26, 29]

Currently, graphene and its derivates have been proved to enhance the mechanical properties of polymeric matrices, [34, 35, 43] and promote the interfacial bio-interaction, and mediate cellular signalling and biological performance with cocultured cells. [53-55] MXene ($M_{n+1}X_nT_z$) is an emerging family of 2-dimensional

early transition metal carbides or nitrides, derived by the selective exfoliation of "A" layers from MAX phases (where M is an early transition metal, A is an A-group element, X is C and/or N, and $T_z$ stands for terminated functional groups, such as -OH, -O, and -F). [56, 62, 79-81] These nanosheets possess large specific surface area, excellent electrical conductivity, and good hydrophilicity, which grant them desirable candidates for versatile applications such as in energy storage, [91, 93, 149, 150] surface absorbent, [94, 96] and sensor device [97, 98]. Very recently, the biomedical applications of MXenes including biosensing, [98, 100] anti-bacteria activity, [101, 102] photothermal ablation [103] and cellular imaging [105] arouse great interests.

The chapter 1 shows that MAX phases, the precursors of MXenes, possess good biocompatibility (**Fig. 2.16**). On the basis of the first-principles calculation from the binding energy of $Ca^{2+}$ ion with the partially oxidized surficial layer, the (001) surfaces of each MAX phase, which the MXenes mainly consist of have much stronger cell affinity than the (100) surfaces (**Table 2.3**).

In this chapter, the intrinsic biocompatibility of MXene ($Ti_3C_2T_z$ nanosheets, d-$Ti_3C_2T_z$) is discussed using graphene oxide (GO) as reference. Then, the commercial PLA is used as matrix of GBR membrane to explore the enhancement by $Ti_3C_2T_z$ nanosheets (d-$Ti_3C_2T_z$) in respects of mechanical properties and

biocompatibility. To the best of our knowledge, this is the first effort to embed the MXenes into the biomedical polymer materials. The $Ti_3C_2T_z$ nanosheets, whose interface with hydrophobic PLA matrix is mediated using n-octyltriethoxysilane (OTES), endows the nanocomposite membranes with high mechanical properties and promotion of osteoblastic adhesion, proliferation, and differentiation.

## 3.2 Preparation and Characterization of d-$Ti_3C_2T_z$ and GO

### 3.2.1 Preparation and Characterization of d-$Ti_3C_2T_z$

#### 3.2.1.1 Methods

The $Ti_3C_2T_z$ nanosheets (d-$Ti_3C_2T_z$) were prepared based on the previous references with chemical acid etching and physical sonication. [84, 91] In a typical procedure, **(1)** 2 g of $Ti_3AlC_2$ powders (400 mesh, Beijing Jinhezhi Materials Co., Ltd., China) were carefully added into the 20 mL of hydrochloric acid (7.5 M) with 1.98 g of lithium fluoride (LiF, Alfa Aesar, 98.5%). The time of above procedure should be over 10 min to avoid the initial overheating of the solution as the result of exothermic reactions. **(2)** The mixture was stirred using a magnetic Teflon stir bar for 24 h at 35 °C. **(3)** The as-produced powders (exfoliated $Ti_3C_2T_z$, e-$Ti_3C_2T_z$) were

rinsed by hydrochloric acid (5 M) for 5 cycles to remove the excess LiF. **(4)** The deionized water was then used to remove the remaining hydrochloric acid until the pH of the supernatant reached approximately 6. The centrifuge (3500 rpm, 15 min; Hanil MF 550, Korea) was employed during above washing steps. **(5)** In order to prepare the d-$Ti_3C_2T_z$ nanosheets, the e-$Ti_3C_2T_z$ powders were dispersed in deionized water with a weight ratio of e-$Ti_3C_2T_z$: water of 1:100 in vacuum chamber (200 Pa for 30 min). The suspension was then sonicated in an ultrasonic bath (40 % power; Daihan DH300H, Korea) under bubbling Ar flow for 1 h. **(6)** After centrifuged at 3500 rpm for 1 h, the supernatant, which contained the d-$Ti_3C_2T_z$ was collected.

The $Ti_3AlC_2$, e-$Ti_3C_2T_z$, and d-$Ti_3C_2T_z$ were characterized by the X-ray diffractometer (XRD, AXS D8 Advance, Bruker, Germany) with Cu $K_\alpha$ radiation and their spectra were collected at a step scans of 0.02° 2θ and a step time of 0.2 sec. The morphology of e-$Ti_3C_2T_z$ was observed using field emission scanning electron microscope (Fe-SEM, ZEISS Merlin Compact, Germany). The morphology and structure of d-$Ti_3C_2T_z$ were characterized using transmission electron microscopy (TEM, Tecnai F20, FEI, USA) equipped with electron diffraction (ED) patterns, and atomic force microscope (AFM, Nano Xpert-II, EM4SYS, Korea).

### 3.2.1.2 Discussion

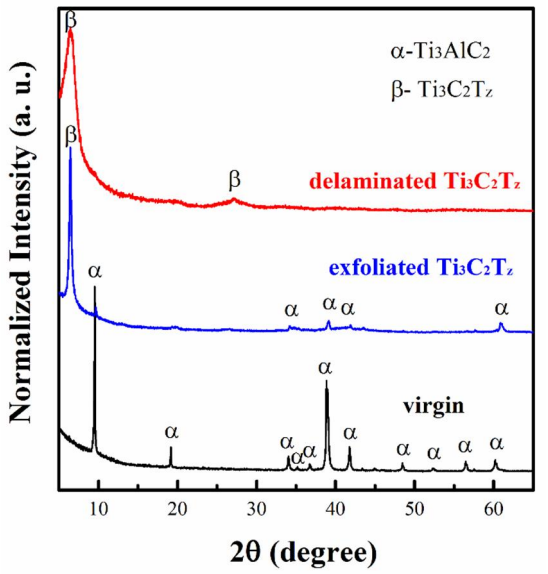


**Fig. 3.1.** XRD analysis of $Ti_3AlC_2$, e-$Ti_3C_2T_z$ and d-$Ti_3C_2T_z$ flakes.

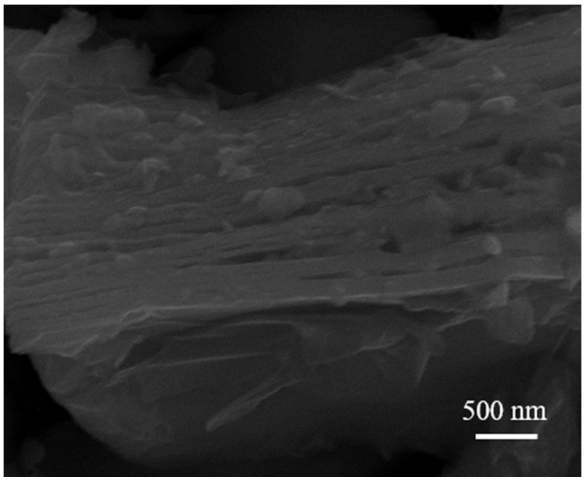


**Fig. 3.2.** SEM image of the e-$Ti_3C_2T_z$.

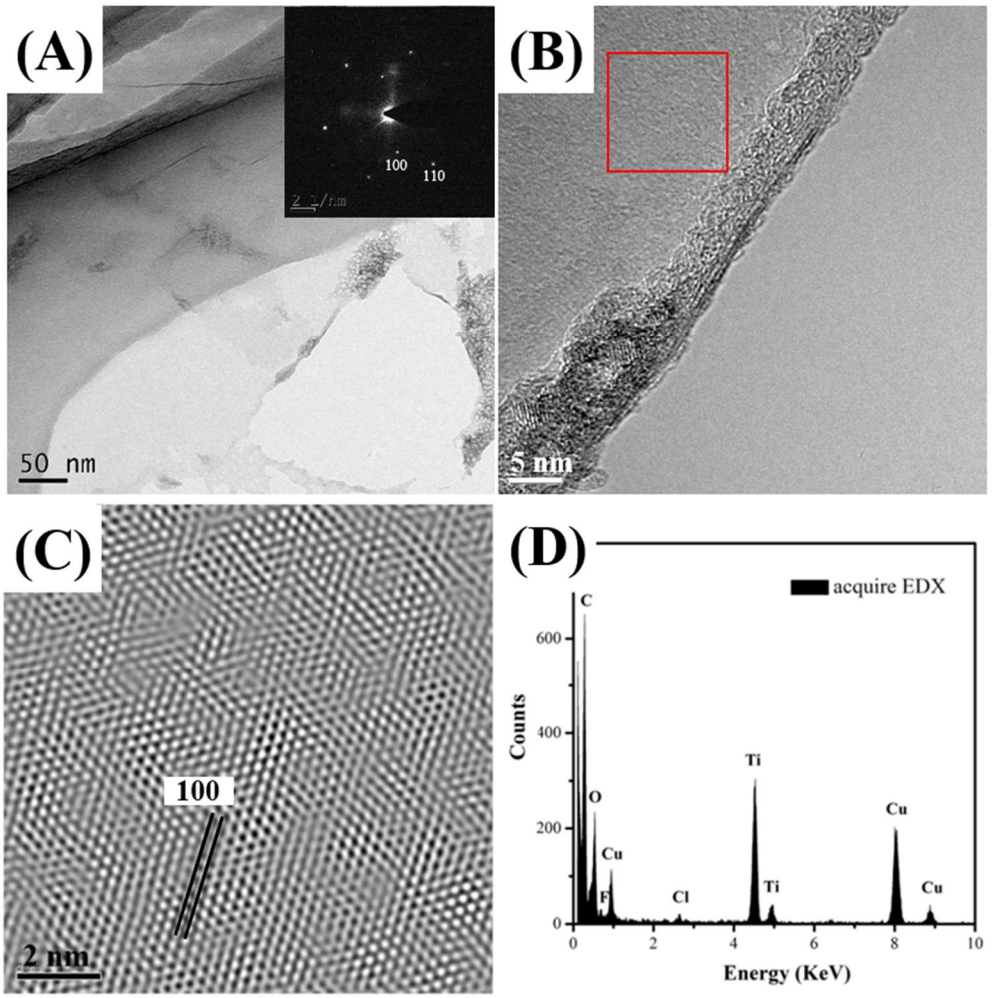


**Fig. 3.3.** TEM analysis of the d-$Ti_3C_2T_z$ flakes: **(A)** Overall morphology, inset, Nano beam electron diffraction (NBED); **(B)** High resolution transmission electron microscopy **(**HRTEM) image and curled edged, which exhibits the flake is very thin; **(C)** Inverse fast Fourier transform (IFFT) image; **(D)** Analysis results of energy dispersive spectrometer (EDS).

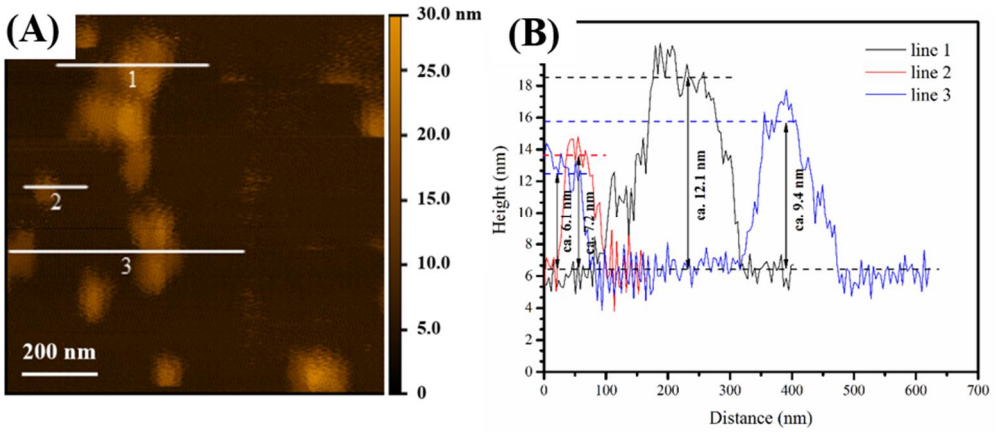


**Fig. 3.4.** **(A)** AFM image of the d-$Ti_3C_2T_z$ flakes; **(C)** Thickness of the d-$Ti_3C_2T_z$ flakes determined by AFM.

The preparation process of d-$Ti_3C_2T_z$ nanosheets was detected using XRD, SEM, TEM and AFM. The XRD patterns in the **Fig. 3.1** showed that most of the $Ti_3AlC_2$ powders transformed to e-$Ti_3C_2T_z$ after being etched in the LiF-HCl mixture for 24 h. There was no LiF or LiCl except a little $Ti_3AlC_2$ observed in the XRD patterns, after the as-synthesized powders were washed by 5 M HCl aqueous solution and deionized water. However, these $Ti_3AlC_2$ particles could be easily removed during the delamination of e-$Ti_3C_2T_z$, since the d-$Ti_3C_2T_z$ nanosheets were collected in the supernatant (3500 rpm for 1 h). In the XRD pattern of d-$Ti_3C_2T_z$, only the peaks diffracted from the $Ti_3C_2T_z$ were detected. The SEM image of e-$Ti_3C_2T_z$ exhibited accordion-like structure, which was the typical morphology

observed in the previous reference (**Fig. 3.2**). [79]

In order to further analyze the structure of d-$Ti_3C_2T_z$ nanosheets, the TEM equipped with ED was employed (**Fig. 3.3**). The size of d-$Ti_3C_2T_z$ was around several hundred nanometers. The curled edges indicated that these nanosheets were very thin. The electron diffraction pattern from the nano electron beam showed typical hexagonal structure, whose space distance of (100) plane (***$d_{100}$***) was 0.264 nm. This space distance could also be calculated from the Inverse Fast Fourier Transform (IFFT) image, which was 0.267 nm. These values were similar to the previous reference (0.266 nm). [81] The result of energy dispersive spectrometer (EDS) showed the signal of Ti, C, O, F, Cl, and Cu. The element of O, F, and Cl could be thought from the functional groups on the d-$Ti_3C_2T_z$. While, the Cu came from the supporting mesh. The AFM was used to assist the analysis of d-$Ti_3C_2T_z$ (**Fig. 3.4**). The size of the d-$Ti_3C_2T_z$ could be more clearly observed (100 – 200 nm). In addition, the thickness of the d-$Ti_3C_2T_z$ nanosheet was about 6.1 – 7.2 nm, which consisted of 6 – 7 single layers of d-$Ti_3C_2T_z$. All the above analyses demonstrated that the d-$Ti_3C_2T_z$ was successfully fabricated using the exfoliation of chemical etching and delamination of physical sonication.

### 3.2.2 Preparation and Characterization of GO

The GO nanosheets were prepared using modified Hummer's method according to the previous references. [151, 152] In brief, **(1)** 3 g of natural graphite powders and 2 g of $NaNO_3$ were mixed in a beaker (1 L) with an ice bath (< 4 °C), **(2)** followed by slow addition of 138 mL $H_2SO_4$ (98 %) with stirring over the course of 20 min. **(3)** Then 18 g of $KMnO_4$ was carefully added into the above mixture. The ice bath was removed after another 15 min of stirring, and the mixture was continuously stirred for 12 h at room temperature. **(4)** Subsequently, the mixture was gradually diluted with 600 mL of warm deionized water (60 °C). **(5)** After stirred for 30 min, 20 mL of $H_2O_2$ (37 %) was then added into the diluted solution and stirred for another 2 h to prevent the further oxidation of the GO. **(6)** The as-produced mixture was rinsed sequentially using HCl (5 %) and deionized water with centrifugation for 7 cylces, respectively. **(7)** The precipitate was re-dispersed in 600 mL of deionized water and sonicated with cell crusher for 4 h. **(8)** After the suspension was centrifuged at 11000 rpm for 15 min (Techcomp CT14D, China), the GO nanosheets were obtained from the supernatant along with freeze drying.

The GO nanosheets were characterized using transmission electron microscopy (TEM, Tecnai F20, FEI, USA) equipped with electron diffraction (ED) patterns, and atomic force microscope (AFM, Nano Xpert-II, EM4SYS, Korea).

From the TEM image, the size of GO nanosheets was about several hundred nanometers (**Fig. 3.5A**). The electron diffraction pattern shown in **Fig. 3.5B** consisted of two rings, which resulted from the stack of several GO nanosheets. The inner ring belonged to (100) and outer ring belonged to (110). [153] The AFM image showed that the size of GO nanosheets was around 100 nm, and the thickness was about 1.5 – 2.2 nm, which consisted of 2 – 3 single layers of GO (**Fig. 3.6**).

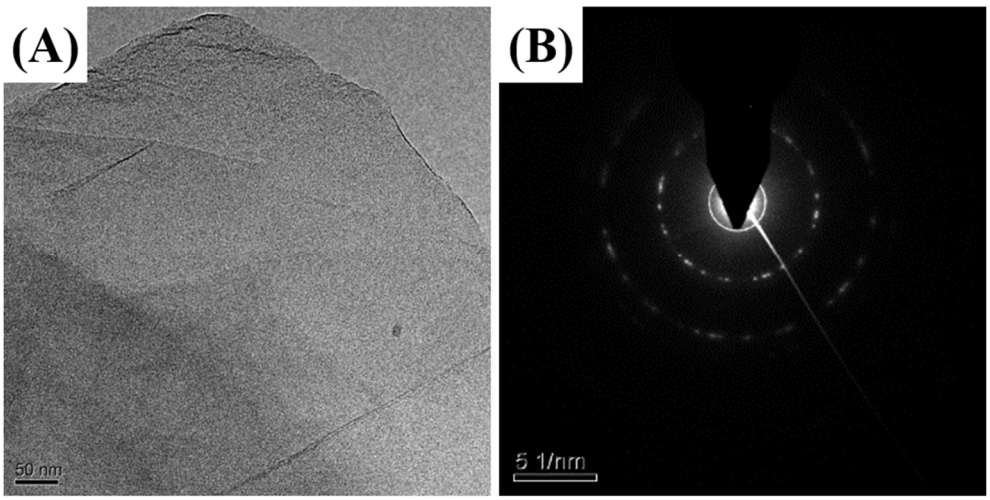


**Fig. 3.5.** **(A)** TEM overall morphology of the graphene oxide flakes; **(B)** Image of the selected area electron diffraction (SAED).

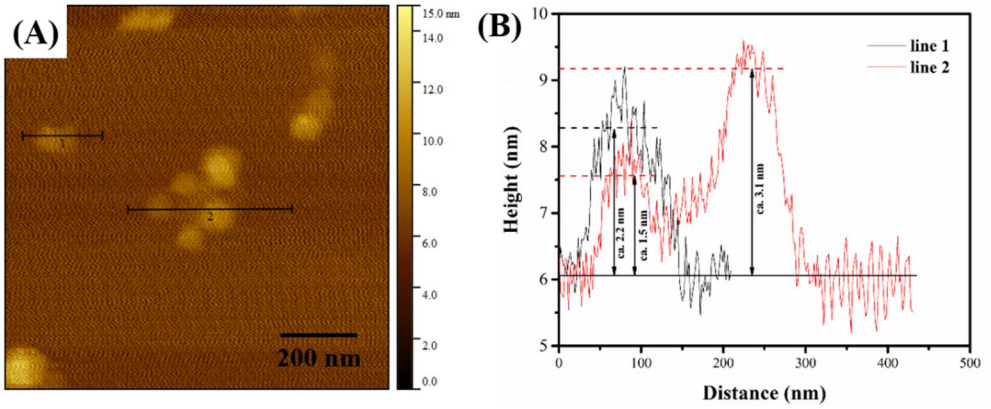


**Fig. 3.6.** **(A)** AFM image of the GO flakes; **(C)** Thickness of the GO flakes determined by AFM.

## 3.3 Comparison on Biocompatibility of d-$Ti_3C_2T_z$ and GO

Although in the chapter 2, the theoretical calculation of binding energy of $Ca^{2+}$ ions absorbed on partially oxidized (001) surface of $Ti_3AlC_2$ has been discussed to speculate the good biocompatibility of d-$Ti_3C_2T_z$, the real intrinsic biocompatibility of d-$Ti_3C_2T_z$ is still unclearly. Herein, a mouse preosteoblast cell line is employed to evaluate the intrinsic biocompatibility of d-$Ti_3C_2T_z$ using GO as a reference, since the GO has the similar structure with d-$Ti_3C_2T_z$, which is also granted by the hydrophilic functional group such as -O and -OH. In addition, the GO has been widely proved to accelerate the cell adhesion and proliferation, and induce the osteogenic differentiation. [53-55] The Teflon filters coated with d-$Ti_3C_2T_z$ and GO are used as platform due to the convenience for *in vitro* tests.

### 3.3.1 Preparation of Teflon Filters Coated with d-$Ti_3C_2T_z$ and GO

The d-$Ti_3C_2T_z$ and GO nanosheets were separately deposited on the Teflon filters (0.22 μm, Haining Yibo, China) using vacuum filtration from their as-produced suspension. After dried overnight, the filters were trimmed to 1 cm × 1 cm slices (for cell adhesion and proliferation) and sectors with 4 $cm^2$ of area (for

cell differentiation). Before the *in vitro* tests, the specimens were disinfected by PBS for 5 cycles and UV for 30 min.

The optical images of Teflon filters coated with d-$Ti_3C_2T_z$ and GO nanosheets were showed in **Fig. 3.7** and **Fig. 3.8**. From the XRD spectra, there was no impurity except the peaks belonging to the Teflon filter (**Fig. 3.9**).

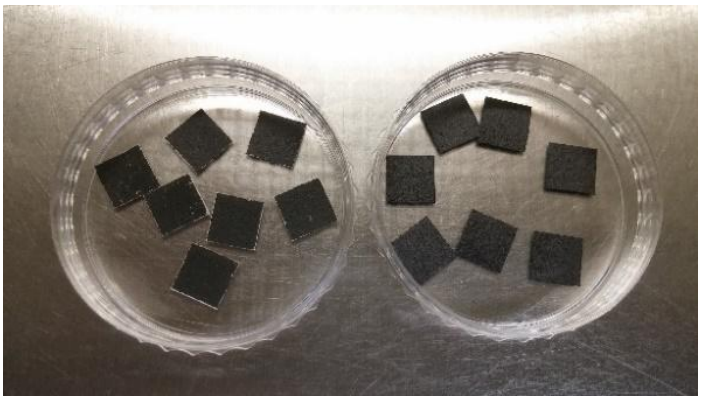

**Fig. 3.7.** The optical images of Teflon filter coated with d-$Ti_3C_2T_z$ (left) and GO nanosheets (right) for cell adhesion and proliferation.

**Fig. 3.8.** The optical images of Teflon filters coated with d-$Ti_3C_2T_z$ (left) and GO nanosheets (right) for cell differentiation.

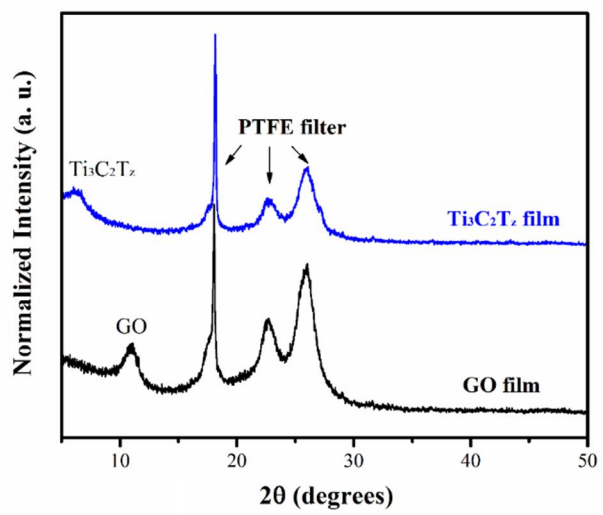


**Fig. 3.9.** X-ray diffraction spectra of Teflon filters coated with d-$Ti_3C_2T_z$ and GO.

### 3.3.2 Biological Behaviors of Preosteoblasts on the Teflon Filters Coated with d-$Ti_3C_2T_z$ and GO Nanosheets

#### 3.3.2.1 Methods

A mouse preosteoblast cell line (MC3T3-E1; ATCC CRL-2593, USA) was employed via *in vitro* tests. The cells were cultivated in alpha-minimum essential medium (α-MEM, Welgene, Korea) with 10% fetal bovine serum (FBS; Cellgro, USA) and 1% penicillin streptomycin (Pen Strep; Life Technologies, USA) in a humidified incubator (Sanyo, Japan) with 5% $CO_2$ at 37°C. A dye-exclusion assay (Trypan blue) was used to count the cells.

The morphology and distribution of the preosteoblasts ($5\times10^4$ cells/mL) after being cultured for 4 h were recorded using the confocal laser scanning microscopy (CLSM; Olympus FluoView FV1000, Japan). Phalloidin (Life Technology, USA) and 4', 6-diamidino-2-phenylindole (DAPI, Life Technology, USA) were used to stain the filamentous actin and nucleus, respectively. The SEM was also used to detect the spreading of preosteoblasts on the PLA membranes, where the adherent cells were fixed with 2.5% glutaraldehyde and dehydrated in graded ethanol.

The cell proliferation after 5-day and 7-day incubation ($1\times10^4$ cells/mL), was analyzed based on the amount of DNA using a Cyquant cell proliferation assay kit (C7026, Invitrogen, USA). The DNA level of the detached cells was evaluated using a multiple plate reader (Victor3, Perkin Elmer, Germany) at 480/520 nm wavelength. The measured florescence values were converted to the DNA content using a DNA standard curve.

The cell differentiation was determined by the alkaline phosphatase (ALP) assay. After incubation for 12 days, the total protein of the cells was determined using the Bio-Rad protein assay kit (Bio-Rad, USA) based on a series of bovine serum albumin (BSA; Sigma) standards. Then, the ALP activity was predicted based on the color change from p-nitrophenyl phosphate (pNPP, Sigma) to p-nitrophenol (pNP). The amount of ALP was calculated based on the absorbance value at 405 nm (OD value) per milligram of total cellular protein.

The hydrophilicity of the Teflon filter coated with d-$Ti_3C_2T_z$ and GO slices was evaluated based on the contact angle with approximately 10 μL of deionized water using a goniometer (Phoenix 300, Korea) at ambient atmosphere.

All the results were expressed as the mean ± standard deviation. The difference between the two groups was determined with a one-way analysis of variance

(ANOVA) using *Statistical Product and Service Solutions* software, and $p < 0.05$ was considered to be statistically significant.

### 3.3.2.2 Discussion

As a prerequisite, the deduction of the intrinsic biocompatibility of $Ti_3C_2T_z$ was first confirmed on account of the contrast with GO using mouse preosteoblast cell line (MC3T3-E1) (**Fig. 3.10**). The typical CLSM images showed that preosteoblasts spread much better on the $Ti_3C_2T_z$-coated surface than on the GO-coated surface (**Fig. 3.10**A). This phenomenon was corroborated by the results of contact angle with deionized water since the hydrophilic materials induced a higher level of the adhesion and spreading of the MC3T3-E1 cells. [110] The more hydrophilic d-$Ti_3C_2T_z$ (32.1°) exhibited better initial cell attachment compared with the GO (58.6°, **Fig. 3.10B**). Moreover, the d-$Ti_3C_2T_z$ exhibited preferable cell proliferation and differentiation performance than GO, which were attested by DNA assay and alkaline phosphatase (ALP) assay, respectively (**Fig. 3.10C-D)**. These results could be explained by the better biocompatibility of Ti-based materials compared with the C-based materials. For instance, Ti could be used to enhance the biocompatibility of polymers [154] and diamond-like carbon (DLC) coatings. [155]

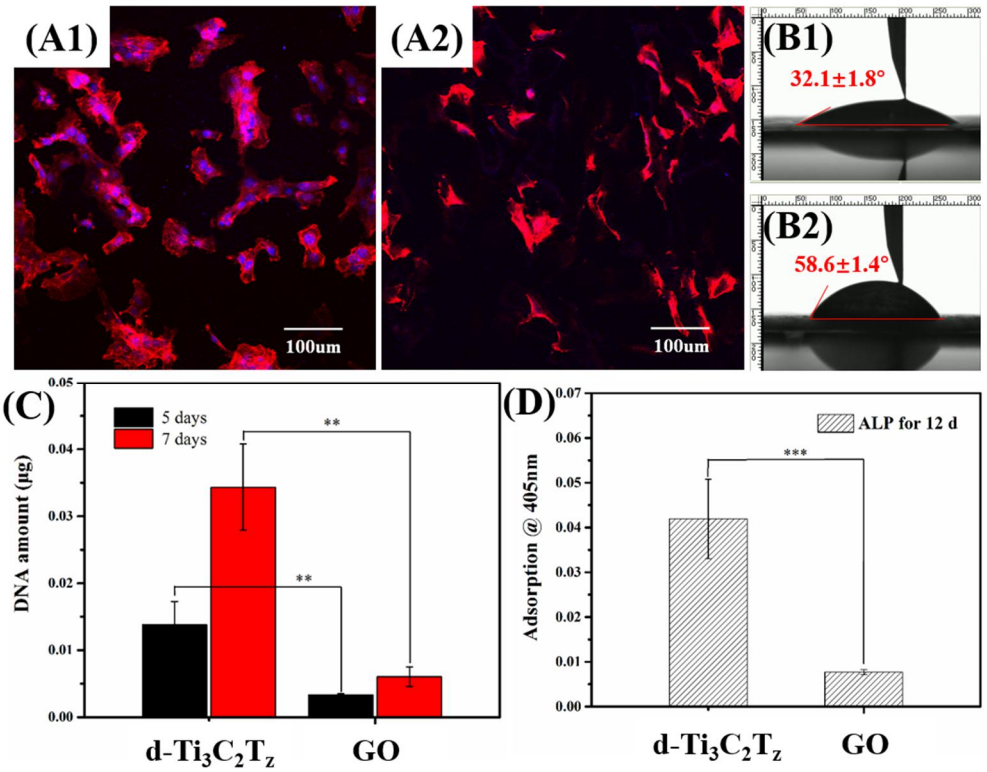


**Fig. 3.10.** The intrinsic biocompatibility of d-$Ti_3C_2T_z$ **(1)** and GO **(2)**: **(A)** Typical CLSM images of adherent MC3T3-E1 cells after incubation for 4 h. Seeding cell density was $5\times10^4$ cells/mL; **(B)** The hydrophilicity determined by the contact angle with the deionized water; **(C)** The cell proliferation after 5-day and 7-day incubation determined by DNA assay. Seeding cell density was $1\times10^4$ cells/mL. (**P<0.01); **(D)** The cell differentiation after 12-day incubation determined by ALP activity. Seeding cell density was $1\times10^4$ cells/mL. (***P<0.001)

## 3.4 Preparation of d-$Ti_3C_2T_z$ Enhanced PLA Nanocomposite Membrane

### 3.4.1 Surface Modification of d-$Ti_3C_2T_z$

The interaction between the filler and matrix is the critical issue for the composite materials. [156] In this work, a biocompatible silane OTES [157] was used to mediate the hydrophilic d-$Ti_3C_2T_z$ and hydrophobic PLA (**Fig. 3.11**). In brief, **(1)** the d-$Ti_3C_2T_z$ nanosheets were separated from the aqueous suspension using ultrahigh-speed centrifuge (Hanil Micro 17TR, Korea) at 15000 rpm for 30 min. **(2)** After dried overnight, 80 mg of d-$Ti_3C_2T_z$ nanosheets were re-dispersed in the 40 mL of ethanol (containing 1 vol. % water) using sonication and magnetic stirring. **(3)** Then 1 vol. % OTES was added into the mixture and continuously stirred for 1 day. **(4)** After reaction, the excess OTES was rinsed using ultrahigh-speed centrifuge with ethanol for 5 cycles and **(5)** the OTES grafted d-$Ti_3C_2T_z$ nanosheets (OTES-d-$Ti_3C_2T_z$) were obtained after dried overnight.

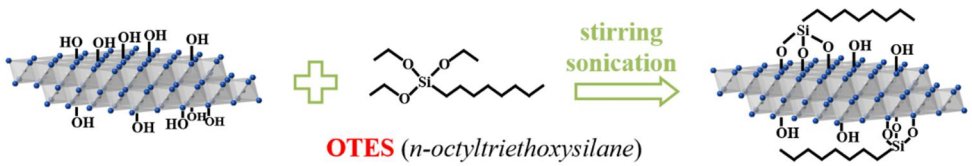


**Fig. 3.11.** Schematic diagram of surface modification of OTES on the d-$Ti_3C_2T_z$.

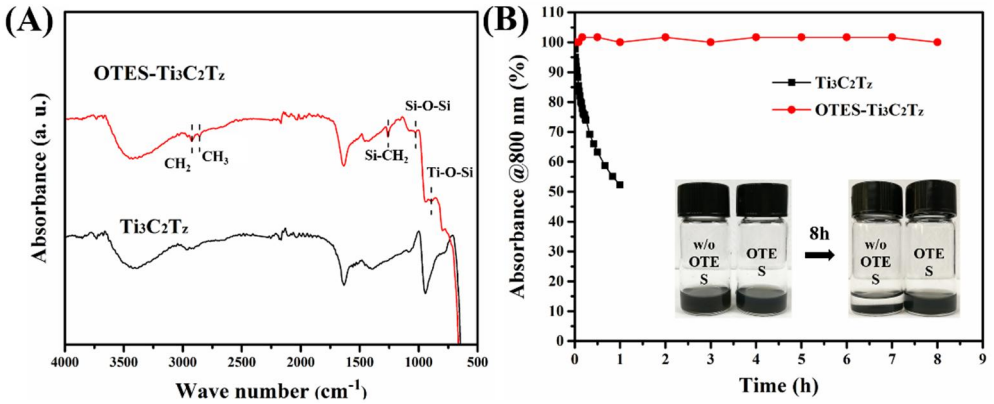


**Fig. 3.12.** **(A)** FT-IR spectra of d-$Ti_3C_2T_z$ (black) and OTES grafted d-$Ti_3C_2T_z$ (red). **(B)** The dispersity and stability of d-$Ti_3C_2T_z$ (black) and OTES grafted d-$Ti_3C_2T_z$ (red) in the DCM determined by the relative absorbance of UV-visible spetrophotometer at 800 nm. Inset: digital images.

The Fourier transform infrared (FT-IR) spectra confirmed that the OTES was successfully grafted on d-$Ti_3C_2T_z$ (**Fig. 3.12A**). The identical stretching vibrations emerged in the both of spectra, including -OH at 3420 $cm^{-1}$, C=O at 1640 $cm^{-1}$, and O-H at 1400 $cm^{-1}$, which belonged to $Ti_3C_2T_z$. [104, 158] Meanwhile, the new peaks appeared in the OTES-treated $Ti_3C_2T_z$. [159, 160] The peak of 2920 $cm^{-1}$ and 2860 $cm^{-1}$ belonged to the asymmetric and symmetric vibrations of C-H in the $CH_2$ and $CH_3$. The peak of 1260 $cm^{-1}$ was generated from the vibration of C-H in the Si-$CH_2$. The peaks of 1030 $cm^{-1}$ and 900 $cm^{-1}$ belonged to the Si-O-Si and Ti-O-Si, respectively.

[159, 160] Furthermore, the dispersity and stability of the d-$Ti_3C_2T_z$ in the dichloromethane (DCM) was evaluated using the UV-visible spectrophotometer (at 800 nm, shown in **Fig. 3.12B**). The relative absorbance of the virgin d-$Ti_3C_2T_z$/DCM suspension decreased to 50 % after holding for about 1 h. In contrast, the relative absorbance in the case of OTES-d-$Ti_3C_2T_z$/DCM suspension maintained around 100 % for up to 8 h. The digital images also clearly showed that the virgin d-$Ti_3C_2T_z$/DCM suspension became transparent after holding for 8 h, while the OTES-d-$Ti_3C_2T_z$/DCM suspension was still turbid (inset in **Fig. 3.12B**). All the above results demonstrated that the OTES grafted d-$Ti_3C_2T_z$ had a good dispersity and stability in the hydrophobic DCM solvent.

### 3.4.2 Preparation of PLA Nanocomposite Membrane Using Solvent Casting

The OTES-d-$Ti_3C_2T_z$ enhanced PLA composite membranes were prepared using solvent casting. In brief, the certain amount of OTES-d-$Ti_3C_2T_z$ was dispersed in the dichloromethane (DCM) with sonication and magnetic stirring. Then the PLA beads (Pureco, Korea; $M_n$: 70,000; $M_w$: 140,000) were added into the mixture and stirred for 2 days. The ratio of DCM to PLA beads is 10 mL to 1 g. And the variable

ratio of OTES-d-$Ti_3C_2T_z$ to PLA was 0, 0.2 wt. %, 0.5 wt. %, 0.7 wt. %, 1 wt.% and 2 wt. %. Subsequently, the mixture suspension was poured into the polyethylene (PE) mold. After dried in the hood overnight (room temperature), the as-produced membranes were dried in the vacuum for another 1 day to clear all the remaining DCM. The pure PLA membrane was also prepared with the same method, which was used as reference for the following property tests.

The **Fig. 3.13** showed the OTES-d-$Ti_3C_2T_z$ enhanced PLA nanocomposite membranes. They were uniform, and the transparency had a negative correlation with the loading content of OTES-d-$Ti_3C_2T_z$. The morphology of cross section was characterized using field emission scanning electron microscope (**Fig. 3.14**). The nanocomposite membranes with low loading content of OTES-d-$Ti_3C_2T_z$ exhibited uniform morphology (up to 0.5 wt. %). However, these flakes aggregated together when the filler content increased (above 0.5 wt. %).

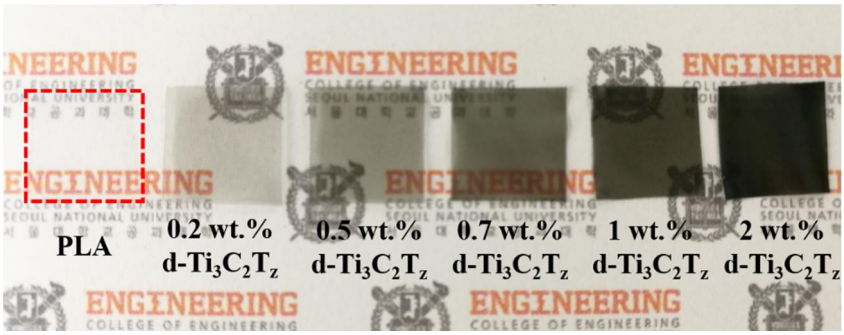


**Fig. 3.13.** Optical images of PLA and OTES-d-$Ti_3C_2T_z$/PLA composite membranes prepared using simple solvent casting.

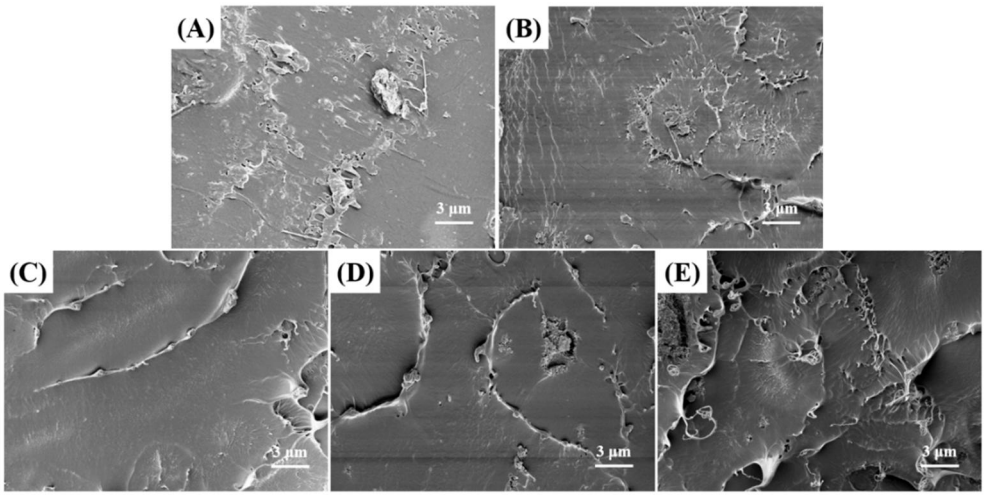


**Fig. 3.14.** Typical SEM cross section morphology of pure PLA and OTES-d-$Ti_3C_2T_z$/PLA nanocomposite membranes with different loading content: **(A)** Pure PLA, **(B)** 0.2 wt. %, **(C)** 0.5 wt. %, **(D)** 1 wt. %, **(E)** 2 wt. %.

## 3.5 Mechanical Properties of PLA Nanocomposite Membrane

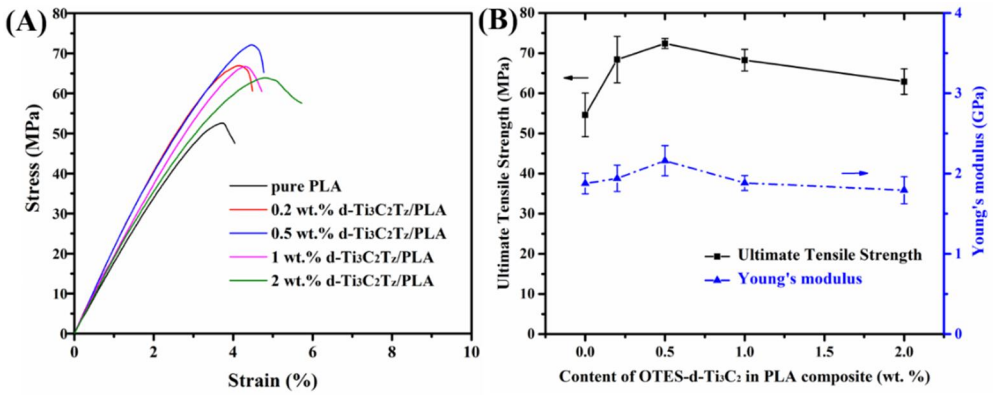


**Fig. 3.15.** the typical stress-strain curves **(A)** and ultimate tensile strength and Young's modulus **(B)** of pure PLA and OTES-d-$Ti_3C_2T_z$/PLA nanocomposite membranes.

The mechanical properties were evaluated using a tensile test machine equipped with a 1000-N capacity load cell (Instron model 3342, USA) (**Fig. 3.15**). The ultimate tensile strength (UTS) rose along with the increasing loading content of OTES-d-$Ti_3C_2T_z$, and descended after reaching at 0.5 wt. %. The optimized UTS was obtained as 72 MPa. The same trend was also observed in the case of Young's modulus, whose optimized value was 2.2 GPa. These results conformed to the analysis of the amount and distribution of OTES-d-$Ti_3C_2T_z$ in the nanocomposite membranes (**Fig. 3.14**). The mechanical properties of nanocomposite membranes

were reinforced by the homogenously distributed secondary phases, whereas it deteriorated when the filler content saturated due to the aggregation of loaded flakes. This phenomenon was also widespread in the graphene-enhanced nanocomposite materials. [156] In addition, we noticed that the optimized UTS in this research was quite high compared with the previous works (**Fig. 3.16**), where the graphene or its derivative was used as the enhanced secondary phase for PLA. Since these works adopted different preparation methods, the direct comparison of absolute UTS could not reflect the merit of our work accurately. Hence, the enhancement of optimized UTS was calculated on basis of the pure PLA membrane which was fabricated using the same method. The enhancement in this work was about 33%. It was almost the highest in contrast with the graphene-enhanced works where the solvent casting was adopted. The reason could be ascribed to the strong interaction between OTES-d-$Ti_3C_2T_z$ and PLA, which ensured the efficient load transferring between these two components.

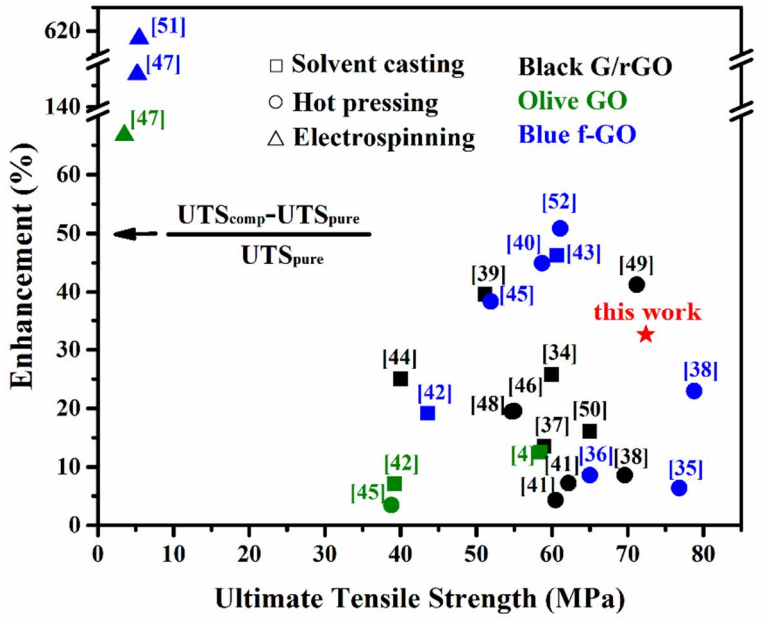


**Fig. 3.16.** Comparison of UTS and its enhancement of OTES-d-$Ti_3C_2T_z$/PLA nanocomposite membrane in this work with those of the membranes which were enhanced by graphene (or reduced GO), GO, and functional group modified GO from the references. [34-52]

### 3.6 Biocompatibility of PLA Nanocomposite Membrane

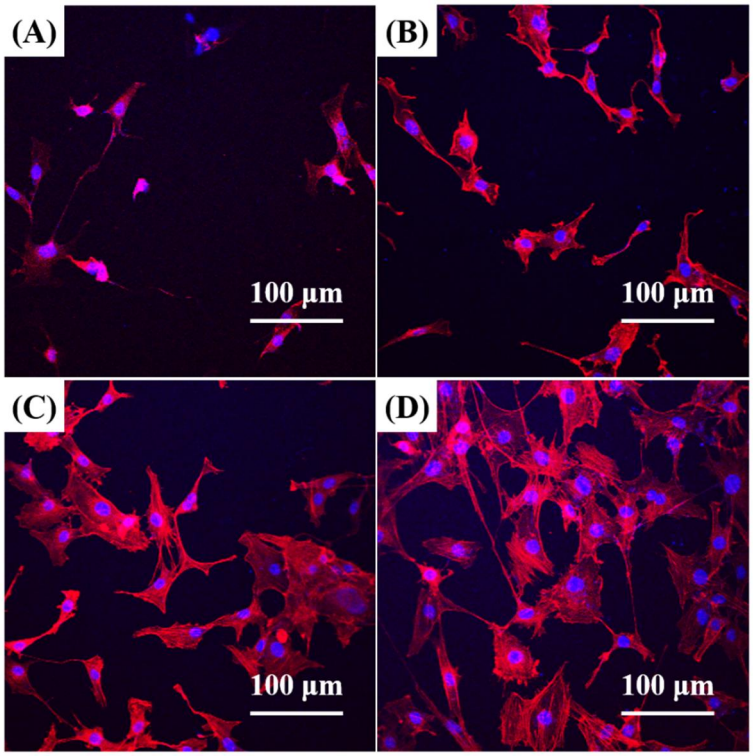


**Fig. 3.17.** Typical CLSM images of adherent MC3T3-E1 cells on pure PLA and OTES-d-$Ti_3C_2T_z$/PLA nanocomposite membranes: **(A)** Pure PLA, **(B)** 0.2 wt. %, **(C)** 0.5 wt. %, **(D)** 1 wt. %.

The detailed procedure of *in vitro* tests in this section was the same as **Section 3.2.2.1**. In brief, the MC3T3-E1 cells were employed to evaluate the biocompatibility of PLA membranes after enhanced by OTES-d-$Ti_3C_2T_z$. After

24-hour incubation (Seeding cell density, $5\times10^4$ cells/mL), the CLSM images exhibited that more preosteoblasts attached on the OTES-d-$Ti_3C_2T_z$/PLA nanocomposite membranes (**Fig. 3.17**). Likewise, the cell spreading area of preosteoblasts had an intimate connection with the loading content of d-$Ti_3C_2T_z$ in the nanocomposite membranes (**Fig. 3.17**). In addition, the SEM was also used to detect the spreading of preosteoblasts on the PLA membranes, where the adherent cells were fixed with 2.5% glutaraldehyde and dehydrated in graded ethanol. The results were shown in **Fig. 3.18**. The typical SEM images exhibited that the d-$Ti_3C_2T_z$ promoted the spreading of preosteoblasts on the nanocomposite membranes.

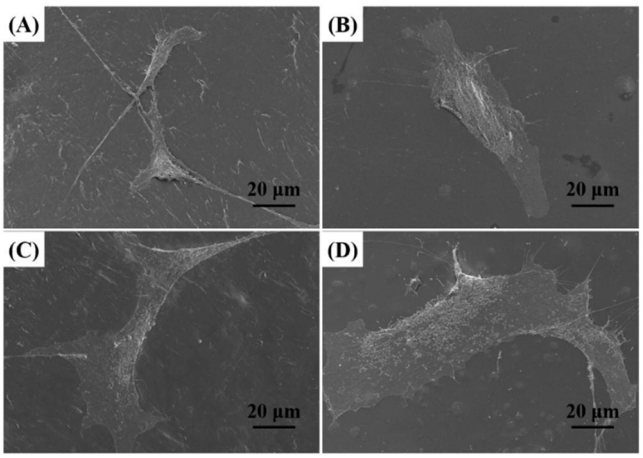

**Fig. 3.18**. Typical SEM images of adherent MC3T3-E1 cells on pure PLA and OTES-d-$Ti_3C_2T_z$/PLA nanocomposite membranes: **(A)** Pure PLA, **(B)** 0.2 wt. %, **(C)** 0.5 wt. %, **(D)** 1 wt. %.

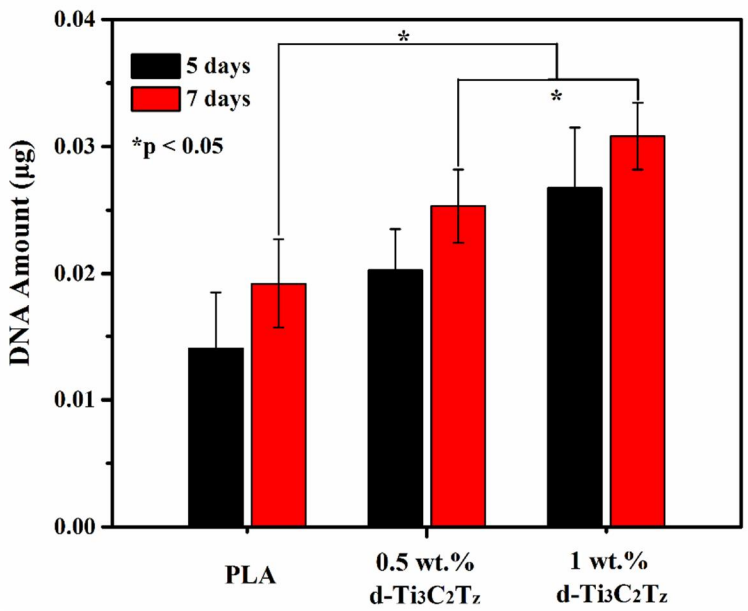


**Fig. 3.19.** DNA assay for determining the cell viability of preosteoblasts on the pure PLA and OTES-d-$Ti_3C_2T_z$ enhanced PLA composite membranes after 5-day and 7-day incubation. Seeding cell density was $1\times10^4$ cells/mL.

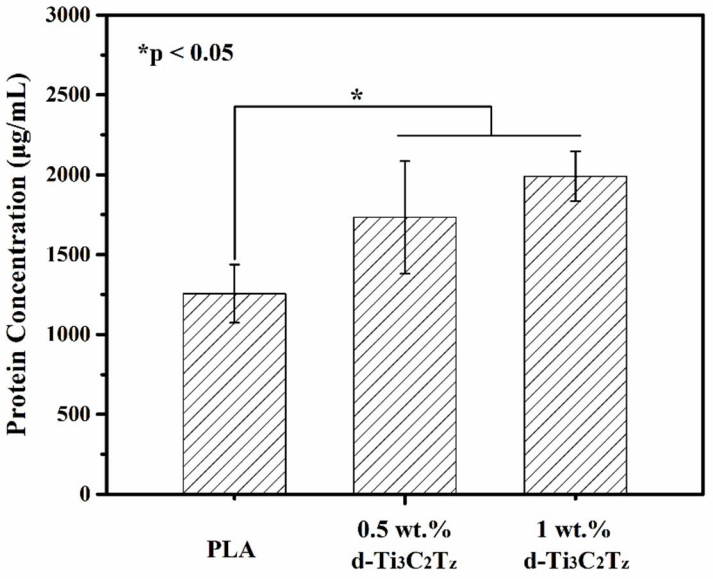


**Fig. 3.20.** The amount of protein obtained from the preosteoblasts after incubating on the pure PLA and OTES-d-$Ti_3C_2T_z$ enhanced PLA composite membranes for 12 days. Seeding cell density was $0.5\times10^4$ cells/mL.

The d-$Ti_3C_2T_z$ was also authenticated to improve the proliferation of preosteoblasts. The cell viability determined by DNA assay showed that preosteoblasts much more actively proliferated on the OTES-d-$Ti_3C_2T_z$/PLA nanocomposite membranes after 7-day incubation (**Fig. 3.19**). Similarly, the larger amount of protein was obtained after the preosteoblasts being incubated on the OTES-d-$Ti_3C_2T_z$/PLA nanocomposite membranes for 12 days (**Fig. 3.20**). Then the analysis of ALP activity indicated that the d-$Ti_3C_2T_z$ could also promote osteogenic

differentiation of nanocomposite membrane (**Fig. 3.21**). The above phenomena could be ascribed to the good intrinsic biocompatibility of $Ti_3C_2T_z$ nanosheets, which was speculated based on the first-principles calculation in the **Chapter 2**. Herein, *in vitro* tests also exhibited that the Teflon filter coated with $Ti_3C_2T_z$ nanosheets had much better biological behaviors with preosteoblasts than that coated with graphene oxide (GO) including cell adhesion, proliferation, and differentiation (**Fig. 3.10**). Hence, $Ti_3C_2T_z$ nanosheets are believed to possess good intrinsic biocompatibility since GO has been widely confirmed to significantly promote interfacial bio-interactions by experiments and simulations.[53-55] Besides, it was noteworthy that although the aggregation of d-$Ti_3C_2T_z$ impaired the mechanical properties of nanocomposite membranes rapidly (**Fig. 3.15**), the aggregated d-$Ti_3C_2T_z$ did not have a serious negative effect on biocompatibility. On the contrary, it still supported the physiological activities of preosteoblasts in our research, where the loading content range of d-$Ti_3C_2T_z$ in the nanocomposite membranes was 0 - 1wt. % (**Fig. 3.17-3.21**)

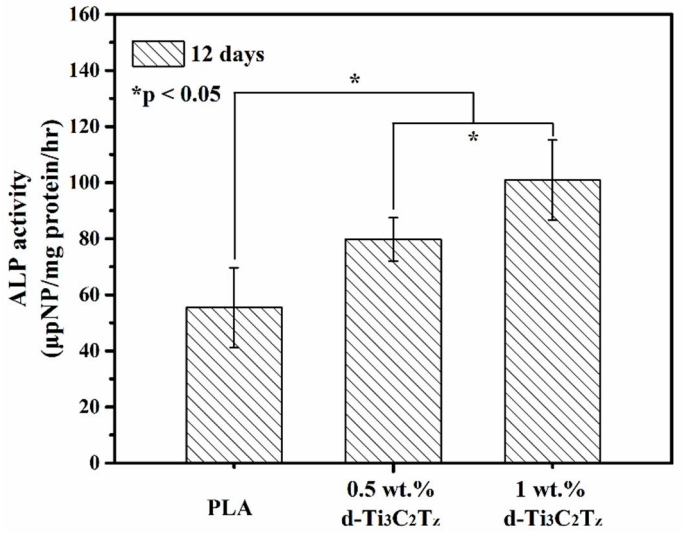


**Fig. 3.21.** ALP assay for determining the cell differentiation of preosteoblasts on the pure PLA and OTES-d-$Ti_3C_2T_z$ enhanced PLA composite membranes after 12-day incubation. Seeding cell density was $0.5\times10^4$ cells/mL.

## 3.7 Conclusion

In summary, this chapter demonstrated the biocompatibility of $Ti_3C_2T_z$ nanosheets (d-$Ti_3C_2T_z$) in the osteoblastic condition using GO as reference. A robust strategy was developed to prepare the strong and biocompatible d-$Ti_3C_2T_z$ enhanced PLA nanocomposite membranes. The OTES was successfully used to mediate the interface between hydrophilic d-$Ti_3C_2T_z$ and hydrophobic PLA matrix. The optimized UTS was 72 MPa, which was obtained when the loading content of d-$Ti_3C_2T_z$ was 0.5 wt. %. The enhancement was about 33% compared with pure PLA membrane. In addition, the d-$Ti_3C_2T_z$ was certified to accelerate the cell adhesion and proliferation of preosteoblasts, and promote the osteogenic differentiation on the PLA membrane. Hence, these strong and biocompatible nanocomposite membranes have an intriguing future to be applied as guide bone regeneration membrane.

# Chapter. 4 Conclusion and Perspective

This thesis systematically evaluated the biocompatibility of selected MAX phases ($Ti_3AlC_2$, $Ti_3SiC_2$, and $Ti_2AlN$) in respect of different A-site and X-site atoms via *in vitro* tests. A general mechanism for the biocompatibility of MAX phases was proposed using the first-principles calculations. Then the good biocompatibility of theoretical-predicted d-$Ti_3C_2T_z$ was ascertained via *in vitro* tests and these nanosheets were used to enhance the mechanical properties and biocompatibility of PLA membrane. The conclusions were list as follows:

**(1)** The $Ti_3AlC_2$, $Ti_3SiC_2$, and $Ti_2AlN$ were determined to be biocompatible with respect to preosteoblasts and fibroblasts in contrast with the commercial Ti–6Al–4V alloy and pure Ti. **(2)** The cell proliferation and differentiation examination under an osteoblastic environment revealed that $Ti_2AlN$ exhibited the optimal performance among these MAX phases. **(3)** The mechanism for this behavior resulted from the strong affinity of $Ca^{2+}$ ions onto the $TiN_xO_y$ layer, which indicated the good biocompatibility of $Ti_2AlN$. **(4)** Compared with GO, preosteoblasts had a better performance of cell adhesion, proliferation, and osteogenic differentiation on the d-$Ti_3C_2T_z$ nanosheets. **(5)** The OTES successfully mediated the interface

between hydrophilic d-$Ti_3C_2T_z$ and hydrophobic PLA matrix. The optimized UTS of OTES-d-$Ti_3C_2T_z$/PLA nanocomposite membranes was 72 MPa (at 0.5 wt. %), which increased by 33% compared with pure PLA membrane. **(6)** The d-$Ti_3C_2T_z$ was also authenticated to accelerate the cell adhesion and proliferation of preosteoblasts, and promote the osteogenic differentiation on the nanocomposite membranes.

This work provided a new route for the selection of specific MAX phases for biomedical applications, such as dental and orthopedic fields. Likewise, the MXene had an intriguing future to simultaneously enhance the mechanical properties and biocompatibility of biopolymer, such as the polymer matrix for GBR membrane. Whereas, in consideration of the time and experimental condition, the following problems left and should be investigated in the future:

**(1)** The intensive and comprehensive mechanism on the biocompatibility of MAX phases should be explored, such as the details of cellular recognition of cell–matrix interactions through biomolecules. **(2)** The influence of the functional groups on the biocompatibility of MXenes should be explored thoroughly. **(3)** The *in vivo* tests should be introduced to evaluate the biocompatibility of MAX phases and the OTES-d-$Ti_3C_2T_z$/PLA nanocomposite membranes. **(4)** A mass production method

should be developed to prepare the d-$Ti_3C_2T_z$, and the cost should be controlled in the acceptable range for the commercial application.

## References


1. Werner Groll, and Björn Delin, "Open-mindedness is the way forward," *Dentsply Implants Magazine*, **1**, 17-18 (**2013**).

2. L. Le Guehennec, A. Soueidan, P. Layrolle, and Y. Amouriq. "Surface treatments of titanium dental implants for rapid osseointegration," *Dental Materials*, **23**, 844-854 (**2007**).

3. W. Becker, P. Hujoel, B. E. Becker, and P. Wohrle. "Dental implants in an aged population: evaluation of periodontal health, bone loss, implant survival, and quality of life," *Clinical Implant Dentistry and Related Research*, **18**, 473-479 (**2016**).

4. T. Jemt, and J. Johansson. "Implant Treatment in the Edentulous Maxillae: A 15-Year Follow-Up Study on 76 Consecutive Patients Provided with Fixed Prostheses," *Clinical Implant Dentistry and Related Research*, **8**, 61-69 (**2006**).

5. Y. Kirmanidou, M. Sidira, M. E. Drosou, V. Bennani, A. Bakopoulou, A. Tsouknidas, N. Michailidis, and K. Michalakis. "New Ti-Alloys and Surface Modifications to Improve the Mechanical Properties and the Biological Response to Orthopedic and Dental Implants: A Review," *Biomed Research International*, (**2016**).

6. X. L. Shi, L. L. Xu, M. L. Munar, and K. Ishikawa. "Hydrothermal treatment for TiN as abrasion resistant dental implant coating and its fibroblast response," *Materials Science & Engineering C-Materials for Biological Applications*, **49**, 1-6

(**2015**).

7. T. Hanawa. "Metal ion release from metal implants," *Materials Science & Engineering C-Biomimetic and Supramolecular Systems*, **24**, 745-752 (**2004**).

8. S. Bauer, P. Schmuki, K. von der Mark, and J. Park. "Engineering biocompatible implant surfaces: Part I: Materials and surfaces," *Progress in Materials Science*, **58**, 261-326 (**2013**).

9. D. J. Wever, A. G. Veldhuizen, M. M. Sanders, J. M. Schakenraad, and J. R. vanHorn. "Cytotoxic, allergic and genotoxic activity of a nickel-titanium alloy," *Biomaterials*, **18**, 1115-1120 (**1997**).

10. S. Minagar, C. C. Berndt, J. Wang, E. Ivanova, and C. Wen. "A review of the application of anodization for the fabrication of nanotubes on metal implant surfaces," *Acta Biomaterialia*, **8**, 2875-2888 (**2012**).

11. C. N. Elias, D. C. Figueira, and P. R. Rios. "Influence of the coating material on the loosing of dental implant abutment screw joints," *Materials Science & Engineering C-Biomimetic and Supramolecular Systems*, **26**, 1361-1366 (**2006**).

12. E. D. de Avila, B. P. Lima, T. Sekiya, Y. Torii, T. Ogawa, W. Y. Shi, and R. Lux. "Effect of UV-photofunctionalization on oral bacterial attachment and biofilm formation to titanium implant material," *Biomaterials*, **67**, 84-92 (**2015**).

13. M. Annunziata, A. Oliva, M. A. Basile, M. Giordano, N. Mazzola, A. Rizzo, A. Lanza, and L. Guida. "The effects of titanium nitride-coating on the topographic and biological features of TPS implant surfaces," *Journal of Dentistry*, **39**, 720-728 (**2011**).

14. B. Subramanian, C. V. Muraleedharan, R. Ananthakumar, and M. Jayachandran.

"A comparative study of titanium nitride (TiN), titanium oxy nitride (TiON) and titanium aluminum nitride (TiAlN), as surface coatings for bio implants," *Surface & Coatings Technology*, **205**, 5014-5020 (**2011**).

15. Y. H. Jeong, C. H. Lee, C. H. Chung, M. K. Son, and H. C. Choe. "Effects of TiN and WC coating on the fatigue characteristics of dental implant," *Surface & Coatings Technology*, **243**, 71-81 (**2014**).

16. H. Guleryuz, and H. Cimenoglu. "Effect of thermal oxidation on corrosion and corrosion-wear behaviour of a Ti-6A1-4V alloy," *Biomaterials*, **25**, 3325-3333 (**2004**).

17. A. K. Srivastava. "Anti-diabetic and toxic effects of vanadium compounds," *Molecular and Cellular Biochemistry*, **206**, 177-182 (**2000**).

18. J. L. Domingo, M. Gomez, J. M. Llobet, J. Corbella, and C. L. Keen. "Oral Vanadium Administration to Streptozotocin-Diabetic Rats Has Marked Negative Side-Effects Which Are Independent of the Form of Vanadium Used," *Toxicology*, **66**, 279-287 (**1991**).

19. C. Morant, M. F. Lopez, A. Gutierrez, and J. A. Jimenez. "AFM and SEM characterization of non-toxic vanadium-free Ti alloys used as biomaterials," *Applied Surface Science*, **220**, 79-87 (**2003**).

20. Y. Okazaki, S. Rao, Y. Ito, and T. Tateishi. "Corrosion resistance, mechanical properties, corrosion fatigue strength and cytocompatibility of new Ti alloys without Al and V," *Biomaterials*, **19**, 1197-1215 (**1998**).

21. H. Kim, C. Y. Kim, D. W. Kim, I. S. Lee, G. H. Lee, J. C. Park, S. J. Lee, and K. Y. Lee. "Wear performance of self-mating contact pairs of TiN and TiAlN coatings

on orthopedic grade Ti-6Al-4V," *Biomedical Materials*, **5**, 044108 (**2010**).

22. P. Y. Yi, L. F. Peng, and J. Q. Huang. "Multilayered TiAlN films on Ti6Al4V alloy for biomedical applications by closed field unbalanced magnetron sputter ion plating process," *Materials Science & Engineering C-Materials for Biological Applications*, **59**, 669-676 (**2016**).

23. M. S. El-Eskandarany. "Structure and properties of nanocrystalline TiC full-density bulk alloy consolidated from mechanically reacted powders," *Journal of Alloys and Compounds*, **305**, 225-238 (**2000**).

24. D. Buser, U. Bragger, N. P. Lang, and S. Nyman. "Regeneration and enlargement of jaw bone using guided tissue regeneration," *Clinical Oral Implants Research*, **1**, 22-32 (**1990**).

25. M. Retzepi, and N. Donos. "Guided Bone Regeneration: biological principle and therapeutic applications," *Clinical Oral Implants Research*, **21**, 567-576 (**2010**).

26. M. C. Bottino, V. Thomas, G. Schmidt, Y. K. Vohra, T. M. G. Chu, M. J. Kowolik, and G. M. Janowski. "Recent advances in the development of GTR/GBR membranes for periodontal regeneration-A materials perspective," *Dental Materials*, **28**, 703-721 (**2012**).

27. A. Turri, I. Elgali, F. Vazirisani, A. Johansson, L. Emanuelsson, C. Dahlin, P. Thomsen, and O. Omar. "Guided bone regeneration is promoted by the molecular events in the membrane compartment," *Biomaterials*, **84**, 167-183 (**2016**).

28. J. L. Wang, L. N. Wang, Z. Y. Zhou, H. J. Lai, P. Xu, L. Liao, and J. C. Wei. "Biodegradable Polymer Membranes Applied in Guided Bone/Tissue Regeneration: A Review," *Polymers*, **8**, (**2016**).

29. D. Schneider, F. E. Weber, U. Grunder, C. Andreoni, R. Burkhardt, and R. E. Jung. "A randomized controlled clinical multicenter trial comparing the clinical and histological performance of a new, modified polylactide-co-glycolide acid membrane to an expanded polytetrafluorethylene membrane in guided bone regeneration procedures," *Clinical Oral Implants Research*, **25**, 150-158 (**2014**).

30. M. Simion, U. Misitano, L. Gionso, and A. Salvato. "Treatment of dehiscences and fenestrations around dental implants using resorbable and nonresorbable membranes associated with bone autografts: A comparative clinical study," *International Journal of Oral & Maxillofacial Implants*, **12**, 159-167 (**1997**).

31. Z. S. Haidar. "Bio-Inspired/-Functional Colloidal Core-Shell Polymeric-Based NanoSystems: Technology Promise in Tissue Engineering, Bioimaging and NanoMedicine," *Polymers*, **2**, 323-352 (**2010**).

32. N. Donos, L. Kostopoulos, and T. Karring. "Alveolar ridge augmentation using a resorbable copolymer membrane and autogenous bone grafts - An experimental study in the rat," *Clinical Oral Implants Research*, **13**, 203-213 (**2002**).

33. F. Stavropoulos, C. Dahlin, J. D. Ruskin, and C. Johansson. "A comparative study of barrier membranes as graft protectors in the treatment of localized bone defects - An experimental study in a canine model," *Clinical Oral Implants Research*, **15**, 435-442 (**2004**).

34. Y. W. Cao, J. C. Feng, and P. Y. Wu. "Preparation of organically dispersible graphene nanosheet powders through a lyophilization method and their poly(lactic acid) composites," *Carbon*, **48**, 3834-3839 (**2010**).

35. B. K. Ahn, J. Sung, Y. H. Li, N. Kim, M. Ikenberry, K. Hohn, N. Mohanty, P.

Nguyen, T. S. Sreeprasad, S. Kraft, V. Berry, and X. S. Sun. "Synthesis and Characterization of Amphiphilic Reduced Graphene Oxide with Epoxidized Methyl Oleate," *Advanced Materials*, **24**, 2123-2129 (**2012**).

36. L. Lei, J. H. Qiu, and E. Sakai. "Preparing conductive poly(lactic acid) (PLA) with poly(methyl methacrylate) (PMMA) functionalized graphene (PFG) by admicellar polymerization," *Chemical Engineering Journal*, **209**, 20-27 (**2012**).

37. A. M. Pinto, J. Cabral, D. A. P. Tanaka, A. M. Mendes, and F. D. Magalhaes. "Effect of incorporation of graphene oxide and graphene nanoplatelets on mechanical and gas permeability properties of poly(lactic acid) films," *Polymer International*, **62**, 33-40 (**2013**).

38. X. Z. Tong, F. Song, M. Q. Li, X. L. Wang, I. J. Chin, and Y. Z. Wang. "Fabrication of graphene/polylactide nanocomposites with improved properties," *Composites Science and Technology*, **88**, 33-38 (**2013**).

39. X. Y. Li, Y. H. Xiao, A. Bergeret, M. Longerey, and J. F. Che. "Preparation of Polylactide/Graphene Composites From Liquid-Phase Exfoliated Graphite Sheets," *Polymer Composites*, **35**, 396-403 (**2014**).

40. X. Lu, J. T. Huang, L. Yang, N. Zhang, G. Jin, and J. P. Qu. "In-situ thermal reduction and effective reinforcement of graphene nanosheet/poly (ethylene glycol)/poly (lactic acid) nanocomposites," *Polymers for Advanced Technologies*, **25**, 1515-1522 (**2014**).

41. B. W. Chieng, N. A. Ibrahim, W. M. Z. W. Yunus, M. Z. Hussein, Y. Y. Then, and Y. Y. Loo. "Effects of Graphene Nanoplatelets and Reduced Graphene Oxide on Poly(lactic acid) and Plasticized Poly(lactic acid): A Comparative Study," *Polymers*,

**6**, 2232-2246 (**2014**).

42. G. Z. Papageorgiou, Z. Terzopoulou, D. Bikiaris, K. S. Triantafyllidis, E. Diamanti, D. Gournis, P. Klonos, E. Giannoulidis, and P. Pissis. "Evaluation of the formed interface in biodegradable poly(L-lactic acid)/graphene oxide nanocomposites and the effect of nanofillers on mechanical and thermal properties," *Thermochimica Acta*, **597**, 48-57 (**2014**).

43. L. Zhang, Y. F. Li, H. H. Wang, Y. D. Qiao, J. Z. Chen, and S. K. Cao. "Strong and ductile poly(lactic acid) nanocomposite films reinforced with alkylated graphene nanosheets," *Chemical Engineering Journal*, **264**, 538-546 (**2015**).

44. R. B. Valapa, G. Pugazhenthi, and V. Katiyar. "Effect of graphene content on the properties of poly(lactic acid) nanocomposites," *RSC Advances*, **5**, 28410-28423 (**2015**).

45. W. Chartarrayawadee, R. Molloy, A. Ratchawet, N. Janmee, M. Butsamran, and K. Panpai. "Fabrication of poly (lactic acid)/graphene oxide/stearic acid composites with improved tensile strength," *Polymer Composites*, (**2015**).

46. C. Gonçalves, A. Pinto, A. V. Machado, J. Moreira, I. C. Gonçalves, and F. Magalhães. "Biocompatible reinforcement of poly (lactic acid) with graphene nanoplatelets," *Polymer Composites*, (**2016**).

47. C. M. Zhang, L. W. Wang, T. L. Zhai, X. C. Wang, Y. Dan, and L. S. Turng. "The surface grafting of graphene oxide with poly (ethylene glycol) as a reinforcement for poly(lactic acid) nanocomposite scaffolds for potential tissue engineering applications," *Journal of the Mechanical Behavior of Biomedical Materials*, **53**, 403-413 (**2016**).

48. A. M. Pinto, C. Goncalves, I. C. Goncalves, and F. D. Magalhaes. "Effect of biodegradation on thermo-mechanical properties and biocompatibility of poly(lactic acid)/graphene nanoplatelets composites," *European Polymer Journal*, **85**, 431-444 (**2016**).

49. Y. Q. Gao, O. T. Picot, E. Bilotti, and T. Peijs. "Influence of filler size on the properties of poly(lactic acid) (PLA)/graphene nanoplatelet (GNP) nanocomposites," *European Polymer Journal*, **86**, 117-131 (**2017**).

50. C. Hu, Z. Li, Y. Wang, J. Gao, K. Dai, G. Zheng, C. Liu, C. Shen, H. Song, and Z. Guo. "Comparative assessment of the strain-sensing behaviors of polylactic acid nanocomposites: reduced graphene oxide or carbon nanotubes," *Journal of Materials Chemistry C*, **5**, 2318-2328 (**2017**).

51. C. Liu, J. Shen, K. W. K. Yeung, and S. C. Tjong. "Development and Antibacterial Performance of Novel Polylactic Acid-Graphene Oxide-Silver Nanoparticle Hybrid Nanocomposite Mats Prepared By Electrospinning," *ACS Biomaterials Science & Engineering*, **3**, 471-486 (**2017**).

52. C. Liu, S. Ye, and J. Feng. "Promoting the dispersion of graphene and crystallization of poly (lactic acid) with a freezing-dried graphene/PEG masterbatch," *Composites Science and Technology*, **144**, 215-222 (**2017**).

53. Y. Luo, H. Shen, Y. X. Fang, Y. H. Cao, J. Huang, M. X. Zhang, J. W. Dai, X. Y. Shi, and Z. J. Zhang. "Enhanced Proliferation and Osteogenic Differentiation of Mesenchymal Stem Cells on Graphene Oxide-Incorporated Electrospun Poly(lactic-co-glycolic acid) Nanofibrous Mats," *ACS Applied Materials & Interfaces*, **7**, 6331-6339 (**2015**).

54. T. Zhang, N. Li, K. Y. Li, R. F. Gao, W. Gu, C. C. Wu, R. G. Su, L. W. Liu, Q. Zhang, and J. Liu. "Enhanced proliferation and osteogenic differentiation of human mesenchymal stem cells on biomineralized three-dimensional graphene foams," *Carbon*, **105**, 233-243 (**2016**).

55. C. Cheng, S. Li, A. Thomas, N. A. Kotov, and R. Haag. "Functional Graphene Nanomaterials Based Architectures: Biointeractions, Fabrications, and Emerging Biological Applications," *Chemical Reviews*, **117**, 1826-1914 (**2017**).

56. M. W. Barsoum. "The $M_{N+1}AX_N$ phases: a new class of solids: thermodynamically stable nanolaminates," *Progress in Solid State Chemistry*, **28**, 201-281 (**2000**).

57. H. Fashandi, M. Dahlqvist, J. Lu, J. Palisaitis, S. I. Simak, I. A. Abrikosov, J. Rosen, L. Hultman, M. Andersson, A. L. Spetz, and P. Eklund. "Synthesis of $Ti_3AuC_2$, $Ti_3Au_2C_2$ and $Ti_3IrC_2$ by noble metal substitution reaction in $Ti_3SiC_2$ for high-temperature-stable Ohmic contacts to SiC," *Nature Materials*, **16**, 814-818 (**2017**).

58. M. W. Barsoum, and M. Radovic. "Elastic and mechanical properties of the MAX phases," *Annual Review of Materials Research*, **41**, 195-227 (**2011**).

59. C. F. Hu, Y. C. Zhou, Y. W. Bao, and D. T. Wan. "Tribological properties of polycrystalline $Ti_3SiC_2$ and $Al_2O_3$-reinforced $Ti_3SiC_2$ composites," *Journal of the American Ceramic Society*, **89**, 3456-3461 (**2006**).

60. L. Wu, J. X. Chen, M. Y. Liu, Y. W. Bao, and Y. C. Zhou. "Reciprocating friction and wear behavior of $Ti_3AlC_2$ and $Ti_3AlC_2/Al_2O_3$ composites against AIS152100 bearing steel," *Wear*, **266**, 158-166 (**2009**).

61. M. W. Barsoum, and T. El-Raghy. "The MAX Phases: Unique New Carbide and Nitride Materials Ternary ceramics turn out to be surprisingly soft and machinable, yet also heat-tolerant, strong and lightweight," *Am. Scientist*, **89**, 33443 (**2001**).

62. P. Eklund, M. Beckers, U. Jansson, H. Hogberg, and L. Hultman. "The $M_{(n+1)}AX_{(n)}$ phases: Materials science and thin-film processing," *Thin Solid Films*, **518**, 1851-1878 (**2010**).

63. Z. Sun. "Progress in research and development on MAX phases: a family of layered ternary compounds," *International Materials Reviews*, **56**, 143-166 (**2011**).

64. X. H. Wang, and Y. C. Zhou. "Microstructure and properties of $Ti_3AlC_2$ prepared by the solid-liquid reaction synthesis and simultaneous in-situ hot pressing process," *Acta Materialia*, **50**, 3141-3149 (**2002**).

65. T. El-Raghy, M. W. Barsoum, A. Zavaliangos, and S. R. Kalidindi. "Processing and mechanical properties of $Ti_3SiC_2$: II, effect of grain size and deformation temperature," *Journal of the American Ceramic Society*, **82**, 2855-2860 (**1999**).

66. Z. J. Lin, M. J. Zhuo, M. S. Li, J. Y. Wang, and Y. C. Zhou. "Synthesis and microstructure of layered-ternary $Ti_2AlN$ ceramic," *Scripta Materialia*, **56**, 1115-1118 (**2007**).

67. J. Lis, L. Chlubny, M. Lopacinski, L. Stobierski, and M. A. Bucko. "Ceramic nanolaminates - Processing and application," *Journal of the European Ceramic Society*, **28**, 1009-1014 (**2008**).

68. L. L. Hench. "Bioceramics," *Journal of the American Ceramic Society*, **81**, 1705-1728 (**1998**).

69. M. A. Lopes, F. J. Monteiro, and J. D. Santos. "Glass-reinforced hydroxyapatite

composites: fracture toughness and hardness dependence on microstructural characteristics," *Biomaterials*, **20**, 2085-2090 (**1999**).

70. N. F. Gao, and Y. Miyamoto. "Joining of $Ti_3SiC_2$ with Ti-6Al-4V alloy," *Journal of Materials Research*, **17**, 52-59 (**2002**).

71. N. F. Gao, Y. Miyamoto, H. Oonishi, and D. Zhang. "Investigation on the application of $Ti_3SiC_2$ ceramics for biomaterials," *Journal of Materials Science Letters*, **21**, 783-785 (**2002**).

72. T. L. Ngai, L. Lu, J. B. Chen, J. H. Zhang, and Y. Y. Li. "Preparation of SiC reinforced $Ti_3SiC_2$-base composite and its biocompatibility evaluation," *Ceramics International*, **40**, 5343-5348 (**2014**).

73. S. L. Shi, W. Pan, M. H. Fang, and Z. Y. Fang. "Reinforcement of hydroxyapatite bioceramic by addition of $Ti_3SiC_2$," *Journal of the American Ceramic Society*, **89**, 743-745 (**2006**).

74. S. L. Shi, and W. Pan. "Machinable $Ti_3SiC_2$/Hydroxyapatite bioceramic composites by spark plasma sintering," *Journal of the American Ceramic Society*, **90**, 3331-3333 (**2007**).

75. K. S. Novoselov. "Rapid progress in producing graphene," *Nature*, **505**, 291-291 (**2014**).

76. K. S. Novoselov, A. K. Geim, S. V. Morozov, D. Jiang, Y. Zhang, S. V. Dubonos, I. V. Grigorieva, and A. A. Firsov. "Electric field effect in atomically thin carbon films," *Science*, **306**, 666-669 (**2004**).

77. J. N. Coleman, M. Lotya, A. O'Neill, S. D. Bergin, P. J. King, U. Khan, K. Young, A. Gaucher, S. De, R. J. Smith, I. V. Shvets, S. K. Arora, G. Stanton, H. Y.

Kim, K. Lee, G. T. Kim, G. S. Duesberg, T. Hallam, J. J. Boland, J. J. Wang, J. F. Donegan, J. C. Grunlan, G. Moriarty, A. Shmeliov, R. J. Nicholls, J. M. Perkins, E. M. Grieveson, K. Theuwissen, D. W. McComb, P. D. Nellist, and V. Nicolosi. "Two-Dimensional Nanosheets Produced by Liquid Exfoliation of Layered Materials," *Science*, **331**, 568-571 (**2011**).

78. L. Ci, L. Song, C. H. Jin, D. Jariwala, D. X. Wu, Y. J. Li, A. Srivastava, Z. F. Wang, K. Storr, L. Balicas, F. Liu, and P. M. Ajayan. "Atomic layers of hybridized boron nitride and graphene domains," *Nature Materials*, **9**, 430-435 (**2010**).

79. M. Naguib, M. Kurtoglu, V. Presser, J. Lu, J. J. Niu, M. Heon, L. Hultman, Y. Gogotsi, and M. W. Barsoum. "Two-Dimensional Nanocrystals Produced by Exfoliation of $Ti_3AlC_2$," *Advanced Materials*, **23**, 4248-4253 (**2011**).

80. M. Naguib, O. Mashtalir, J. Carle, V. Presser, J. Lu, L. Hultman, Y. Gogotsi, and M. W. Barsoum. "Two-dimensional transition metal carbides," *ACS Nano*, **6**, 1322-1331 (**2012**).

81. M. Naguib, V. N. Mochalin, M. W. Barsoum, and Y. Gogotsi. "25th Anniversary Article: MXenes: A New Family of Two-Dimensional Materials," *Advanced Materials*, **26**, 992-1005 (**2014**).

82. M. Ghidiu, M. Naguib, C. Shi, O. Mashtalir, L. M. Pan, B. Zhang, J. Yang, Y. Gogotsi, S. J. L. Billinge, and M. W. Barsoum. "Synthesis and characterization of two-dimensional $Nb_4C_3$ (MXene)," *Chemical Communications*, **50**, 9517-9520 (**2014**).

83. M. Naguib, J. Halim, J. Lu, K. M. Cook, L. Hultman, Y. Gogotsi, and M. W. Barsoum. "New Two-Dimensional Niobium and Vanadium Carbides as Promising

Materials for Li-Ion Batteries," *Journal of the American Chemical Society*, **135**, 15966-15969 (**2013**).

84. C. E. Ren, M. Q. Zhao, T. Makaryan, J. Halim, M. Boota, S. Kota, B. Anasori, M. W. Barsoum, and Y. Gogotsi. "Porous Two-Dimensional Transition Metal Carbide (MXene) Flakes for High-Performance Li-Ion Storage," *ChemElectroChem*, **3**, 689-693 (**2016**).

85. M. Khazaei, A. Ranjbar, M. Arai, and S. Yunoki. "Topological insulators in the ordered double transition metals $M'_2M''C_2$ MXenes (M′= Mo, W; M ″= Ti, Zr, Hf)," *Physical Review B*, **94**, 125152 (**2016**).

86. P. Urbankowski, B. Anasori, T. Makaryan, D. Er, S. Kota, P. L. Walsh, M. Zhao, V. B. Shenoy, M. W. Barsoum, and Y. Gogotsi. "Synthesis of two-dimensional titanium nitride $Ti_4N_3$ (MXene)," *Nanoscale*, **8**, 11385-11391 (**2016**).

88. J. Zhou, X. Zha, X. Zhou, F. Chen, G. Gao, S. Wang, C. Shen, T. Chen, C. Zhi, and P. Eklund. "Synthesis and electrochemical properties of two-dimensional hafnium carbide," *ACS nano*, **11**, 3841-3850 (**2017**).

87. J. Zhou, X. H. Zha, F. Y. Chen, Q. Ye, P. Eklund, S. Y. Du, and Q. Huang. "A Two-Dimensional Zirconium Carbide by Selective Etching of $Al_3C_3$ from Nanolaminated $Zr_3Al_3C_5$," *Angewandte Chemie-International Edition*, **55**, 5092-5097 (**2016**).

89. M. Q. Zhao, M. Sedran, Z. Ling, M. R. Lukatskaya, O. Mashtalir, M. Ghidiu, B. Dyatkin, D. J. Tallman, T. Djenizian, M. W. Barsoum, and Y. Gogotsi. "Synthesis of Carbon/Sulfur Nanolaminates by Electrochemical Extraction of Titanium from $Ti_2SC$," *Angewandte Chemie-International Edition*, **54**, 4810-4814 (**2015**).

90. Z. W. Seh, K. D. Fredrickson, B. Anasori, J. Kibsgaard, A. L. Strickler, M. R.

Lukatskaya, Y. Gogotsi, T. F. Jaramillo, and A. Vojvodic. "Two-dimensional molybdenum carbide (MXene) as an efficient electrocatalyst for hydrogen evolution," *ACS Energy Letters*, **1**, 589-594 (**2016**).

91. M. Ghidiu, M. R. Lukatskaya, M. Q. Zhao, Y. Gogotsi, and M. W. Barsoum. "Conductive two-dimensional titanium carbide 'clay' with high volumetric capacitance," *Nature*, **516**, 78-81 (**2014**).

92. X. Liang, A. Garsuch, and L. F. Nazar. "Sulfur Cathodes Based on Conductive MXene Nanosheets for High-Performance Lithium-Sulfur Batteries," *Angewandte Chemie International Edition*, **54**, 3907-3911 (**2015**).

93. M. R. Lukatskaya, O. Mashtalir, C. E. Ren, Y. Dall'Agnese, P. Rozier, P. L. Taberna, M. Naguib, P. Simon, M. W. Barsoum, and Y. Gogotsi. "Cation Intercalation and High Volumetric Capacitance of Two-Dimensional Titanium Carbide," *Science*, **341**, 1502-1505 (**2013**).

94. L. Wang, L. Y. Yuan, K. Chen, Y. J. Zhang, Q. H. Deng, S. Y. Du, Q. Huang, L. R. Zheng, J. Zhang, Z. F. Chai, M. W. Barsoum, X. K. Wang, and W. Q. Shi. "Loading Actinides in Multilayered Structures for Nuclear Waste Treatment: The First Case Study of Uranium Capture with Vanadium Carbide MXene," *ACS Applied Materials & Interfaces*, **8**, 16396-16403 (**2016**).

95. Y. L. Ying, Y. Liu, X. Y. Wang, Y. Y. Mao, W. Cao, P. Hu, and X. S. Peng. "Two-Dimensional Titanium Carbide for Efficiently Reductive Removal of Highly Toxic Chromium(VI) from Water," *ACS Applied Materials & Interfaces*, **7**, 1795-1803 (**2015**).

96. Q. M. Peng, J. X. Guo, Q. R. Zhang, J. Y. Xiang, B. Z. Liu, A. G. Zhou, R. P.

Liu, and Y. J. Tian. "Unique Lead Adsorption Behavior of Activated Hydroxyl Group in Two-Dimensional Titanium Carbide," *Journal of the American Chemical Society*, **136**, 4113-4116 (**2014**).

97. J. Chen, K. Chen, D. Y. Tong, Y. J. Huang, J. W. Zhang, J. M. Xue, Q. Huang, and T. Chen. "$CO_2$ and temperature dual responsive "Smart" MXene phases," *Chemical Communications*, **51**, 314-317 (**2015**).

98. F. Wang, C. H. Yang, M. Duan, Y. Tang, and J. F. Zhu. "$TiO_2$ nanoparticle modified organ-like $Ti_3C_2$ MXene nanocomposite encapsulating hemoglobin for a mediator-free biosensor with excellent performances," *Biosensors & Bioelectronics*, **74**, 1022-1028 (**2015**).

99. F. Wang, C. H. Yang, C. Y. Duan, D. Xiao, Y. Tang, and J. F. Zhu. "An Organ-Like Titanium Carbide Material (MXene) with Multilayer Structure Encapsulating Hemoglobin for a Mediator-Free Biosensor," *Journal of the Electrochemical Society*, **162**, B16-B21 (**2015**).

100. H. Liu, C. Y. Duan, C. H. Yang, W. Q. Shen, F. Wang, and Z. F. Zhu. "A novel nitrite biosensor based on the direct electrochemistry of hemoglobin immobilized on MXene-$Ti_3C_2$," *Sensors and Actuators B-Chemical*, **218**, 60-66 (**2015**).

101. K. Rasool, M. Helal, A. Ali, C. E. Ren, Y. Gogotsi, and K. A. Mahmoud. "Antibacterial Activity of $Ti_3C_2T_x$ MXene," *ACS Nano*, **10**, 3674-3684 (**2016**).

102. K. Rasool, K. A. Mahmoud, D. J. Johnson, M. Helal, G. R. Berdiyorov, and Y. Gogotsi. "Efficient Antibacterial Membrane based on Two-Dimensional $Ti_3C_2T_x$ (MXene) Nanosheets," *Scientific Reports*, **7**, (**2017**).

103. H. Lin, X. G. Wang, L. D. Yu, Y. Chen, and J. L. Shi. "Two-Dimensional

Ultrathin MXene Ceramic Nanosheets for Photothermal Conversion," *Nano Letters*, **17**, 384-391 (**2017**).

104. C. Dai, H. Lin, G. Xu, Z. Liu, R. Wu, and Y. Chen. "Biocompatible 2D Titanium Carbide (MXenes) Composite Nanosheets for pH-Responsive MRI-Guided Tumor Hyperthermia," *Chemistry of Materials*, **29**, 8637–8652 (**2017**).

105. Q. Xue, H. Zhang, M. Zhu, Z. Pei, H. Li, Z. Wang, Y. Huang, Y. Huang, Q. Deng, J. Zhou, S. Du, Q. Huang, and C. Zhi. "Photoluminescent $Ti_3C_2$ MXene Quantum Dots for Multicolor Cellular Imaging," *Advanced Materials*, **29**, 1604847 (**2017**).

106. B. Xu, M. Zhu, W. Zhang, X. Zhen, Z. Pei, Q. Xue, C. Zhi, and P. Shi. "Ultrathin MXene-Micropattern-Based Field-Effect Transistor for Probing Neural Activity," *Advanced Materials*, **28**, 3333-3339 (**2016**).

107. Enderle John D, Bronzino Joseph D, and Blanchard Susan M. "Introduction to biomedical engineering. second ed." Amsterdam; Boston: Elsevier Academic Press; 2005.

108. K. von der Mark, and J. Park. "Engineering biocompatible implant surfaces Part II: Cellular recognition of biomaterial surfaces: Lessons from cell-matrix interactions," *Progress in Materials Science*, **58**, 327-381 (**2013**).

109. S. H. Jun, E. J. Lee, S. W. Yook, H. E. Kim, H. W. Kim, and Y. H. Koh. "A bioactive coating of a silica xerogel/chitosan hybrid on titanium by a room temperature sol-gel process," *Acta Biomaterialia*, **6**, 302-307 (**2010**).

110. S. Faghihi, F. Azari, A. P. Zhilyaev, J. A. Szpunar, H. Vali, and M. Tabrizian. "Cellular and molecular interactions between MC3T3-E1 pre-osteoblasts and

nanostructured titanium produced by high-pressure torsion," *Biomaterials*, **28**, 3887-3895 (**2007**).

111. F. Iwasa, N. Hori, T. Ueno, H. Minamikawa, M. Yamada, and T. Ogawa. "Enhancement of osteoblast adhesion to UV-photofunctionalized titanium via an electrostatic mechanism," *Biomaterials*, **31**, 2717-2727 (**2010**).

112. A. Wennerberg, and T. Albrektsson. "Effects of titanium surface topography on bone integration: a systematic review," *Clinical Oral Implants Research*, **20**, 172-184 (**2009**).

113. D. Yang, X. Lü, Y. Hong, T. Xi, and D. Zhang. "The molecular mechanism for effects of TiN coating on NiTi alloy on endothelial cell function," *Biomaterials*, **35**, 6195-6205 (**2014**).

114. S. Piscanec, L. C. Ciacchi, E. Vesselli, G. Comelli, O. Sbaizero, S. Meriani, and A. De Vita. "Bioactivity of TiN-coated titanium implants," *Acta Materialia*, **52**, 1237-1245 (**2004**).

115. M. Svetina, L. C. Ciacchi, O. Sbaizero, S. Meriani, and A. De Vita. "Deposition of calcium ions on rutile (110): A first-principles investigation," *Acta Materialia*, **49**, 2169-2177 (**2001**).

116. W. L. Liu, C. J. Qiu, J. Zhou, Z. H. Ding, X. B. Zhou, S. Y. Du, Y. H. Ha, and Q. Huang. "Fabrication of $Ti_2AlN$ ceramics with orientation growth behavior by the microwave sintering method," *Journal of the European Ceramic Society*, **35**, 1385-1391 (**2015**).

117. F. C. Wang, D. M. Huo, S. K. Li, and Q. B. Fan. "Inducing $TiAl_3$ in titanium alloys by electric pulse heat treatment improves mechanical properties," *Journal of*

*Alloys and Compounds*, **550**, 133-136 (**2013**).

118. M. Chandrasekaran, and Z. S. Xia. "Effect of alloying time and composition on the mechanical properties of Ti alloy," *Materials Science and Engineering a-Structural Materials Properties Microstructure and Processing*, **394**, 220-228 (**2005**).

119. S. Myhra, J. A. A. Crossley, and M. W. Barsoum. "Crystal-chemistry of the $Ti_3AlC_2$ and $Ti_4AlN_3$ layered carbide/nitride phases - characterization by XPS," *Journal of Physics and Chemistry of Solids*, **62**, 811-817 (**2001**).

120. S. F. Ren, J. H. Meng, J. B. Wang, J. J. Lu, and S. R. Yang. "Tribo-corrosion behaviors of $Ti_3SiC_2/Si_3N_4$ tribo-pair in hydrochloric acid and sodium hydroxide solutions," *Wear*, **274**, 8-14 (**2012**).

121. L. H. Zhang, and R. V. Koka. "A study on the oxidation and carbon diffusion of TiC in alumina titanium carbide ceramics using XPS and Raman spectroscopy," *Materials Chemistry and Physics*, **57**, 23-32 (**1998**).

123. R. Okazaki, D. Inoue, M. Shibata, M. Saika, S. Kido, H. Ooka, H. Tomiyama, Y. Sakamoto, and T. Matsumoto. "Estrogen promotes early osteoblast differentiation and inhibits adipocyte differentiation in mouse bone marrow stromal cell lines that express estrogen receptor (ER) α or β," *Endocrinology*, **143**, 2349-2356 (**2002**).

123. H. D. Jung, T. S. Jang, L. Wang, H. E. Kim, Y. H. Koh, and J. Song. "Novel strategy for mechanically tunable and bioactive metal implants," *Biomaterials*, **37**, 49-61 (**2015**).

124. K. Bordji, J. Y. Jouzeau, D. Mainard, E. Payan, P. Netter, K. T. Rie, T. Stucky, and M. HageAli. "Cytocompatibility of Ti-6Al-4V and Ti-5Al-2.5Fe alloys

according to three surface treatments, using human fibroblasts and osteoblasts," *Biomaterials*, **17**, 929-940 (**1996**).

125. M. M. M. Carrijo, L. G. Caro, H. Lorenz, P. Greil, N. Travitzky, and C. R. Rambo. "$Ti_3SiC_2$-based inks for direct ink-jet printing technology," *Ceramics International*, **43**, 820-824 (**2017**).

126. M. Mishra, Y. Sakka, C. F. Hu, T. S. Suzuki, T. Uchikoshi, and L. Besra. "Electrophoretic Deposition of $Ti_3SiC_2$ and Texture Development in a Strong Magnetic Field," *Journal of the American Ceramic Society*, **95**, 2857-2862 (**2012**).

127. Z. Q. Sun, M. S. Li, L. F. Hu, X. P. Lu, and Y. C. Zhou. "Surface Chemistry, Dispersion Behavior, and Slip Casting of $Ti_3AlC_2$ Suspensions," *Journal of the American Ceramic Society*, **92**, 1695-1702 (**2009**).

128. V. D. Jovic, M. W. Barsoum, B. M. Jovic, A. Ganguly, and T. El-Raghy. "Corrosion behavior of $Ti_3GeC_2$ and $Ti_2AlN$ in 1 m NaOH," *Journal of the Electrochemical Society*, **153**, B238-B243 (**2006**).

129. V. Milman, B. Winkler, J. White, C. Pickard, M. Payne, E. Akhmatskaya, and R. Nobes. "Electronic structure, properties, and phase stability of inorganic crystals: A pseudopotential plane-wave study," *International Journal of Quantum Chemistry*, **77**, 895-910 (**2000**).

130. D. Vanderbilt. "Soft self-consistent pseudopotentials in a generalized eigenvalue formalism," *Physical Review B*, **41**, 7892 (**1990**).

131. J. P. Perdew, K. Burke, and M. Ernzerhof. "Generalized gradient approximation made simple," *Physical Review Letters*, **77**, 3865 (**1996**).

132. J. P. Perdew, K. Burke, and M. Ernzerhof. "Generalized Gradient

Approximation Made Simple [Phys. Rev. Lett. 77, 3865 (1996)]," *Physical Review Letters*, **78**, 1396 (**1997**).

133. S. Grimme. "Semiempirical GGA-type density functional constructed with a long-range dispersion correction," *Journal of Computational Chemistry*, **27**, 1787-1799 (**2006**).

134. H. J. Monkhorst, and J. D. Pack. "Special points for Brillouin-zone integrations," *Physical Review B*, **13**, 5188 (**1976**).

135. J. F. Li, W. Pan, F. Sato, and R. Watanabe. "Mechanical properties of polycrystalline $Ti_3SiC_2$ at ambient and elevated temperatures," *Acta Materialia*, **49**, 937-945 (**2001**).

136. J. Rodriguez, P. Liu, J. Dvorak, T. Jirsak, J. Gomes, Y. Takahashi, and K. Nakamura. "The interaction of oxygen with TiC (001): Photoemission and first-principles studies," *The Journal of Chemical Physics*, **121**, 465-474 (**2004**).

137. T. Lee, E. Chang, and C. Yang. "Surface characteristics of Ti6Al4V alloy: effect of materials, passivation and autoclaving," *Journal of Materials Science: Materials in Medicine*, **9**, 439-448 (**1998**).

138. T. Hanawa, and M. Ota. "Calcium phosphate naturally formed on titanium in electrolyte solution," *Biomaterials*, **12**, 767-774 (**1991**).

139. M. Fredel, and A. Boccaccini. "Processing and mechanical properties of biocompatible $Al_2O_3$ platelet-reinforced $TiO_2$," *Journal of Materials Science*, **31**, 4375-4380 (**1996**).

140. A. Ochsenbein, F. Chai, S. Winter, M. Traisnel, J. Breme, and H. F. Hildebrand. "Osteoblast responses to different oxide coatings produced by the sol-gel process on

titanium substrates," *Acta Biomaterialia*, **4**, 1506-1517 (**2008**).

141. K. Marycz, J. Krzak-Ros, A. Donesz-Sikorska, and A. Smieszek. "The morphology, proliferation rate, and population doubling time factor of adipose-derived mesenchymal stem cells cultured on to non-aqueous $SiO_2$, $TiO_2$, and hybrid sol-gel-derived oxide coatings," *Journal of Biomedical Materials Research Part A*, **102**, 4017-4026 (**2014**).

142. Y. Zhao, S. M. Wong, H. M. Wong, S. L. Wu, T. Hu, K. W. K. Yeung, and P. K. Chu. "Effects of Carbon and Nitrogen Plasma Immersion Ion Implantation on *In vitro* and *In vivo* Biocompatibility of Titanium Alloy," *ACS Applied Materials & Interfaces*, **5**, 1510-1516 (**2013**).

143. K. Yeung, R. Poon, P. Chu, C. Chung, X. Liu, W. Lu, D. Chan, S. Chan, K. Luk, and K. Cheung. "Surface mechanical properties, corrosion resistance, and cytocompatibility of nitrogen plasma-implanted nickel-titanium alloys: A comparative study with commonly used medical grade materials," *Journal of Biomedical Materials Research Part A*, **82**, 403-414 (**2007**).

144. V.-H. Pham, S.-W. Yook, E.-J. Lee, Y. Li, G. Jeon, J.-J. Lee, H.-E. Kim, and Y.-H. Koh. "Deposition of TiN films on Co–Cr for improving mechanical properties and biocompatibility using reactive DC sputtering," *Journal of Materials Science: Materials in Medicine*, **22**, 2231-2237 (**2011**).

145. H.-H. Huang, C.-H. Hsu, S.-J. Pan, J.-L. He, C.-C. Chen, and T.-L. Lee. "Corrosion and cell adhesion behavior of TiN-coated and ion-nitrided titanium for dental applications," *Applied Surface Science*, **244**, 252-256 (**2005**).

146. B. Groessner-Schreiber, A. Neubert, W. D. Muller, M. Hopp, M. Griepentrog,

and K. P. Lange. "Fibroblast growth on surface-modified dental implants: An *in vitro* study," *Journal of Biomedical Materials Research Part A*, **64A**, 591-599 (**2003**).

147. V. Jovic, B. Jovic, S. Gupta, T. El-Raghy, and M. Barsoum. "Corrosion behavior of select MAX phases in NaOH, HCl and $H_2SO_4$," *Corrosion Science*, **48**, 4274-4282 (**2006**).

148. M. Barsoum. "Oxidation of $Ti_{n+1}AlX_n$ (n= 1-3 and X= C, N) I. Model," *Journal of the Electrochemical Society*, **148**, C544-C550 (**2001**).

149. Z. Ling, C. E. Ren, M.-Q. Zhao, J. Yang, J. M. Giammarco, J. Qiu, M. W. Barsoum, and Y. Gogotsi. "Flexible and conductive MXene films and nanocomposites with high capacitance," *Proceedings of the National Academy of Sciences*, 201414215 (**2014**).

150. M. Naguib, J. Come, O. Mashtalir, V. Presser, P. L. Taberna, P. Simon, M. W. Barsoum, and Y. Gogotsi. "MXenes: A new family of 2D transition metal carbides for use in lithium ion batteries and lithium ion capacitors," *Abstracts of Papers of the American Chemical Society*, **244**, (**2012**).

151. W. S. Hummers, and R. E. Offeman. "Preparation of Graphitic Oxide," *Journal of the American Chemical Society*, **80**, 1339-1339 (**1958**).

152. Y. H. Chen, Y. F. Niu, T. A. Tian, J. A. Zhang, Y. F. Wang, Y. P. Li, and L. C. Qin. "Microbial reduction of graphene oxide by Azotobacter chroococcum," *Chemical Physics Letters*, **677**, 143-147 (**2017**).

153. J. L. Zhang, H. J. Yang, G. X. Shen, P. Cheng, J. Y. Zhang, and S. W. Guo. "Reduction of graphene oxide via L-ascorbic acid," *Chemical Communications*, **46**,

1112-1114 (**2010**).

154. H. D. Jung, H. S. Park, M. H. Kang, Y. Li, H. E. Kim, Y. H. Koh, and Y. Estrin. "Reinforcement of polyetheretherketone polymer with titanium for improved mechanical properties and *in vitro* biocompatibility," *Journal of Biomedical Materials Research Part B-Applied Biomaterials*, **104**, 141-148 (**2016**).

155. A. Schroeder, G. Francz, A. Bruinink, R. Hauert, J. Mayer, and E. Wintermantel. "Titanium containing amorphous hydrogenated carbon films (a-C : H/Ti): surface analysis and evaluation of cellular reactions using bone marrow cell cultures *in vitro*," *Biomaterials*, **21**, 449-456 (**2000**).

156. D. G. Papageorgiou, I. A. Kinloch, and R. J. Young. "Mechanical properties of graphene and graphene-based nanocomposites," *Progress in Materials Science*, **90**, 75-127 (**2017**).

157. C. G. Trejo, D. Lozano, M. Manzano, J. C. Doadrio, A. J. Salinas, S. Dapia, E. Gomez-Barrena, M. Vallet-Regi, N. Garcia-Honduvilla, J. Bujan, and P. Esbrit. "The osteoinductive properties of mesoporous silicate coated with osteostatin in a rabbit femur cavity defect model," *Biomaterials*, **31**, 8564-8573 (**2010**).

158. P. T. Yan, R. J. Zhang, J. Jia, C. Wu, A. G. Zhou, J. Xu, and X. S. Zhang. "Enhanced supercapacitive performance of delaminated two-dimensional titanium carbide/carbon nanotube composites in alkaline electrolyte," *Journal of Power Sources*, **284**, 38-43 (**2015**).

159. H. F. Wang, Y. Z. Zhu, X. P. Yan, R. Y. Gao, and J. Y. Zheng. "A room temperature ionic liquid (RTIL)-mediated, non-hydrolytic sol-gel methodology to prepare molecularly imprinted, silica-based hybrid monoliths for chiral separation,"

*Advanced Materials*, **18**, 3266-3270 (**2006**).

160. B. Zewde, P. Pitliya, and D. Raghavan. "The role of surface modified $TiO_2$ nanoparticles on the mechanical and thermal properties of CTBN toughened epoxy nanocomposite," *Journal of Materials Science*, **51**, 9314-9329 (**2016**).

# Resume

**Chen Ke (陈 科)**, born on Aug. 1989, Zhejiang province, China.

## Education:

From Sep. 2008 to Jun. 2012, Bachelor's degree in *Materials Sciences and Engineering*, School of Materials Sciences and Engineering, *University of Sciences and Technology Beijing* (**USTB**).

From Sep. 2012 to Jun. 2015, Master's degree in *Materials Physics and Chemistry*, *Ningbo Institute of Materials and Technology*, *Chinese Academy of Sciences* (**NIMTE, CAS**) and *University of Chinese Academy of Sciences* (**UCAS**). (Academic advisor: Prof. *Qing Huang*)

From Sep. 2015 to Feb. 2018 (expected), Ph.D. in *Materials Sciences and Engineering*, Department of Materials Sciences and Engineering, *Seoul National University* (**SNU**). (Academic advisor: Prof. *Hyoun-Ee Kim*)

## Honors and Awards:

2017.03. Korea Rotary Scholarship Foundation - 정석규 Scholarship

2016.09. China Scholarship Council (CSC)

2015.09. SNU Global Scholarship 1

2015.06. Merit Student of UCAS

2012.06. Outstanding Graduates of USTB

2012.06. Outstanding Diploma Thesis of USTB

2010.11. The Second-Class for the People's Scholarship of USTB

2010.11. Merit Student of USTB (besides 2009.11)

2009.12. The Second Prize for National Physics Competition for Undergraduate

2009.10. National Endeavor Scholarship etc.

## Publications:

1. **Ke Chen**, Youhu Chen, Qihuang Deng, Seol-Ha Jeong, Tae-Sik Jang, Shiyu Du, Hyoun-Ee Kim, Qing Huang, and Cheol-Min Han. "Strong and Biocompatible Poly(lactic acid) Membrane Enhanced by $Ti_3C_2T_z$ (MXene) Nanosheets for Guided Bone Regeneration," ***submitted***.

2. **Ke Chen**[#], NianXiang Qiu[#], Qihuang Deng, Min-Ho Kang, Hui Yang, Jae-Uk Baek, Young-Hag Koh, Shiyu Du, Qing Huang, and Hyoun-Ee Kim. "Cytocompatibility of $Ti_3AlC_2$, $Ti_3SiC_2$, and $Ti_2AlN$: *In Vitro* Tests and First-Principles Calculations," *ACS Biomater Sci Eng*, 3, 2293–2301. **(2017)**

3. Lin Wang, Liyong Yuan, **Ke Chen**, Yujuan Zhang, Qihuang Deng, Shiyu Du, Qing Huang, Lirong Zheng, Jing Zhang, Zhifang Chai, Michel W. Barsoum, Xiangke Wang, and Weiqun Shi. "Loading Actinides in Multilayered Structures for Nuclear Waste Treatment: The First Case Study of Uranium Capture with Vanadium Carbide MXene," *ACS Appl Mater Inter*, 8, 16396-16403. **(2016)**

4. **Ke Chen**, Qun Ye, Jie Zhou, Lu Shen, Jianming Xue and Qing Huang. "Synthesis

of $Ti_2SC$ Using Iron Disulfide or Iron Sulfide Post-Treated with Acid," *J Am Ceram Soc*, 98, 1074-1079. **(2015)**

5. Jing Chen[#], **Ke Chen[#]**, Dingyi Tong, Youju Huang, Jiawei Zhang, Jianming Xue, Qing Huang and Tao Chen. "$CO_2$ and Temperature Dual Responsive "Smart" MXene Phases," *Chem Comm*, 51, 314-317. (**2015**)

6. Qun Ye, Peng Xiao, Wulong Liu, **Ke Chen**, Tao Chen, Jianming Xue, Shiyu Du, and Qing Huang. "Exploring the Potential of Exfoliated Ternary Ultrathin $Ti_4AlN_3$ Nanosheets for Fabricating Hybrid Patterned Polymer Brushes," *RSC Adv*, 5, 70339-70344. **(2015)**

7. Shanjie Yi, Haiqing Yin, **Ke Chen**, Dil Faraz Khan, Qingjun Zheng and Xuanhui Qu. "Microstructure and Properties of Nano-TiN Modified Ti(C,N)-based Cermets Fabricated by Powder Injection Molding and Die Pressing," *Int J Min Met Mater*, 20, 1115-1121. (**2013**).